Divergent neural pathways emanating from the lateral parabrachial nucleus mediate distinct components of the pain response

by

Michael C. Chiang

Bachelor of Arts, University of California, Berkeley, 2010

Submitted to the Graduate Faculty of

School of Medicine in partial fulfillment

of the requirements for the degree of

Doctor of Philosophy

University of Pittsburgh

2019

UNIVERSITY OF PITTSBURGH

SCHOOL OF MEDICINE

This dissertation was presented

by

Michael C. Chiang

It was defended on

July 12, 2019

and approved by

Rebecca P. Seal, Associate Professor, Department of Neurobiology

Bryan M. Hooks, Assistant Professor, Department of Neurobiology

Michael S. Gold, Professor, Department of Neurobiology

Nathaniel N. Urban, Professor, Department of Neurobiology

External examiner: Clifford B. Saper, Professor, Department of Neurology

Dissertation Director: Sarah E. Ross, Associate Professor, Department of Neurobiology

Divergent neural pathways emanating from the lateral parabrachial nucleus mediate distinct components of the pain response

Michael C. Chiang, PhD

University of Pittsburgh, 2019

The lateral parabrachial nucleus (lPBN) is a major target of spinal projection neurons conveying nociceptive input into supraspinal structures. However, the functional role of distinct lPBN efferents for diverse nocifensive responses have remained largely uncharacterized. Here, we show that two populations of efferent neurons from different regions of the lPBN collateralize to distinct targets. Activation of efferent projections to the ventromedial hypothalamus (VMH) or lateral periaqueductal gray (lPAG) drive escape behaviors, whereas the activation of lPBN efferents to the bed nucleus stria terminalis (BNST) or central amygdala (CEA) generates an aversive memory. Finally, we provide evidence that dynorphin expressing neurons span cytoarchitecturally distinct domains of the lPBN to coordinate these distinct aspects of the nocifensive response.

Table of Contents

List of Figures

List of Tables

Acknowledgements

As an undergraduate student, my interest in neuroscience grew under the mentorships of Drs. Garret D. Stuber and Antonello Bonci at University of California, San Francisco (UCSF). I gained invaluable technical and scientific experiences, for which I will always be grateful, while training with Dr. Nirao M. Shah also at UCSF. However, I believe that all my prior research experiences have come together as one and allowed me to become a true, independent scientist with my PhD advisor Dr. Sarah E. Ross. Training under Sarah's supervision has been one of the most influential experiences of my life. I have grown as a scientist. More importantly, I have grown as a person. Together, her support and kindness have helped shape the kind of scientist, physician, and person I want to be. It has been a great privilege and honor to train under her, and even as I move on in my career, I will continue to grow both as a person and scientist because of the lessons I have learned from her.

Completing my PhD in four years has not been a trivial endeavor, and I knew entirely what I committed myself to when I took on a systems and behavioral neuroscience project. Despite countless frustrations, I have had the great support of former lab member Lindsey Snyder and current lab members Drs. Tayler Sheahan and Kelly Smith. Enduring the hardships of scientific training would have been unimaginable without them. I am thankful to have formed fond memories within and outside the lab in their company. I am also grateful to have worked with everyone within the Ross lab, including the number of undergraduate students who have worked closely with me, and the Pittsburgh Center for Pain Research. Lastly, I would like to again thank Tayler Sheahan and Talia Adi, an incoming MSTP student, who have helped me tremendously with reviewing this thesis for grammatical and spelling errors to which I am notoriously prone to

making. Together, I simply cannot fathom the enormity of knowledge and personal growth I have gained through everyone's presence.

I am also thankful for the insight I have gained from my committee members. They have challenged me, and they have guided me. They have pushed me, and they have supported me. They are all my mentors, but more importantly, they are my friends. I have learned so much from my thesis committee – I hope to one day return the favor.

Outside the lab I have had immeasurable luck surrounding myself with amazing people (and my *loving* cat Bob). My friends have supported me through emotionally difficult times, lifted me when I felt down, opened their homes to me, explored the wild west of West Virginia with me, and so much more. To my closest friends, thank you for years of friendship and many more to come.

Lastly, I am thankful for all that my parents have done to provide for me, in whatever way they could, so I could have as many educational opportunities to pursue my academic endeavors. I remember their sacrifices and the years through which they have endured. They have been unwavering in their support. I am thankful to have learned this resilience that has helped me push through my own hardships just as they have done for my sake. For all that I have learned and received from them, I am blessed.

Abbreviations

AAV – adeno-associated virus

AVPV – anteroventral periventricular nucleus

BMA – basomedial amygdaloid nucleus

BNST – bed nucleus stria terminalis

BSTMV – medial ventral division of bed nucleus stria terminalis

Calb2 – calbindin 2

CCK - cholecystokinin

CEA – central amygdala

CGRP – calcitonin gene-related peptide

ChR2 – channelrhodopsin-2

CM – centromedial thalamic nucleus

Crh – corticotropin releasing hormone

CPA – conditioned place aversion

CTB – cholera toxin B

DBH – dopamine β-hydroxylase

DMH – dorsomedial hypothalamus

DNIC – diffuse noxious inhibitory control

dPBN – dorsal parabrachial nucleus

elPBN – external lateral parabrachial nucleus

eYFP – enhanced yellow fluorescent protein

GFP – green fluorescent protein

FISH – fluorescent in situ hybridization

IC – insular cortex

LH – lateral hypothalamus

lPAG – lateral periaqueductal grey

lPBN – lateral parabrachial nucleus

LRN - lateral reticular nucleus

MnPO – median preoptic nucleus

mPBN – medial parabrachial nucleus

NK1R – neurokinin 1 receptor

Nts – neurotensin

Oxtr – oxytocin receptor

Pdyn – preprodynorphin

PSD95 – post-synaptic density 95

PVT – paraventricular thalamic nucleus

ReaChR– red shifted variant of channelrhodopsin-2

RH – rhomboid nucleus

RVM – rostral ventromedial medulla

RTPA – real time place aversion

SPbN – spinoparabrachial neurons

Sst – somatostatin

Tac1 – tachykinin 1

TFA – tail flick assay

VMH – ventromedial hypothalamus

Table 1 Key resources table

REAGENT or RESOURCE	SOURCE	IDENTIFIER
Antibodies		
Rabbit anti-homer 1	Frontier Institute	Cat: AB_2571774; RRID: AB_2571774
Chicken anti-GFP	Aves Laboratory	Cat: GFP-1020; RRID: AB_10000240
Rabbit anti-c-fos	Santa Cruz Biotech	Cat: Sc-52; RRID: AB_216783
Mouse anti-NeuN	Millipore	Cat: MAB377; RRID: AB_2298772
Rabbit anti-NK1R	Sigma Aldrich	Cat: SAB4502913; RRID: AB_10746598
Donkey anti-chicken (IgG) Alexa Fluor 488 secondary antibody	Jackson ImmunoResearch	Cat: 703-035-155; RRID: AB_2340375
Donkey anti-rabbit (IgG) Alexa Fluor 555 secondary antibody	ThermoFisher	Cat: A-31572; RRID: AB_162543
Donkey anti-mouse (IgG) Alexa Fluor 647	ThermoFisher	Cat: A-31571; RRID: AB_162542
Bacterial and Virus Strains		
AAV2-hSyn-eYFP	UNC	Addgene: 50465
AAV2-hSyn.hChR2(H134R).eYFP	UNC	Addgene: 26973
AAV2-EF1a-DIO-eYFP	UNC	Addgene: 27056
AAV2-EF1a-DIO-hChR2(H134R)-eYFP	UNC	Addgene: 20298
AAV2-EF1a-flex-taCasp3-TEVp	UNC	Addgene: 45580
AAV8.2-hEF1a-DIO-synaptophysin-eYFP	MGH GTC	AAV-RN2
AAV8.2-hEF1a-DIO-PSD95-eYFP	MGH GTC	AAV-RN7
AAV8.2-hEF1a-synaptophysin-mCherry	MGH GTC	AAV-RN8
AAV9-CAGGS-FLEX-ChR2-tdtomato.WRPE.SV40	Penn Vector Core	Addgene: 18917
Chemicals, Peptides, and Recombinant Proteins		
Cholera toxin subunit B (Recombinant), Alexa Fluor 555	ThermoFisher	C34778
Cholera toxin subunit B (Recombinant), Alexa Fluor 647	ThermoFisher	C22843
PFA	Sigma Aldrich	P6148
Capsaicin	Sigma Aldrich	M2028
Formalin	Sigma Aldrich	HT501128
Tamoxifen	Sigma Aldrich	T5648-5G
Corn oil	Sigma Aldrich	C8267
Critical Commercial Assays		
RNAscope		

Fluorescent multiplex assay	ACD	320850
Pdyn probe	ACD	318771
Calca probe	ACD	417961
Tac1 probe	ACD	410351
Gad2 probe	ACD	415071
Fos probe	ACD	316921
Slc32a1 probe	ACD	319191
Slc17a6 probe	ACD	319171
EYFP probe	ACD	312131
DAPI	ACD	320858
3-plex positive control probe	ACD	320881
3-plex negative control probe	ACD	320871
Experimental Models: Organisms/Strains		
Mouse: C57BL6	Charles River	027
Mouse: Pdyn-IRES-Cre B6;129S-Pdyntm1.1(cre)Mjkr/LowlJ	Jackson Laboratory Krashes et a. 2014	IMSR Cat: JAX:027958; RRID: IMSR_ JAX:027958
Mouse: Gad2-IRES-Cre Gad2tm2(cre)Zjh/J	Jackson Laboratory Taniguchi et al. 2011	IMSR Cat: JAX:010802; RRID: IMSR_ JAX:010802
Mouse: Tacr1CreER	Ross lab; Huang et al. 2016	N/A
Mouse: Ai34D or Ai34(RCL-Syp/tdT)-D B6;129S-Gt(ROSA)26Sortm34.1(CAG-Syp/tdTomato)Hze/J	Jackson Laboratory Zeng 2011	IMSR Cat: JAX:012570; RRID: IMSR_ JAX:012570
Mouse: Rosa26 CAG-LSL-ReaChR-mCit B6.Cg-Gt(ROSA)26Sortm2.2Ksvo/J	Jackson Laboratory Hooks et al. 2015	IMSR Cat: JAX:026294; RRID: IMSR_ JAX:026294
Software and Algorithms		
Prism 7.0	GraphPad	N/A
Matlab	Mathworks	N/A
Mouse tracking algorithm	https://www.biorxiv.org/content/10.1101/558643v1	N/A

1.0 Introduction

1.1 The parabrachial nucleus: an overview of its function and connectivity

Noxious stimuli drive innate behaviors that promote an animal's immediate and long-term survival from these potentially life-threatening events. Unpleasant temperatures, food, and cutaneous sensations elicit avoidance behavior. In the presence of potentially threatening odors or visual cues, an animal becomes more aroused and primed for "fight or flight". Tissue damage drives escape behaviors and a memory of such events. Regardless of the modality of these stimuli, hardwired neural connections permit appropriate physiological responses that begin with adaptive autonomic changes which are followed by the emergence of learned avoidance behavior. These neural circuits encode stereotyped behavioral sequences that shift toward more complex motor actions as the severity of potential damage increases. For example, low intensity noxious stimuli drive withdrawal reflexes, whereas high intensity noxious stimuli recruit escape behaviors. Together, these distinct behavioral responses form a nocifensive response (Browne et al., 2017; Espejo and Mir, 1993; Fan et al., 1995; Le Bars et al., 2001). Despite the importance of the appropriate response for survival, the neural underpinnings of the distinct components that make up the nocifensive response remain to be fully explored. A growing body of work points to the significant contributions of the parabrachial complex (PBN), an evolutionarily conserved hindbrain structure in mammalian species that orchestrates behavioral outputs with autonomic changes to these threats.

The PBN is located in the pons at the junction between midbrain and hindbrain and comprises more than a dozen subnuclei that surround the superior cerebellar peduncles, fiber tracts

that communicate between deep cerebellar and midbrain nuclei. The neurons within these cytoarchitecturally distinct subdivisions express neuropeptides and chemical markers that both neurochemically and functionally distinguish them. Furthermore, the inputs into PBN and its subregions can also be categorized in this way. Such differential expression patterns may underlie how the PBN, through its anatomical organization, integrates incoming information to elicit a coordinated behavioral response through its projections to forebrain targets. Here, we provide an overview of its anatomical organization and functional connectivity in response to diverse sensory modalities.

1.2 Parabrachial cell morphology

The PBN complex has been cytoarchitecturally categorized based upon the morphology of the subpopulations of neurons within each subdivision of the PBN complex. Medial PBN (mPBN) comprises populations of neurons heterogeneous in size and morphology, unlike those within the lateral PBN (lPBN), which comprise several homogeneous groups (Fulwiler and Saper, 1984; Saper and Loewy, 1980). Whereas the dendritic domains of mPBN neurons have been less extensively characterized, those of the lateral PBN (lPBN) can be categorized into one of several groups: those that remain confined within subnuclear domains, those that extend into neighboring lPBN subnuclei, and those that project to other brain regions (Herbert and Bellintani-Guardia, 1995). Despite extensive morphometric and anatomical analysis of the cells, the identities of pre- and post-synaptic lPBN cells within these local microcircuits remains to be fully characterized. Nevertheless, these studies support the idea that cells within both mPBN and lPBN serve as

integrators of both interoceptive and exteroceptive signals to elicit a coordinated behavioral action through its connections with downstream targets.

1.3 Anatomical organization of the parabrachial nucleus

1.3.1 Afferent projections

The afferent and efferent connections in the PBN complex have been well-characterized in rigorous detail. Numerous ascending and descending pathways converge onto the PBN complex that contribute to the regulation of autonomic responses to interoceptive and exteroceptive signals. Sensory input regarding taste, visceral information, fluid balance, and cardiovascular function arise from the area postrema and nucleus of the solitary tract (NTS) and terminate in discrete patterns that map to the dendritic domains and subnuclear boundaries of the lPBN (Cechetto and Calaresu, 1985; Feil and Herbert, 1995; Herbert et al., 1990). The NTS, retrotrapezoid nucleus in the rostral medulla of the brainstem, and Kölliker-Fuse nucleus neighboring the PB complex also convey chemosensory signals to lPBN to regulate respiration and hypercapnic arousal (Kaur et al., 2013; Kaur et al., 2017).

Nociceptive, pruritic, and thermal input also reach the PB complex through spinoparabrachial neurons within lamina I of the dorsal horn spinal cord. These projection neurons express the neurochemical marker neurokinin-1 receptor and densely innervate dorsal divisions of the PB complex, primarily the internal, central, and dorsal subnuclei (Cameron et al., 2015; Harrison et al., 2004; Hylden et al., 1989). The spinal trigeminal nucleus carrying nociceptive information related to the craniofacial structures projects primarily to the external lateral division

of the PBN (Feil and Herbert, 1995; Rodriguez et al., 2017)The rostroventral medulla (RVM) also projects to the lPBN. Although these connections have primarily been characterized as mediating cardiovascular and respiratory input, a subpopulation RVM neurons expressing *Tac1* has recently been demonstrated to be involved in mediating nocifensive responses to noxious heat (Barik et al., 2018)

1.3.2 Efferent projections

The PBN complex comprises multiple subnuclei with reciprocal connections with its inputs and whose outputs are also organized topographically (Fulwiler and Saper, 1984; Moga et al., 1990; Saper and Loewy, 1980; Tokita et al., 2009). Its vast connectivity with forebrain and brainstem structures highlights its critical involvement in integrating sensory information with brain regions that regulate autonomic functions in response to gustation, consummatory behavior, pain, itch, thermoregulation, respiratory control, and cardiovascular regulation (Benarroch, 2016, 2018; Davern, 2014; Kaur and Saper, 2019). Efferent projections to insula arise primarily from mPBN and the ventral lPBN. The bed nucleus of the stria terminalis and central amygdala also receive dense innervation from lPBN subnuclei, with the greatest number of inputs arising from elPBN. Efferents to hypothalamic regions arise primarily from mPBN and rostral lPBN, mainly the superior lateral and dorsal divisions, and innervate the preoptic area, anteroventral periventricular, paraventricular, dorsal medial, ventromedial, and lateral hypothalamic nuclei. Thalamic inputs to paraventricular thalamus and thalamic nuclei (ventral posterior, ventral medial, intralaminar, and centromedial) also arise from mPBN and generally rostral lPBN subdivisions (central, internal, and dorsal lPBN). Brainstem projections to NTS and rostral medulla arise from the ventrolateral aspect of the lPBN. Advances in techniques and the emergence of genetically

engineered mice to target distinct lPBN subnuclei have enabled more detailed characterizations of PBN circuitry and their involvement in behavioral responses to threats and aversive stimuli.

1.4 Physiological properties of parabrachial neurons

In line with the multiple distinct subnuclei of the lPBN, the neural populations within these subdivisions appear to have somewhat different electrophysiological properties. Compared to the elPBN, neurons within more dorsal divisions exhibited less spike frequency adaptation (Hayward and Felder, 1999). A separate study identified additional differences in membrane resistance and time constant, action potential duration, firing frequency, and action potential latency among separate dPBN subnuclei (Kobashi and Bradley, 1998). How these properties relate to different genetically-defined classes of lPBN neurons and their functional contributions remain an area of active investigation.

1.5 Neurochemical and functional characterizations of parabrachial

As prior studies have revealed, the lPBN comprises cytoarchitecturally distinct divisions with distinct projection patterns, suggesting the possibility of functional segregation of different genetically defined neural populations. Some subdomains uniquely express a number of neuropeptides, whereas other neurochemical markers appear to be broadly expressed (Block and Hoffman, 1987; Miller et al., 2012; Zagami and Stifani, 2010). Somatostatin, enkephalin, and vasoactive intestinal peptide were observed to be mostly robustly expressed in dPBN. Neurotensin

was found to be most abundantly expressed in more rostral dPBN. Cholecystokinin expression was also in dPBN, specifically the superiolateral division. Tyrosine hydroxylase-positive cells were found scattered throughout dPBN.

The advances in mouse genetics have allowed for the generation of powerful gene-targeting technology that enables cell-type specific neural manipulations from a heterogeneous mix. Although the number of genetically-defined populations within the lPBN have yet to be fully characterized, a number of Cre-driver mouse lines have been developed to permit the visualization and functional characterization of distinct subpopulations. An overview of the current understanding of these lPBN subsets is provided.

SatB2 neurons and electrophysiological evidence for taste

Sensory neurons relay different modalities of taste to the nucleus solitary tract and subsequently into the parabrachial nucleus (Carleton et al., 2010). Electrophysiological recordings have demonstrated a topographic response to different tastants: bitter or generally unpleasant tastes activate elPBN, whereas sweet tastants preferentially promote Fos expression in dPBN (Tokita and Boughter, 2016; Yamamoto et al., 1994; Yamamoto et al., 2009). Only recently has the molecular identity of a gustatory neural population in the central nervous system been implicated in a particular taste modality, that is for sweet taste. SatB2-expressing neurons occur in the waist region of the parabrachial complex that bridges the superior cerebellar peduncle between the medial and lateral PBN. A recent study found that ablating this population resulted in significantly diminished taste preference for sucrose without effecting preference for umami, bitter, sour, or salty (Fu et al., 2019). Furthermore, activating SatB2-expressing projections to ventral posteromedial thalamus enhanced appetitive behavior and promoted real time place preference to

light stimulation, suggesting this specific output encodes positive valence to consummatory behavior. Identifying additional genetically-defined lPBN populations that respond preferentially to other taste modalities would provide greater insight into gustatory coding in the lPBN.

Cholecystokinin, leptin receptor and glucose homeostasis

The central circuits that mediate glucose homeostasis involve lPBN neurons expressing cholecystokinin (CCK) (Garfield et al., 2014). These neurons are expressed throughout lPBN, with the majority located in dorsal divisions of lPBN. Hypoglycemia drives Fos expression in these neurons, which consequently signal to downstream VMH neurons expressing steroidogenic-factor 1 (SF-1) to drive an autonomically mediated counterregulatory response to increase glucose production. Moreover, CCK-positive lPBN neurons coexpress the leptin receptor. Administration of leptin into the lPBN resulted in impaired hyperglycemic response, and genetic deletion of leptin receptor for CCK lPBN neurons enhanced the counterregulatory response (Flak et al., 2014). The neural circuitry that CCK-expressing neurons engage underlie physiological adaptations that require enhanced glucose production and mobilization. Consistent with this idea, activating SF-1 VMH neurons robustly elicits both overt defensive-like behaviors characterized by running, jumping, and some freezing in addition to autonomic changes in respiratory rate, heart rate, and pupil size (Wang et al., 2015). Thus the increase in glucose production may fuel the metabolic needs for the animal to engage in these escape-like behaviors. Furthermore, activating PAG neurons expressing the leptin receptor promoted hyperglycemia, whereas genetically ablating leptin receptor from these neurons also increased glucose production in response to noxious stimuli (Flak et al., 2017). Together, the CCK-positive subset of lPBN neurons integrates sensory signals, such as noxious input or hunger, to facilitate appropriate autonomic and behavioral responses that require glucose mobilization.

lPBN and feeding

Different lPBN subpopulations encode either positive and negative valences to feeding. An unknown dPBN population receives input from melanocortin-4 receptor (MC4R) paraventricular hypothalamus neurons to mediate positive valence and satiety in food-deprived mice (Garfield et al., 2015). However, gustatory neurons that express either CCK or noradrenergic, dopamine β-hydroxylase (DBH) form monosynaptic connections with CGRP elPBN neurons that suppress food intake (Campos et al., 2016; Roman et al., 2016). Both the CGRP and dPBN neurons downstream of MC4R-positive PVH neurons appear to be distinct, nonoverlapping populations. Their differential activity, and potentially interactions among each other and other unknown lPBN populations, regulate food consumption.

Oxytocin receptor and fluid satiety

Parabrachial neurons have been implicated in regulating fluid homeostasis (Geerling and Loewy, 2008; Menani et al., 2014). Whereas some lPBN neurons drive salt intake in hyponatremic mice (Geerling and Loewy, 2007; Jarvie and Palmiter, 2017), those that express the oxytocin receptor (Oxtr) specifically regulate hypernatremia and hypervolemia regardless of food and salt deprivation (Ryan et al., 2017). Chemogenetic activation of these neurons reduces non-caloric fluid intake in dehydrated mice, whereas inhibition promotes the opposite effect. Oxtr-positive lPBN neurons are regulated through multiple pathways. Although many brain regions express and use oxytocin for different physiological purposes (Lee et al., 2009), those within the paraventricular nucleus of the hypothalamus lie upstream of Oxtr-positive lPBN neurons and moderately regulate their activity. On the other hand, inputs from the nucleus of the solitary tract

strongly reduce fluid intake likely through the recruitment of multiple lPBN subpopulations that indirectly drive Oxtr-expressing lPBN neurons.

Dynorphin, FoxP2, and thermal homeostasis

A subset of excitatory dPBN neurons express the neuropeptide dynorphin and have been found to respond to warm ambient temperature (Geerling et al., 2016). Furthermore, these neurons project to numerous forebrain regions that govern thermosensation (Allen brain institute Experiment: 543876073, http://connectivity.brain-map.org/). Consistent with a role in thermoregulation, dorsal horn neurons carrying thermal information innervate dPBN within the subdivisions of dynorphin-expressing neurons. In turn, these distinct lPBN divisions project to the preoptic area of the anterior hypothalamus to mediate autonomic responses that maintain thermal homeostasis (Nakamura and Morrison, 2008, 2010; Tan and Knight, 2018). Additional studies are warranted to confirm whether dynorphin-positive neurons indeed contribute to thermoregulation in response to warm temperature. In addition, a broad excitatory population of neurons within lPBN express the transcription factor and neurochemical marker FoxP2 (forkhead box protein P2). However, only a subset of FoxP2-expressing neurons within the elPBN respond strongly to cold ambient temperature (Geerling et al., 2016). Thus, two non-overlapping populations within the lPBN may be mediating the thermoregulatory response to warm or cold temperatures.

Glutamatergic lPBN neurons and itch

Although the lPBN responds to pruriceptive stimuli (Jansen and Giesler, 2015), a specific genetically-defined subset of lPBN neurons has yet to be attributed to this sensory modality. Rather, glutamatergic lPBN neurons, which make up the majority of lPBN (Guthmann et al., 1998; Yokota et al., 2007), have been found to be important mediators of itch. Optogenetic or chemogenetic inhibition of lPBN, as well as genetic deletion of *Vglut2* from lPBN neurons, resulted in decreased scratching in response to a pruritogen such as chloroquine (Mu et al., 2017). A separate study found that silencing glutamatergic neurotransmission in CGRP-expressing neurons also attenuated scratching to chloroquine and non-chemical stimuli (Campos et al., 2018). Interestingly, chemogenetic inhibition or genetic deletion of *Vglut2* had no effect on acute mechanical and thermal hypersensitivity (Mu et al., 2017). Additional experiments will be needed to confirm these findings.

lPBN contributions to pain affect

lPBN has been demonstrated to serve an important role in receiving, processing, and relaying somatic and visceral nociceptive signals (Bernard and Besson, 1990; Bernard et al., 1994; Bourgeais et al., 2001; Buritova et al., 1998; Campos et al., 2018; Gauriau and Bernard, 2002a, b; Hermanson and Blomqvist, 1996). In animal models the lPBN is one of two major supraspinal targets of the anterolateral tract (Cameron et al., 2015; Cechetto et al., 1985; Hylden et al., 1989; Polgar et al., 2010; Todd, 2010). Although the lPBN responds to different noxious modalities (chemical, thermal, and mechanical), the elPBN neurons have been attributed to the affective dimensions of pain via its connections to amygdalar targets (This population expresses CGRP, which will be discussed in following paragraph) (Bernard and Besson, 1990; Gauriau and Bernard, 2002a; Han et al., 2015a; Jasmin et al., 1997). Recent work has implicated a nociceptive trigemino-

parabrachial pathway onto CGRP-expressing elPBN neurons in which its activation induces stress vocalization and avoidance behavior, while its inhibition reduces inflammatory facial pain via capsaicin-induced mechanical hypersensitivity of the whisker pads (Rodriguez et al., 2017).

NPY1R and hunger as a competing behavioral state to reduce inflammatory pain

The lPBN serves as an integrator of different physiological states to govern appropriate adaptive behaviors to different environmental challenges, for example between hunger and pain (Malick et al., 2001). A recent study identified a neural mechanism through which the lPBN prioritizes these competing needs. Food-deprived mice exhibit diminutions in the negative valence associated with and the behavioral response to hindpaw formalin administration, a model of inflammatory pain (Alhadeff et al., 2018). However, acute pain response remained unaffected. This competing state arises from the increased activity of GABAergic inputs from agouti-related peptide (AgRP) neurons in the arcuate nucleus neurons following 24-hour fasting. In the presence of an acute painful stimulus, the activity of these neurons decreases. Microinjections of GABA antagonists into lPBN failed to reverse the nocifensive licking response to intraplantar formalin. Rather, the release of neuropeptide Y (NPY) from AgRP-positive afferents onto lPBN neurons expressing the NPY1 receptor (NPY1R) suppressed the inflammatory nocifensive response to intraplantar formalin. The degree in which NPY1R neurons overlap with CGRP-expressing neurons would warrant future investigations, as the activity of these neurons encode negative valence and promote aversive behaviors (Campos et al., 2018).

Tachykinin1 and nocifensive behavior

A recent study identified an lPBN population expressing tachykinin 1 (Tac1). Tac1-positive lPBN neurons are primarily within the elPBN with a sparsely distributed population throughout dPBN (Barik et al., 2018). Those in elPBN partially overlap with CGRP-positive neurons and project to similar forebrain structures. However, Barik et al. revealed a unique subset of Tac1 neurons that project to RVM. Chemogenetic activation of this population resulted in enhanced nocifensive response to noxious heat as measured by increased jumping. Importantly, they noted no jumping without this noxious stimulus, and this motor response occurred independent of forebrain involvement. How Tac1 neurons projecting to these forebrain targets contribute to other stereotyped motor responses to noxious stimuli remain to be determined.

Pituitary adenylate cyclase activating polypeptide, anxiety, and pain

Pituitary adenylate cyclase activating polypeptide (PACAP) signaling through its cognate receptor PAC 1 has been implicated in nociception. PACAP deficient mice or PAC 1 receptor KO mice exhibit dramatic decreases in persistent pain responses (Jongsma et al., 2001; Mabuchi et al., 2004). However, it is important to note that expression of PACAP and PAC 1 occur broadly throughout the peripheral and central nervous systems (Mulder et al., 1994; Zhang et al., 1995). Within brain, and particularly the lPBN, PACAP expression appears localized to the elPBN. Consistent with this, its projection pattern overlaps with those of the CGRP-expressing population by approximately 60 – 70%, and excitotoxic lesions of lPBN results in significant loss of both PACAP and CGRP immunoreactive fibers in CEA and BNST (Missig et al., 2014). Interestingly, PACAP appears to be broadly upregulated in lPBN neurons following the chronic constriction injury (CCI) model of neuropathic pain (Missig et al., 2017), suggesting functional expression of PACAP correlated with neuroplasticity. PACAP infusions into CEA increased anxiety-like

behaviors and thermal hypersensitivity, whereas the PACAP receptor 1 antagonist PACAP (6-38) attenuated the CCI-mediated behavioral effects. These experiments demonstrate the contributions of parabrachial-amygdalar PACAP signaling on different measures of pain behavior and suggest a neural substrate through which the development of chronic pain and stress-related comorbidities arise (Scioli-Salter et al., 2015).

lPBN signaling on cardiovascular response

The nucleus of the solitary tract and brainstem nuclei transmit signals related to blood pressure, aortic stretch, and carotid chemoreceptors to the lPBN (Benarroch, 2018; Davern, 2014; Jhamandas et al., 1991). However, the genetic identity of lPBN neurons underlying cardiovascular responses remains unclear, although they have been found to be primarily excitatory (Guo et al., 2005). Electrical and glutamate stimulation of different lPBN subdivisions resulted in opposing effects: elPBN activation caused tachycardia whereas dlPBN appeared to drive depressor bradycardic changes (Chamberlin and Saper, 1992).

Calcitonin gene-related peptide and arousal from hypercapnia

Stimulating lPBN neurons results in increased cortical arousal thought to be mediated through its connections with forebrain structures (Luo et al., 2018; Qiu et al., 2016). In line with these studies, genetic deletion of glutamatergic signaling decreases arousal states and reduces cortical activity (Kaur et al., 2013). Recently, a study found that the CGRP-expressing population serves critical roles in mediating cortical arousal, at least in response to hypercapnia (Kaur et al., 2017). Stimulating these neurons decreases the latency to arousal and increases wakefulness states during hypercapnia. Inhibiting these neurons prevented hypercapnia-induced arousal. Moreover, inhibiting projections of CGRP-positive lPBN neurons to forebrain structures (CEA, BNST, and LH) all increased arousal latency to hypercapnia. These suggest redundant pathways that underlie

a critical physiological and behavioral response to a life-threatening stimulus. Still, differences were observed between the latency to which terminal inhibition of these projections delayed arousal latency, leaving open the possibility of subtle differences in the functional significance in these different ascending pathways that increase cortical arousal.

Calcitonin gene-related peptide signaling as a general alarm

As described in the preceding paragraphs, the CGRP-expressing elPBN population has been attributed to diverse physiological and behavioral roles, suggesting that these neurons respond more broadly to a wide range of sensory signals (Palmiter, 2018; Saper, 2016). Indeed, a recent study found that elPBN CGRP neurons respond to multiple different stimuli that may be of potential harm – visceral and cutaneous noxious input (chemical, mechanical, thermal, and electrical) in addition to environmental stimuli such as novelty and fear learning (Campos et al., 2018). These neurons seem to encode negative valence because blocking glutamatergic release resulted in decreased behavioral responses to unpleasant or potentially harmful stimuli (reduction in chloroquine-induced scratching, increased novel food intake, and attenuated conditioning to aversive signals) (Campos et al., 2018; Carter et al., 2015; Chen et al., 2018; Han et al., 2015b; Palmiter, 2018). How CGRP-expressing elPBN neurons orchestrate these diverse behavioral and physiological responses remains a topic of exploration.

1.6 Summary

The wide range of sensory information that converges onto the lPBN underscores the diversity of lPBN neurons involved in responding to different sensory modalities. Furthermore, it emphasizes the clinical significance of lPBN signaling in different pathophysiological states in

human diseases. For example, circuit dysfunction involving the CGRP-expressing population may have significant implications in the manifestation of a wide range of human disorders such as chronic pain, anorexia, and generalized anxiety. Given the diverse roles of lPBN, understanding the functional contributions of even a single genetically-defined subpopulation is a huge endeavor. Instead, we focused our efforts on understanding lPBN contributions to one of its many physiological roles – that is, how lPBN orchestrates behavioral responses to pain. In Chapter 2, we characterize the unique anatomical traits of different lPBN subnuclei. Consequently, we designed experiments aimed to elucidate the role of different subregions of lPBN and their anatomical connections to downstream targets on the nocifensive response in Chapter 3. Through our investigations we identified a unique subpopulation of lPBN neurons expressing dynorphin, which we hypothesize coordinates nocifensive responses detailed in Chapter 4. Finally, we speculate more broadly about how these lPBN efferent pathways underlie different aspects of homeostastic regulation of different sensory modalities.

2.0 Lateral parabrachial nucleus circuitry and activity in the pain response

2.1 Introduction

The lPBN is a major downstream target of spinoparabrachial neurons that conveys noxious signals into supraspinal structures, and previous work has demonstrated lPBN involvement in responses to these inputs. However, most have studied the excitatory population expressing the vesicular glutamate transporter 2 (*Vglut2*), as they compose the majority of neurons within lPBN. (Geerling et al., 2017; Guthmann et al., 1998; Yokota et al., 2007). In this chapter we describe experiments that determine the significance of the lPBN in the pain response. To get at this, we target a subset of inhibitory lPBN neurons expressing *Gad2* that have not been thoroughly explored. These data lead us to consequently perform a series of experiments that characterize in further detail the anatomical projections of lPBN outputs, which we believe are also primarily excitatory. Given the cytoarchitecturally distinct divisions of lPBN, we predict that these regions exhibit unique projection patterns that potentially regulate different physiological and behavioral responses.

2.2 Methods

2.2.1 Animals

Mice were given free access to food and water and housed under standard laboratory conditions. The use of animals was approved by the Institutional Animal Care and Use Committee of the University of Pittsburgh. *Gad2-IRES-Cre* (Taniguchi et al., 2011), Ai34 (RCL-Syp/tdT)-D, and Rosa26 CAG-LSL- ReaChR-mCit (Hooks et al., 2015) were obtained from Jackson Laboratory. Wild-type C57BL/6 mice were obtained from Charles River (Cat # 027). For all experiments 8 – 16 week-old male and female mice were used. In all cases, no differences between male and female mice were observed and so the data were pooled. Age-matched littermates were used for all behavioral experiments that involved mice harboring the knock-in allele Cre-recombinase.

2.2.2 Viruses

The following viruses were used for experimentation: AAV2-EF1a-DIO-eYFP (Addgene: 27056), AAV2-EF1a-DIO-hChR2(H134R)-eYFP (Addgene: 20298), and AAV2-CMV-CreGFP (Addgene 49056). Viruses were purchased from University of North Carolina Vector Core and University of Pennsylvania Vector Core.

2.2.3 Stereotaxic injections and optical fiber implantation

Animals were anesthetized with 2% isoflurane and placed in a stereotaxic head frame. Ophthalmic ointment was applied to the eyes. The scalp was shaved, local antiseptic applied (betadine), and a midline incision made to expose the cranium. The skull was aligned using cranial fissures. A drill bit (MA Ford, #87) was used to create a burr hole and custom-made metal needle (33 gauge) loaded with virus was subsequently inserted through the hole to the injection site. Virus was infused at a rate of 100 nL/min using a Hamilton syringe with a microsyringe pump (World Precision Instruments). *Gad2*^{Cre} mice were bilaterally injected with 0.5 μl virus. The injection needle was left in place for an additional 5- 10 min and then slowly withdrawn. Injections and optical fiber implantations were performed bilaterally at the following coordinates for each brain region: BNST: AP +0.50 mm, ML ± 1.00 mm, DV -4.30; CEA: AP -1.20 mm, ML ± 2.85 mm, DV -4.50; VMH: AP -1.48 mm ML ± -0.50 mm DV -5.80 mm; lPAG: AP -4.70 mm, ML ± 0.74 mm, DV: -2.75; and lPBN AP -5.11 mm, ML ± 1.25 mm, DV: -3.25. For implantation of optical fibers (Thor Labs: 1.25 mm ceramic ferrule 230 μm diameter), implants were slowly lowered 0.300-0.500 mm above the site of injection and secured to the skull with a thin layer of Vetbond (3M) and dental cement. The incision was closed using Vetbond and animals were given a subcutaneous injection of buprenorphine (0.3 mg/kg) and allowed to recover over a heat pad. Mice were given 4 weeks to recover prior to experimentation.

2.2.4 CTB backlabeling

Fluorescently conjugated cholera toxin subunit B-Alexa-fluor conjugates -555 and -647 (CTB, ThermoFisher C34778, C22843) were stereotactically injected (0.2 μl, 1 mg/ml) into the

brain regions of interest and subsequently analyzed 10 days following injection. Mice were perfused and brains were processed as described above for immunohistochemistry. CTB-labeled cells were quantified using 65 μm z-stacked images at 2 μm steps of the entire lPBN (n = 3 – 5 mice per backlabeled region). For retrograde labeling of cells and quantification of pre- and post-synaptic markers, 3 – 4 40 μm sections were quantified for a given animal, and 4 mice were used per experiment.

2.2.5 Immunohistochemistry

Mice were anesthetized with an intraperitoneal injection of urethane, transcardially perfused, and post-fixed at least four hours in 4% paraformaldehyde. 40 or 65 μm thick transverse brain or spinal cord sections were collected on a vibratome and processed free-floating for immunohistochemistry. Sections were blocked at room temperature for two hours in a 10% donkey serum, 0.1% triton, 0.3M NaCl in phosphate buffered saline. Primary antisera was incubated for 14 hours overnight at 4°C: chicken anti-GFP (1:1K). Sections were subsequently washed three times for 20 minutes in wash buffer (1% donkey serum, 0.1% triton, 0.3M NaCl) and incubated in secondary antibodies (Life Technologies, 1:500) at room temperature for two hours. Sections were then incubated in Hoechst (ThermoFisher, 1:10K) for 1 minute and washed 7 times for 15 minutes in wash buffer, mounted and coverslipped.

2.2.6 Image acquisition and quantification

Full-tissue thickness sections were imaged using either an Olympus BX53 fluorescent microscope with UPlanSApo 4X, 10X, or 20X objectives or a Nikon A1R confocal microscope

with 20X or 60X objectives. All images were quantified and analyzed using ImageJ. For all images, background pixel intensity was subtracted as calculated from control mice. To quantify the area of synapses observed, confocal images using single optical planes were converted into a binary scale and area of signal taken as a ratio of the total area (one section per region of interest, n = 6 mice). To quantify the number of *Gad2*^{Cre} neurons labeled, a single optical plane was imagined from full-tissue thickness sections and neurons were manually quantified. To quantify CTB-labeled cells in tracing experiments, confocal images were manually quantified in a stereological manner using full-tissue thickness z-stacked images at 2 μm steps of the entire lPBN (3 – 4 mice per group).

2.2.7 Behavior

All assays were performed and scored by an experimenter blind to virus (eYFP or ChR2). Post hoc analysis confirming specificity of viral injections and proper fiber implantation were also performed blinded to animal identity, and mice in which viral injections and/or fiber implantation were considered off target excluded from analysis. All testing was performed in the University of Pittsburgh Rodent Behavior Analysis Core. The following optogenetic stimulation parameters were used: 10 mW, 20 Hz, 5 ms duration pulses.

Mechanical allodynia

Mice were allowed to habituate for at least two hours prior to testing. Mice received a 10 ul intraplantar injection of 0.03% capsaicin dissolved in 2.5% Tween, 2.5% ethanol in PBS and tested for mechanical hypersensitivity via the up-down method (Chaplan et al., 1994). After 5-10 minute resting period, mice were optogenetically stimulated and tested for mechanical

hypersensitivity. Mice were again allowed to rest for 5-10 minutes before von Frey testing for post-stimulation effects on mechanical hypersensitivity.

2.2.8 Statistical analysis

All statistical analyses were performed using GraphPad Prism 7.0. Values are presented as mean ± SEM. Statistical significance was assessed using one-way repeated measures ANOVA followed by Holm-Sidak post-hoc test or two-way repeated measures ANOVA followed by Holm-Sidak post-hoc test. Significance was indicated by $p \leq 0.05$. Sample sizes were based on pilot data and are similar to those typically used in the field.

2.3 Results

2.3.1 Inhibition of lPBN on the nociceptive response and lPBN connectivity

Nociceptive information is conveyed from the spinal cord to multiple regions of the brain in parallel, including brainstem, midbrain and forebrain structures (Todd, 2010). Within the lPBN, neurons throughout all cytoarchitecturally distinct divisions respond quite robustly to different forms of noxious stimuli, as suggested by the expression of the early immediate gene *Fos* (Bernard et al., 1994; Bester et al., 1997; Bourgeais et al., 2001; Hermanson and Blomqvist, 1996, 1997; Menendez et al., 1996). Although the lPBN is a major target of the anterolateral tract in murine species (Todd, 2010; Todd et al., 2000), its relative contribution to pain behaviors has only recently been explored (Alhadeff et al., 2018; Barik et al., 2018; Huang et al., 2018; Rodriguez et al., 2017).

Moreover, these neurons are thought to be excitatory, thus conveying the nociceptive input from spinal cord to downstream forebrain targets that drive appropriate behavioral and autonomic responses to these noxious signals. To further understand the contributions of lPBN to pain behaviors, we tested whether transiently inhibiting the lPBN would affect the behavioral response to noxious stimuli. For these experiments, adenoassociated virus (AAV) encoding a Cre-dependent channelrhodopsin-2 (ChR2) or enhanced yellow fluorescent protein (eYFP) was bilaterally delivered into the lPBN using the *Gad2*^{Cre} allele. This allows us to optogenetically control the activity of inhibitory neurons within the lPBN in live, behaving mice. (Figures 1A and 1B). In the absence of blue light, both ChR2 and eYFP mice showed capsaicin-induced mechanical hypersensitivity.

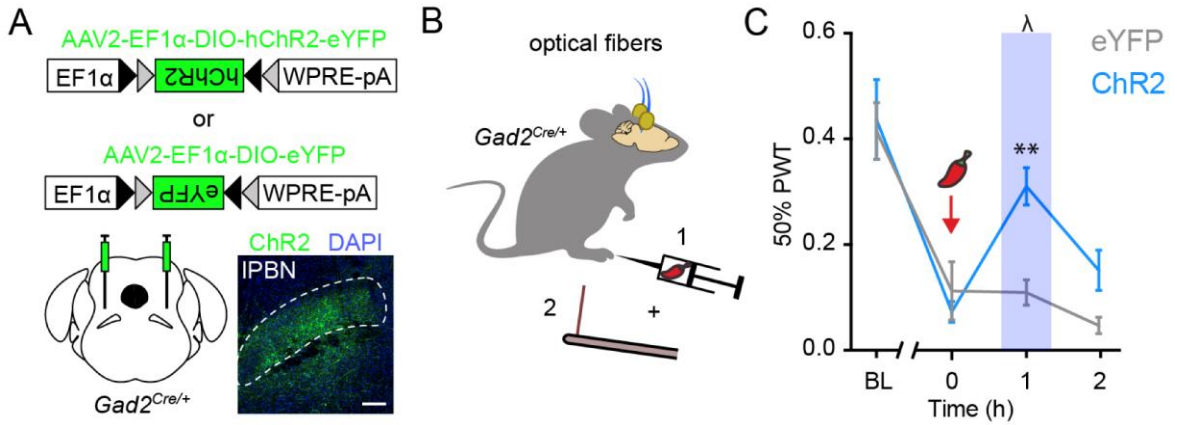

Figure 1 lPBN is required for mechanical hypersensitivity

(A) Experimental strategy to drive inhibition in the lPBN. AAVs encoding Cre-dependent ChR2 or eYFP were bilaterally injected into the lPBN of *Gad2*^{Cre} mice. Representative image depicts expression of ChR2 within the lPBN (outline). Scale bar = 100 μm.

(B) Mechanical hypersensitivity was (1) induced through intraplantar injection of capsaicin (10 μl, 0.03%) and (2) tested using von Frey filaments.

(C) Paw withdrawal threshold (PWT) was significantly reduced during optogenetic stimulation (blue bar) in ChR2-expressing mice compared to eYFP-expressing controls. Data are mean ± SEM (n = 10 – 11 mice per group) ** indicates significantly different (two-way RM ANOVA followed by Holm-Sidak post-hoc test: p = 0.008).

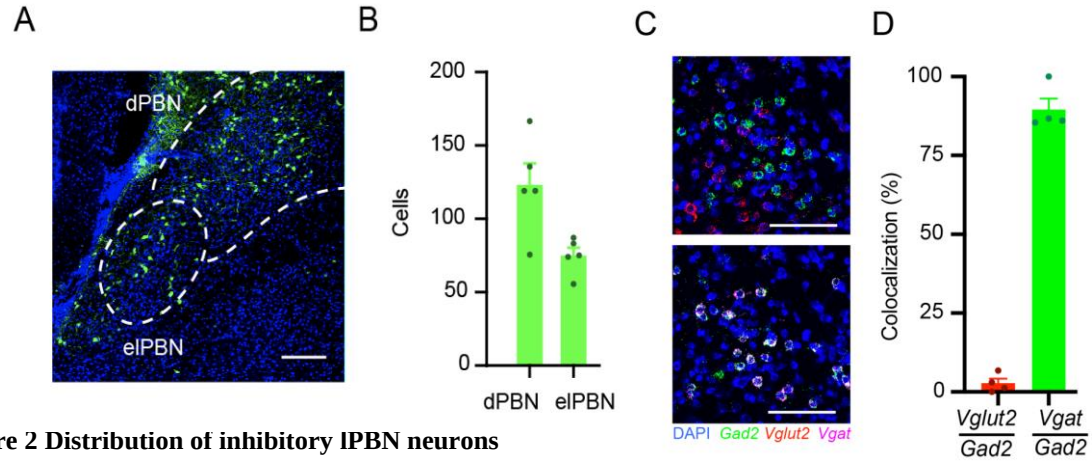

Figure 2 Distribution of inhibitory lPBN neurons

(A) Visualization of *Gad2*^{Cre} neurons in lPBN. Scale bar = 100 μm.

(B) Quantification of the number of *Gad2*^{Cre} neurons in dPBN vs. elPBN. (n = 5 mice).

(C) Representative image of FISH between *Vglut2* and *Gad2* (Top) or *Vgat* and *Gad2* (Bottom). Scale bar = 50 μm

(D) Quantification of colocalization between *Vglut2* and *Gad2* or *Vgat* and *Gad2*. n = 4 mice.

However, this hypersensitivity was significantly reduced when the lPBN was photostimulated in ChR2 mice compared to eYFP controls (Figure 1C). These data indicate that optogenetic activation of *Gad2* – expressing neurons in lPBN is sufficient to reduce mechanical hypersensitivity, suggesting that activity within the lPBN is required for mechanical allodynia.

Next, we used immunohistochemistry to determine the location and number of inhibitory neurons targeted through our viral strategy (Figure 2A – 2B). We found comparable numbers of inhibitory neurons expressing eYFP in dPBN compared to elPBN (123.1 ± 14.7 vs. 74.9 ± 5.4 neurons, respectively; paired Student's t test, $p = 0.063$). Furthermore, the number of neurons per unit area was not different (1856.4 ± 222.1 vs. 1791.9 ± 129.8 neurons per mm^2, respectively). To verify that these *Gad2* – expressing neurons indeed are inhibitory, we performed fluorescent in situ hybridization to visualize the colocalization of *Gad2* with either *Vglut2* or *Vgat* (Figure 2C). Roughly 3% of *Gad2*-positive neurons colocalized with *Vglut2*, whereas approximately 90% of *Gad2*-positive neurons colocalized with *Vgat* (Figure 2D). These data argue that the lPBN population expressing *Gad2* that we targeted indeed are inhibitory. Together, these data suggest that the $Gad2^{Cre}$ labels inhibitory neurons, and our optogenetic activation of the $Gad2^{Cre}$ lPBN neurons equally targeted both dPBN and elPBN inhibitory subpopulations.

Given the necessity of the lPBN for this pain behavior, we next explored its efferent targets. Towards this end, an AAV encoding a Cre-GFP fusion protein was stereotaxically delivered into the lPBN of transgenic mice harboring two Cre-dependent alleles: ReaChR-mCitrine, for the purpose of visualizing axonal projections, and synaptophysin-tdTomato, for the purpose of visualizing presynaptic terminals (Figure 3A). We observed lPBN efferent projections to numerous regions of the brain (Figure 5), consistent with previous studies (Bernard et al., 1996; Bernard et al., 1994; Gauriau and Bernard, 2002a; Saper and Loewy, 1980). However, four targets

in particular stood out due to the robust projections from mCitrine-labeled axons and dense puncta from tdtomato-labeled synaptic terminals: the BNST, the CEA, the VMH, and the lPAG (Figures 3B and 3C). Quantification revealed that all four of these regions received significant synaptic input from the lPBN (Figure 3D), though the apparent perisomatic input to the BNST and CEA (arrows) was qualitatively different from the diffuse input observed within the VMH and lPAG

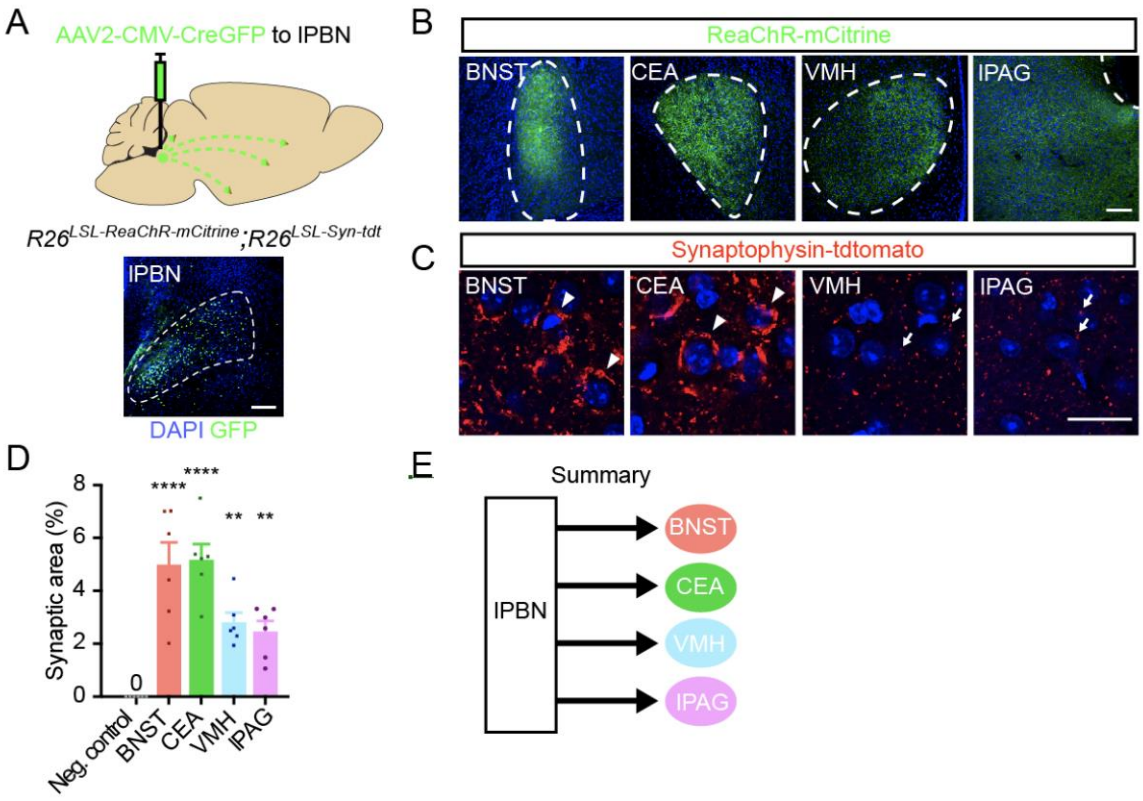

Figure 3 lPBN projects to four major targets.

(A) Experimental design and representative image of strategy to visualize lPBN neurons, their projections, and their presynaptic terminals. An AAV encoding a Cre-GFP fusion protein was targeted to the lPBN into mice harboring two Cre-dependent alleles, $R26^{LSL\text{-}ReaChR\text{-}mCitrine}$ and $R26^{LSL\text{-}Syn\text{-}tdt}$. Scale bar = 100 μm.

(B) Projections of the lPBN efferents to four different brain regions, as visualized with ReaChR- mCitrine: BSNT, CEA, VMH and lPAG. Scale bar = 100 μm. Images are representative of results from 6 mice.

(C) Synaptic terminals of lPBN efferents at four indicated targets, as visualized with Synaptophysin-tdtomato. Scale bar = 25 μm. Arrowheads and arrows denote perisomatic and diffuse input, respectively.

(D) Quantification of synaptic input. The relative synaptic input from lPBN was estimated by quantifying the area of synaptophysin-tdtomato expression within the indicated target. Motor cortex, which exhibits no synaptophysin-tdtomato expression, was used as negative control. Data are mean ± SEM and dots represent data points from individual animals (n = 6 mice). Asterisks indicate significantly different than negative control region (one-way RM ANOVA followed by Holm-Sidak post-hoc test; ** $p < 0.01$, **** $p < 0.001$).

(E) Summary diagram depicting four major efferent targets of lPBN.

(arrowheads; Figure 3C). Together, these data indicate that the BNST, CEA, VMH, and lPAG are four principle efferent targets of the lPBN (Figure 3E).

The observation that lPBN targets four principle downstream targets led us to wonder whether the reduction in mechanical allodynia during optogenetic stimulation of inhibitory lPBN neurons could be mediated through mechanisms downstream of lPBN. We therefore visualized the projections of *Gad2*^{Cre} lPBN neurons through stereotaxic injections of cre-dependent AAV encoding ChR2-eYFP (Figure 5). We found axon terminals from *Gad2*^{Cre} neurons primarily in BNST, CEA, VMH, and lPAG (Figure 4A). However, the relative projection intensity was less than that when the total lPBN population as targeted (Figure 4B). This argues that the majority of lPBN outputs are excitatory.

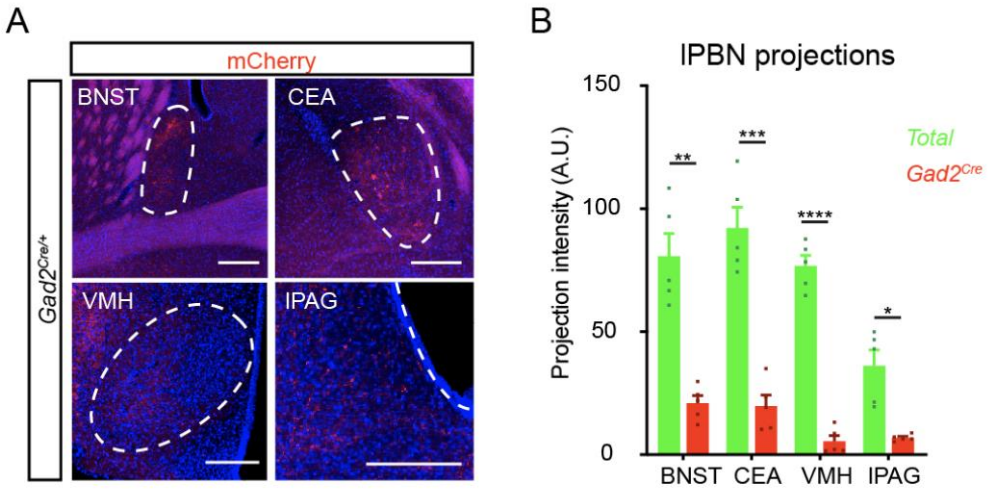

Figure 4 Inhibitory lPBN projections to four major targets.

(A) *Gad2-cre* neurons in lPBN project to BNST, CEA, VMH, and lPAG.

(B) Quantification of projection intensity from all lPBN or *Gad2*^{Cre} neurons to BNST, CEA, VMH, and lPAG. (n = 5 mice, two-way RM ANOVA followed by Holm-Sidak post-hoc test; * $p < 0.05$; ** $p < 0.01$; *** $p < 0.001$; **** $p < 0.0001$).

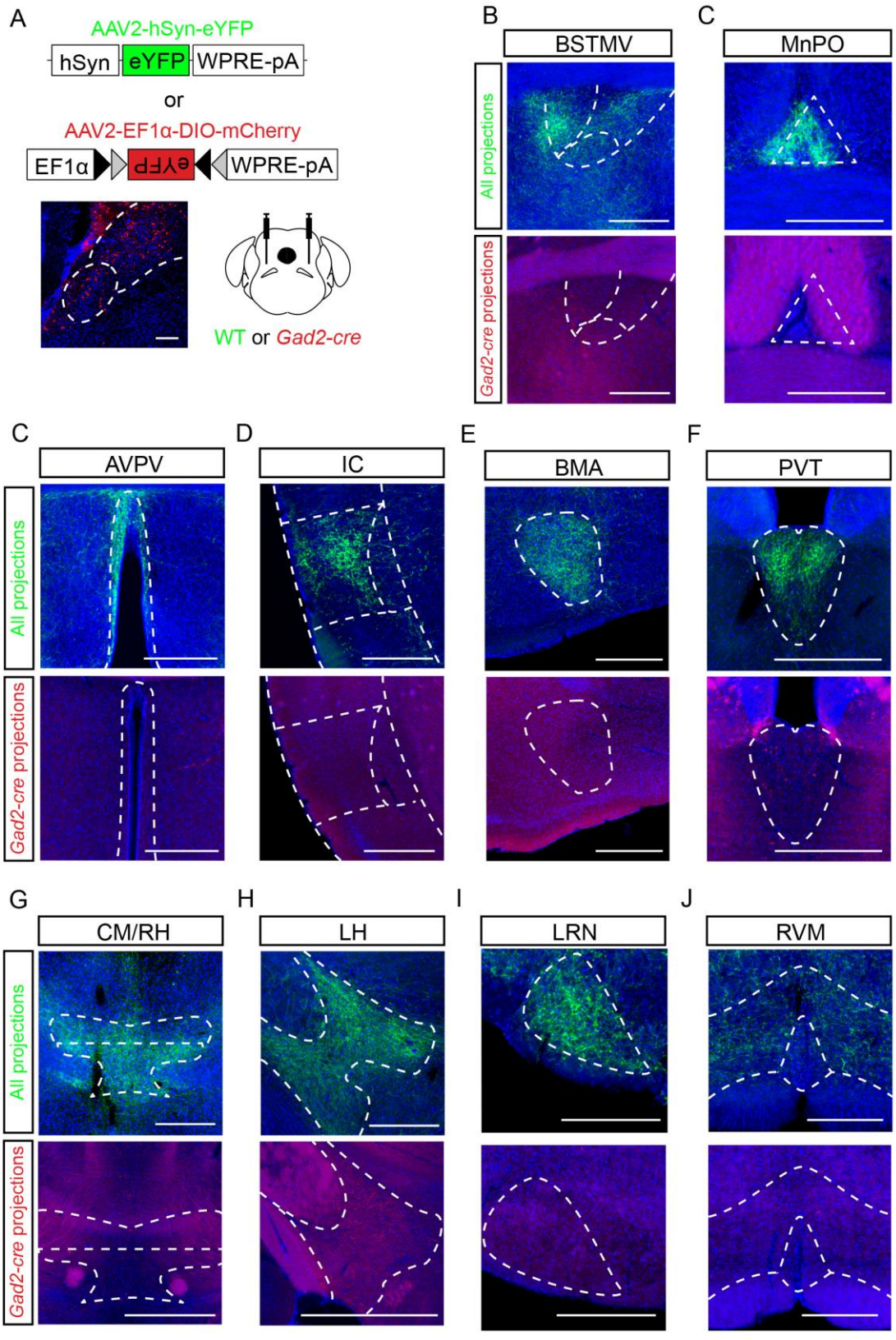

Figure 5 Efferents from the lPBN target numerous brain regions.

Efferents from the lPBN targets numerous brain regions, as visualized following stereotaxic injection of an AAV encoding eYFP into the lPBN (0.2 μl, bilateral).

(A) Graphical illustration of viral delivery approach to target all lPBN neurons (top) or an inhibitory subset expressing *Gad2*^{Cre} (bottom).

(B) Medial ventral division of bed nucleus stria terminalis (BNSTMV).

(C) Median preoptic nucleus (MnPO).

(D) Anteroventral periventricular nucleus (AVPV).

(E) Insular cortex.

(F) Basomedial amygdaloid nucleus (BMA).

(G) Paraventricular thalamic nucleus (PV).

(H) Centromedial thalamic nucleus (CM) and rhomboid nucleus (RH).

(I) Lateral hypothalamus (LH).

(J) Lateral reticular nucleus (LRN).

(K) Rostral ventromedial medulla (RVM). Scale bar = 200 μm (B - K)

2.3.2 Anatomical characterizations of collateral output pathways from the lPBN

Next, we sought to investigate the cellular basis of these efferent projections in more detail. In particular, we considered whether there might be parallel pathways originating from distinct cell types within the lPBN (Figure 6A), which would be consistent with previous work suggesting that distinct subdivisions of the LBPN have distinct projection patterns (Fulwiler and Saper, 1984; Saper and Loewy, 1980). Alternatively, given that at least some lPBN efferents are known to collateralize (Tokita et al., 2010), we also considered the possibility of a single major output from the lPBN with multiple targets (Figure 6B). To distinguish between these possibilities, we characterized the projections from the lPBN using cholera toxin B subunit (CTB) as a retrograde tracing tool (Figure 6C). Intriguingly, we found that stereotaxic injection of CTB into distinct

lPBN targets labeled neuronal cell bodies in different sub-regions of the lPBN: retrograde tracing from BNST or CEA resulted in labeled neurons within the elPBN, whereas retrograde tracing from VMH or lPAG labeled neurons within the dPBN (Figure 6D). These findings suggested the existence of at least two populations of efferent neurons with distinct targets.

To further explore this idea, we performed dual retrograde labeling experiments, placing distinct CTB conjugates into different target regions through stereotaxic injections. Following dual targeting of CEA and BNST, we found that ~40% of labeled neurons in the lPBN were double-labeled with both CTB-conjugated fluorophores (Figure 6E). Analogously, following dual injection into the VMH and lPAG, ~30% of CTB-containing neurons in the lPBN were double-labeled (Figure 6F). In contrast, there was almost no double labeling of lPBN neurons upon dual injections into any of the other four pair-wise combinations (Figures 6G, 6H, 6I and 6J). Together, these data define two major efferent pathways from the lPBN that exhibit collaterals: one originating from the dPBN that collateralizes to the VMH and lPAG, and a second arising from the elPBN that collateralizes to the BNST and CEA (Figure 6K).

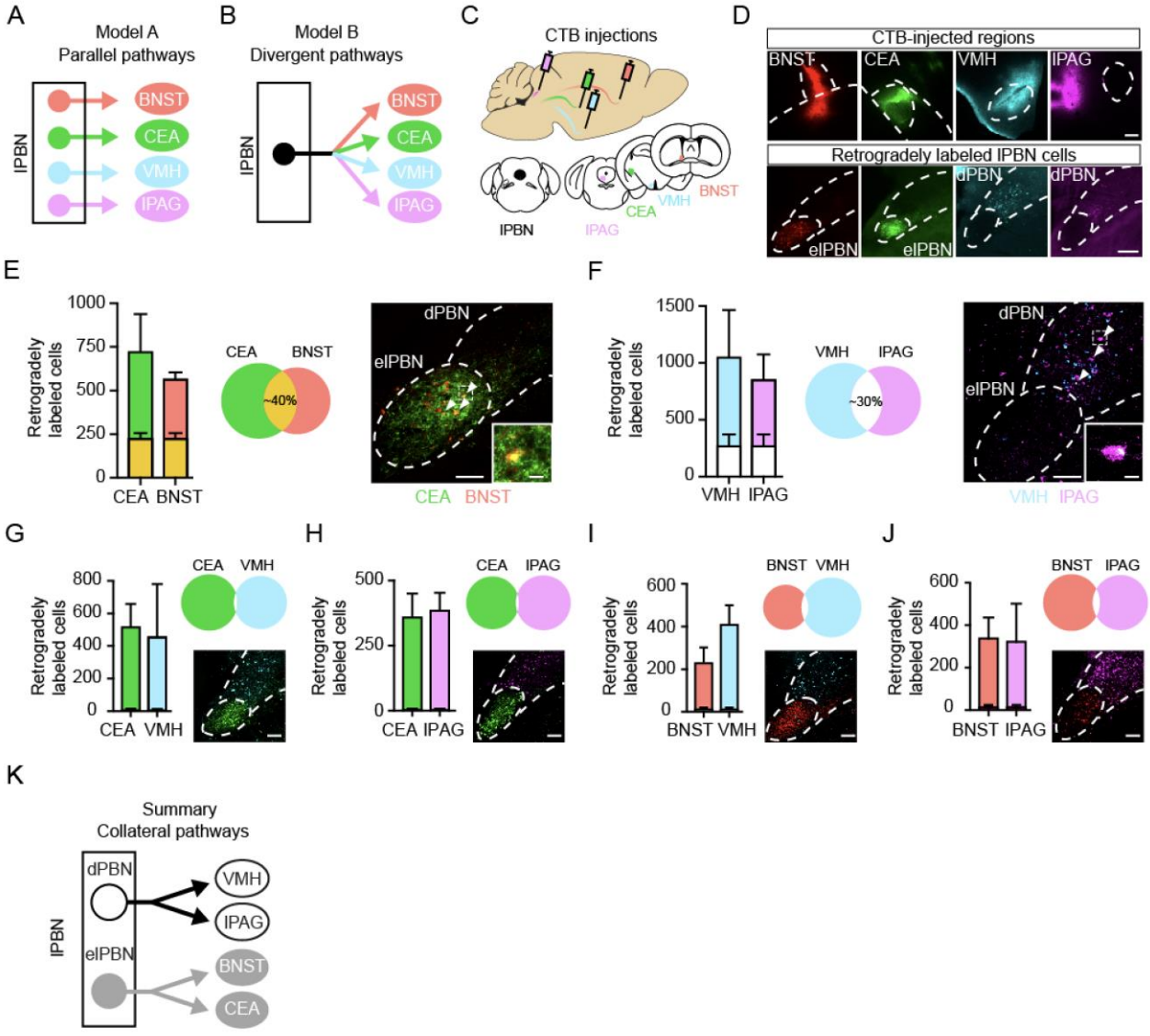

Figure 6 Distinct subpopulations of lPBN collateralize to different forebrain regions

(A-B) Models illustrating lPBN efferents as parallel (A) or divergent pathways (B).

(C) Experimental strategy to retrogradely label lPBN efferents with fluorophore-congugated CTB.

(D) CTB injections into efferent targets (top) and retrogradely labeled cells (bottom) in elPBN (BSNT and CEA) and dPBN (VMH and lPAG). Scale bars = 100 μm.

(E) Dual injection of CTB into CEA (green) and BNST (red) resulted in colocalized signal in approximately 40% of retrogradely labeled cells (yellow) across entire lPBN. Data are mean ± SEM (n = 4 mice). Arrows highlight co-labeled cells. Scale bar = 50 μm. Magnification shown in inset. Scale bar = 10 μm.

(F) Dual injections of CTB into VMH (blue) and lPAG (purple) resulted in colocalized signal in 30% of retrogradely labeled cells (white) across entire lPBN. Data are mean ± SEM (n = 4 mice). Arrows highlight co-labeled cells. Scale bar = 50 μm. Magnification shown in inset. Scale bar = 10 μm. (G-J) Very few dual-labeled neurons were observed following dual CTB injections into: CEA and VMH (G); CEA and lPAG (H); BNST and VMH (I); or BNST and lPAG (J). Data are mean ± SEM (n = 3 - 4 mice). Scale bar = 50 μm.

(K) Summary diagram illustrating two collateral pathways emerging from lPBN.

2.4 Discussion

In this chapter we provided evidence demonstrating two distinct pathways emanating from the lPBN. We identified robust terminal endings in four downstream regions that we characterized as major efferent pathways. Retrograde labeling from these regions identified spatially distinct lPBN subpopulations that collateralize to these downstream targets. Those from the dPBN collateralize to the VMH and lPAG, whereas a separate subpopulation from elPBN collateralize to BNST and CEA. These anatomical tracing studies suggest that divergent pathways from lPBN may underlie functionally distinct pathways that govern different aspects of behavior. Furthermore, we used genetically engineered mice expressing Cre recombinase in a subset of inhibitory lPBN neurons under the *Gad2* promoter, thereby allowing us to virally target and optogenetically activate this population to determine their functional contributions in a test of acute pain. This experiment revealed transient and reversible reduction in mechanical hypersensitivity through the activation of *Gad2*-expressing inhibitory neurons.

A novel finding through our experiment was the ability to reduce mechanical hypersensitivity through the activation of an inhibitory lPBN population. Prior work on lPBN

circuitry and function have previously described predominantly excitatory populations within lPBN that respond to nociceptive stimuli (Guthmann et al., 1998; Yokota et al., 2007). Furthermore, these excitatory populations, some of which project to downstream forebrain regions, serve integral roles in mediating different aspects of nociceptive behavior (Barik et al., 2018; Chen et al., 2018). As the inhibitory populations within downstream targets, such as the BNST and CEA, have been well-described (Babaev et al., 2018; Fadok et al., 2017; Gungor and Pare, 2016; Li et al., 2013), the modulation of these excitatory lPBN outputs have been either implicated to occur at these downstream regions or arise from inhibitory inputs onto lPBN excitatory neurons, thus painting an unappreciated role of inhibitory lPBN subsets in modulating lPBN activity. It is important to make clear that the lPBN exhibits dense GABA-immunoreactive varicosities, indicating that the lPBN is under strong GABAergic inhibition capable of suppressing lPBN activity (Coizet et al., 2010; Guthmann et al., 1998). However, whether this inhibitory regulation arises from local interneurons remains to be determined. Characterizing the morphology of *Gad2*^{Cre} lPBN neurons would provide insight into the ability of these neurons to broadly inhibit lPBN activity and subsequent pain behavior as these neurons are broadly distributed throughout lPBN.

Interestingly, we found that not all *Gad2*-expressing population were local interneurons as indicated by the presence of projections to a few downstream forebrain targets. In contrast, anatomical tracing data from the Allen Brain Institute indicate much sparser to no projections to these regions (Experiment: 303535149, http://connectivity.brain-map.org/). This is not entirely inconsistent with our findings, as the difference is likely a result of the greater number of inhibitory neurons within lPBN that were targeted in our experiment compared to those performed at the Allen Brain Institute. This leaves open the possibility of whether the observed increase in paw

withdrawal threshold was mediated through the optogenetic activation of local *Gad2*-positive neurons or *Gad2* – expressing projection neurons. However, the relative proportion of inhibitory projections to forebrain targets are small compared to those of the excitatory population, suggesting that the reduction in mechanical allodynia when photoactivating the lPBN inhibitory population likely arises from the activity of local inhibitory interneurons within lPBN. Lastly, our viral delivery and optical fiber implantations were localized to the PBN complex, further supporting our interpretation that the reduction in mechanical hypersensitivity resulted from lPBN $Gad2^{Cre}$ interneuron activity and not inhibitory neurons from adjacent brain structures.

An additional novel finding from these experiments is the collateralization of distinct lPBN subpopulations. We described results in which two distinct subdivisions of lPBN collateralize to separate targets. Roughly 30% of backlabeled dPBN neurons collateralize to both VMH and lPAG, whereas 40% of backlabeled elPBN neurons collateralizes to BNST and CEA. Although previous anatomical characterizations of lPBN efferents have demonstrated that these projections arise from distinct subdivisions of lPBN, few have characterized the collateralization of these efferent pathways and, to our knowledge, the degree of colocalization among these lPBN projection neurons has not been reported (Sarhan et al., 2005). Liang et al. 2016 retrogradely labeled from CEA and PVT and found less than 10% of cells colocalized compared to the 40% colocalization of BNST- and CEA-projecting lPBN neurons in our experiments (Liang et al., 2016a). It is important to raise the technical concern that these retrograde tracing approaches do not definitively label all lPBN projection neurons. Thus, it is possible that the 30% dPBN- and 40% elPBN- labeled neurons may be an underestimate of the total number of collateralizing neurons. Nevertheless, these data suggest that the lPBN population collateralizing between BNST and CEA, and those between VMH and lPAG, may indeed be major, unique subsets of lPBN neurons that convey

interoceptive or exteroceptive input from the periphery to forebrain structures. Although the availability of different retrograde tools has limited the number of collateralizations we could characterize in our experiments, we imagine that lPBN subsets may exhibit more than two collateral emergent pathways.

An important detail not addressed in our tracing studies is the neurochemical composition of collateralizing pathways. Although the cytoarchitectural territories and divisions of lPBN have been carefully and thoroughly detailed (Fulwiler and Saper, 1984; Saper and Loewy, 1980), these subregions have yet to be categorized into genetically distinct cell types. The generation of genetically engineered mice harboring the Cre recombinase allele has permitted local, targeted delivery of transgenes into specific subsets of neurons within a heterogeneous population. Within the lPBN, the most notable is the *Calca*^{Cre} allele in which Cre recombinase has been targeted to the *Calca* locus encoding CGRP (Carter et al., 2013; Rosenfeld et al., 1983). Tracing studies have demonstrated that CGRP-positive neurons reside almost exclusively within the elPBN and project to several forebrain targets including BNST and CEA (Chen et al., 2018). In a separate study, nearly all CEA- and PVT- projecting lPBN neurons expressed CGRP (Liang et al., 2016b). Thus, it is very likely that the elPBN neurons collateralizing to BNST and CEA we characterized also overlap to a significant degree with CGRP. On the other hand, the neurochemical identity of dPBN subpopulations has not been as thoroughly characterized. In Chapter 4, we identified a subset of dynorphin-expressing neurons in dPBN using *Pdyn*^{Cre} mice. However, they are unlikely to represent the subpopulation of neurons collateralizing to VMH and lPAG because anatomical tracing revealed no projections to VMH (data not shown). Further studies are warranted to determine the various cell types within each subdomain of the lPBN.

3.0 Activity of divergent lateral parabrachial pathways compose the nocifensive response

3.1 Introduction

Our work and previous studies have demonstrated segregated subpopulations within lPBN that give rise to different projection patterns, suggesting such outputs regulate different aspects of behavior in response to interoceptive and exteroceptive signals (Fulwiler and Saper, 1984; Liang et al., 2016b; Saper and Loewy, 1980; Tokita et al., 2010). Although there is general agreement that lPBN likely serves as a homeostatic alarm to notify an animal of potential danger from a diverse range of stimuli (Palmiter, 2018; Saper, 2016), the functional role of specific efferent pathways to downstream targets remains to be fully explored. The CGRP-expressing population in the elPBN, which has been the most well-described, projects to numerous downstream regions that, through redundant pathways, encode conditioned aversion to unpleasant or threatening stimuli (Chen et al., 2018; Han et al., 2015a). A partially overlapping population expressing the neuropeptide Tac1 exhibits similar projection patterns. However, its connections with the RVM trigger nocifensive behavior in response to noxious heat (Barik et al., 2018). The functional contributions to pain responses of the remainder of projections to numerous forebrain regions have yet to be characterized. In this chapter, we designed experiments to activate specific projections from elPBN and evaluate their effects on behavior in vivo.

3.2 Methods

3.2.1 Animals

Mice were given free access to food and water and housed under standard laboratory conditions. The use of animals was approved by the Institutional Animal Care and Use Committee of the University of Pittsburgh. Wild-type C57BL/6 mice were obtained from Charles River (Cat # 027). For all experiments 8 – 16 week-old male and female mice were used. In all cases, no differences between male and female mice were observed and so the data were pooled.

3.2.2 Viruses

The following viruses were used for experimentation: AAV2-hsyn-eYFP (Addgene: 50465) and AAV2-hSyn-hChR2(H134R)-eYFP (Addgene: 26973). Viruses were purchased from University of North Carolina Vector Core.

3.2.3 Stereotaxic injections and optical fiber implantation

Stereotaxic injections and optical fiber implantations were performed as described in the previous chapter. Wildtype mice were bilaterally injected with 0.2 μl virus. The injection needle was left in place for an additional 5- 10 min and then slowly withdrawn. Injections and optical fiber implantations were performed bilaterally at the following coordinates for each brain region: BNST: AP +0.50 mm, ML ± 1.00 mm, DV -4.30; CEA: AP -1.20 mm, ML ± 2.85 mm, DV -4.50; VMH: AP -1.48 mm ML ± -0.50 mm DV -5.80 mm; lPAG: AP -4.70 mm, ML ± 0.74 mm, DV: -

2.75; and lPBN AP -5.11 mm, ML ± 1.25 mm, DV: -3.25. For implantation of optical fibers (Thor Labs: 1.25 mm ceramic ferrule 230 μm diameter), implants were slowly lowered 0.300-0.500 mm above the site of injection and secured to the skull with a thin layer of Vetbond (3M) and dental cement. The incision was closed using Vetbond and animals were given a subcutaneous injection of buprenorphine (0.3mg/kg) and allowed to recover over a heating pad. Mice were given 4 weeks to recover prior to experimentation.

3.2.4 Immunohistochemistry

Immunohistochemistry was performed as described in the previous chapter. Primary antisera were incubated for 14 hours overnight at 4°C: chicken anti-GFP (1:1K) and rabbit anti-Fos (1:5K). Sections were subsequently washed three times for 20 minutes in wash buffer (1% donkey serum, 0.1% triton, 0.3M NaCl) and incubated in secondary antibodies (Life Technologies, 1:500) at room temperature for two hours. Sections were then incubated in Hoechst (ThermoFisher, 1:10K) for 1 minute and washed 7 times for 15 minutes in wash buffer, mounted and coverslipped.

3.2.5 Image acquisition and quantification

Full-tissue thickness sections were imaged using either an Olympus BX53 fluorescent microscope with UPlanSApo 4X, 10X, or 20X objectives or a Nikon A1R confocal microscope with 20X or 60X objectives. All images were quantified and analyzed using ImageJ. For all images, background pixel intensity was subtracted as calculated from control mice. To quantify

Fos-labeled cells, 65 μm sections of the entire lPBN were imaged using the fluorescent microscope and images manually counted in a blinded manner.

3.2.6 Fos induction (optogenetics)

To induce Fos in optically implanted mice, mice were photostimulated at 10 mW, 20 Hz, and 5 ms pulse duration for 20 minutes at a 3 seconds on, 2 seconds off stimulation pattern and subsequently perfused 90 minutes after the initial onset of photostimulation as noted for immunohistochemistry. 65 um thick transverse sections of brain were collected on a vibratome and processed free-floating for immunohistochemistry as detailed above. To quantify Fos-labeled cells, we identified the center of each full-thickness tissue section and imaged 3 optical planes that were 10 μm apart. These images were subsequently merged into a single layer and counted for each region of interest (lPBN, BNST, CEA, VMH, and lPAG).

3.2.7 Behavior

All assays were performed and scored by an experimenter blind to virus (eYFP or ChR2). Post hoc analysis confirming specificity of viral injections and proper fiber implantation were also performed blinded to animal identity, and mice in which viral injections and/or fiber implantation were considered off target excluded from analysis. All testing was performed in the University of Pittsburgh Rodent Behavior Analysis Core. Optogenetic stimulation parameters were determined empirically as follows: 10 mW, 20 Hz, 5 ms duration pulses.

Real time place aversion assay (RTPA)

Mice were stereotaxically injected with either channelrhodopsin or control eYFP virus and optical fibers implanted at the downstream terminals of interest. Four weeks following injection mice were habituated to a custom-made 2-chamber (40cm x 28cm x 20cm chamber) for real time place aversion testing. Mice were habituated on day 1 for 20 minutes and subsequently tested the next day for 20 minutes. Light stimulation was delivered whenever the mouse entered one of two sides of the chamber and turned off when the animal exited that chamber. The side of stimulation was counterbalanced. The behavior was recorded and post-hoc analysis performed to determine body position using the open source software Optimouse (Ben-Shaul, 2017). Position data were discarded according to established criteria, and velocity was computed as described here (https://www.biorxiv.org/content/10.1101/558643v1).

Tail immersion test

Mice were habituated to mouse restraints 15 minutes for 5 days before testing. Tails were immersed 3 cm into a water bath at 48°C or 55°C, and the latency to tail flick was measured three times per temperature with a 1 minute interval between trials. For optogenetic testing, mice were photostimulated for 10 seconds prior to tail immersion testing.

Escape response test

Mice were placed in an open field chamber and allowed to habituate for five minutes before two 30-second optogenetic stimulation bouts and two minute resting period between bouts. The behavior was recorded and post-hoc analysis performed to determine body position using the open source software Optimouse as described in RTPA.

Conditioned place aversion test

Mice were placed in a two-chamber plexiglass box for 20 minutes and allowed to freely roam between one of two sides differentiated by visual cues (spots versus stripes). For two conditioning days, mice were restricted to one of two sides and received either no stimulation or photostimulation (3 seconds on, 2 seconds off at 20Hz, 5ms pulse duration, 10mW) for 20 minute periods in the morning and afternoon. On the test day, mice were placed back into the box and allowed to freely explore either chamber. The behavior was recorded and post-hoc analysis performed to determine body position using the open source software Optimouse as described in RTPA. For formalin-induced CPA, mice were conditioned to 2% 10µl solution of formalin injected into either one hindpaw on the first day of conditioning and the contralateral hindpaw on the second day of conditioning. Control mice received no hindpaw injections.

3.2.8 Statistical analysis

All statistical analyses were performed using GraphPad Prism 7.0. Values are presented as mean ± SEM. Statistical significance was assessed using Fisher's exact test for categorical data, Students t-test, or two-way repeated measures ANOVA followed by Holm-Sidak post-hoc test. Significance was indicated by $p \leq 0.05$. Sample sizes were based on pilot data and are similar to those typically used in the field.

3.3 Results

3.3.1 dPBN projections and nociceptive behavior

Our two main findings from the previous chapter, that 1) the activity of inhibitory lPBN neurons can reduce mechanical allodynia and 2) distinct subdivisions of the lPBN collateralize to different targets, led us to ask whether distinct outputs from the lPBN underlie different components of the nocifensive response. To address this question, we targeted the lPBN with AAVs encoding either ChR2 or eYFP and implanted optical fibers above distinct efferent targets, thereby enabling pathway-selective stimulation (Figure 7A). For each mouse, behavioral experiments and post-hoc analysis of tissue for infection specificity in the lPBN and optical placement over the efferent target were performed in a blinded manner.

Several lines of evidence suggest that nociceptive threshold is determined, at least in part, by descending modulation from brain structures such as the PAG that are activated by ascending nociceptive circuitry (Basbaum and Fields, 1978). To explore whether any of the efferent projections from the lPBN are sufficient to activate descending inhibition, we assessed whether optogenetic stimulation affected the latency to withdraw in the tail flick assay, which measures a spinal reflex to noxious heat (Figure 7B). At baseline, ChR2-expressing mice exhibited similar tail flick latencies compared to eYFP controls. However, immediately following optogenetic activation of dPBN projections to lPAG, ChR2-expressing mice showed a significant increase in tail flick latency (Figure 7C). Indeed, over half of these mice reached cut-off, which was imposed to prevent tissue damage. In contrast, photostimulation of projections to other efferent targets had either no significant effect (VMH or CEA) or only a small effect (BNST) (Figures 8A, 8B and

8C). Thus, activation of the efferent pathway from the lPBN to the lPAG is sufficient to elicit robust analgesia that likely activating descending inhibition.

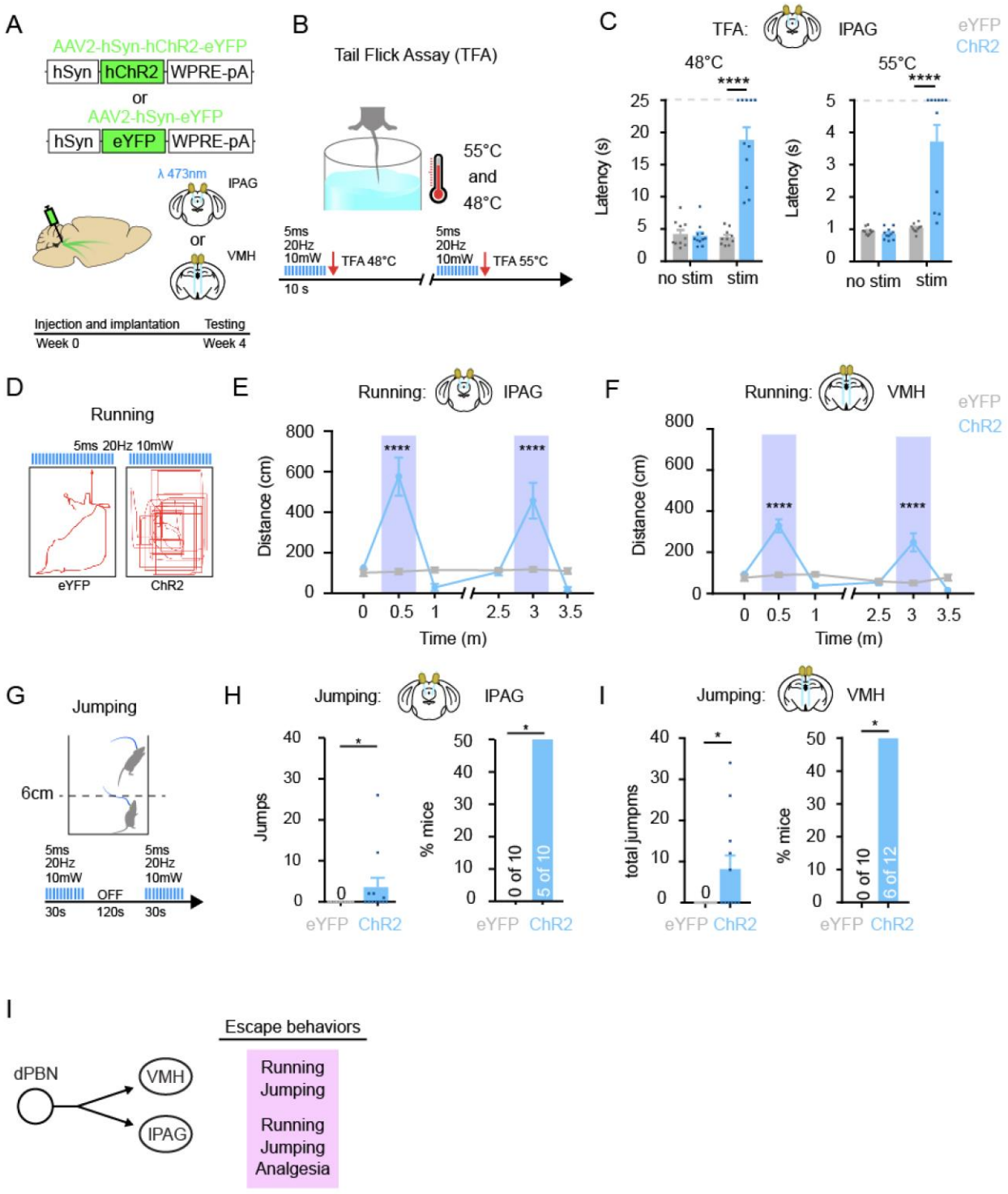

Figure 7 Efferent dPBN projections to VMH and lPAG elicit escape-like behaviors

(A) Experimental strategy to selectively activate distinct lPBN projections. AAVs encoding either ChR2 or eYFP were injected into the lPBN and optical implants were placed above one of four efferent targets: lPAG, VMH, CEA or BNST.

(B) Experimental protocol for tail flick assay (TFA). Mice were photostimulated for 10 s immediately prior to TFA at either 48 °C and 55 °C.

(C) Photostimulation of dPBN terminals in lPAG significantly increases latency to tail flick at 48 °C and 55 °C. Data are mean ± SEM and dots represent data points from individual animals (n = 9 – 11 mice per group). **** indicates significantly different (Two-way RM ANOVA followed by Holm-Sidak post-hoc test; lPAG, $p < 0.0001$). Dotted lines indicate cut-off latencies that were imposed to prevent tissue damage.

(D) Experimental protocol for running assay. Stimulation paradigm and example traces of locomotion following stimulation of lPAG terminals from lPBN efferents in eYFP and ChR2 mice.

(E) Photostimulation of dPBN terminals in lPAG significantly increases locomotion. Data are mean ± SEM (n = 9 – 11 mice per group). **** indicates significantly different (Two-way ANOVA followed by Holm-Sidak post-hoc test, $p < 0.0001$)

(F) Photostimulation of dPBN terminals in VMH significantly increases locomotion. Data are mean ± SEM (n = 10 – 12 mice per group). **** indicates significantly different (Two-way ANOVA followed by Holm-Sidak post-hoc test, $p < 0.0001$).

(G) Experimental protocol for jumping assay. A minimum of 6 cm vertical movement of the body was considered a jump.

(H) Photostimulation of dPBN terminals in lPAG elicits significant jumping. Data are mean ± SEM and dots represent data points from individual animals (n = 9 – 11 mice per group). Left: * indicates significant number of jumps (Mann-Whitney; $p = 0.033$). Right: * indicates significant proportion of mice (Fisher's exact test: $p = 0.033$).

(I) Photostimulation of dPBN terminals in VMH elicits significant jumping. Data are mean ± SEM and dots represent data points from individual animals (n = 9 – 11 mice per group). Left: * indicates significant number of jumps (Mann-Whitney; $p = 0.015$). Right: * indicates significant proportion of mice (Fisher's exact test: $p = 0.015$).

(J) Summary diagram depicting behavioral responses observed upon stimulation of dPBN efferents to VMH and lPAG.

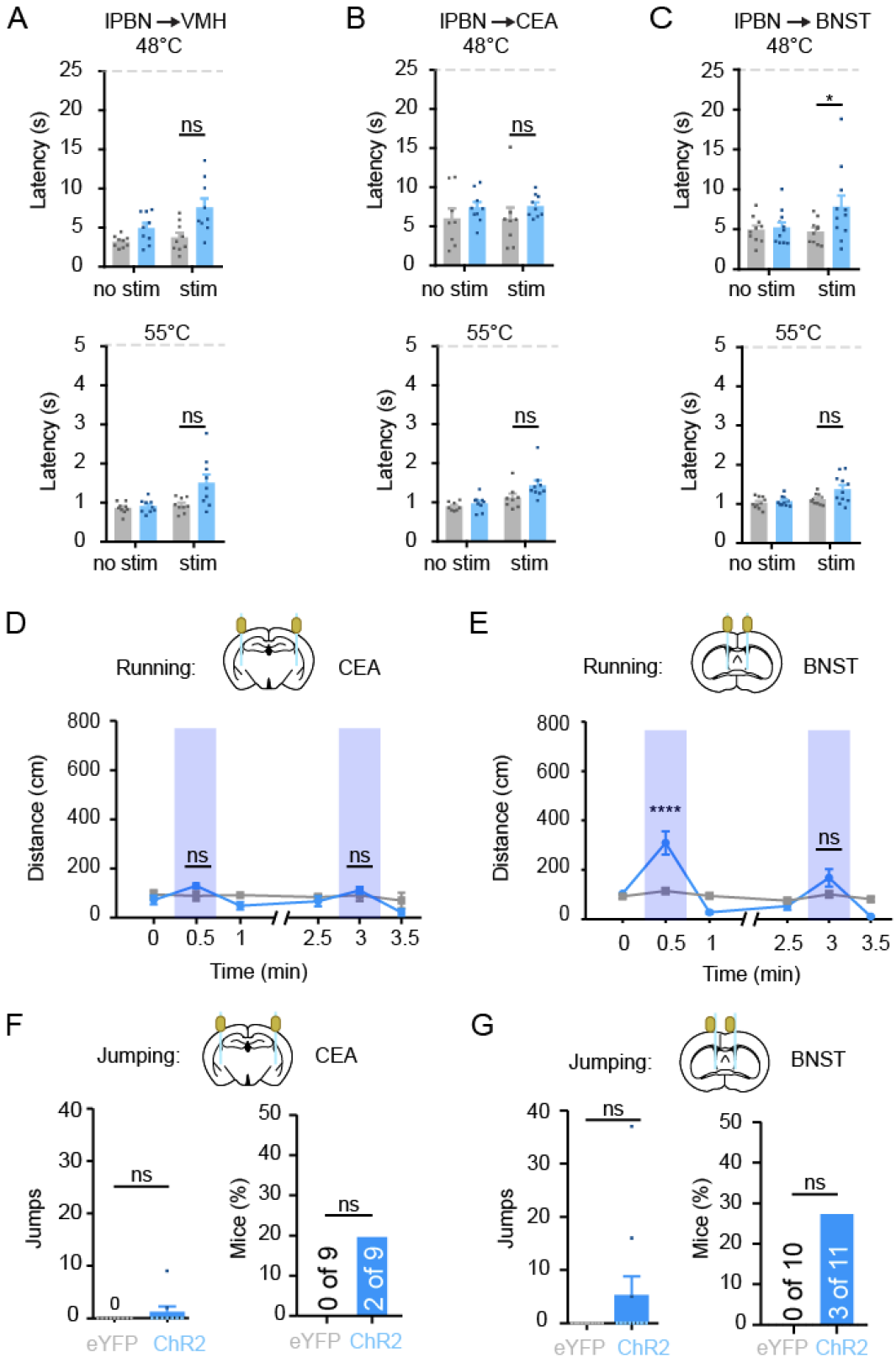

Figure 8 Effect of photoactivation of lPBN on descending modulation, running, and jumping.

(A-B) Optogenetic activation of terminals in VMH or CEA of ChR2-injected mice (blue bars) does not increase latency of tail flick response to low or high noxious heat compared to eYFP-expressing controls (grey). Data are mean ± SEM and dots represent data points from individual animals (n = 8 - 9 mice per group; ns, not significant $p > 0.05$, two-way RM ANOVA).

(C) Photostimulation of projections to BNST in ChR2-expressing mice (blue bars) increases latency to tail flick at 48 °C but not 55 °C compared to control mice (grey bars). Data are mean ± SEM and dots represent data points from individual animals (n = 10 - 11 mice per group; * indicates significant, two-way RM ANOVA followed by Holm-Sidak post-hoc test, $p = 0.03$).

(D) Optogenetic stimulation of terminals in CEA of ChR2-injected mice has no effect on lateral movement. Data are mean ± SEM (n = 8 – 9 mice per group; ns, not significant, two-way RM ANOVA, $p > 0.05$).

(E) Optogenetic stimulation of terminals in BNST promotes significant lateral movement in the first but not second bout of photostimulation. Data are mean ± SEM (n = 10 - 11 mice per group, **** indicates significant difference, two-way RM ANOVA followed by Holm-Sidak post-hoc test, $p < 0.0001$).

(F - G) The number of jumps or proportion of mice exhibiting jumping was not significantly higher in ChR2-expressing mice that were stimulated in CEA or BNST compared to eYFP controls (Mann-Whitney t-test: CEA: $p = 0.47$; BNST: $p = 0.21$, Fisher's exact test: CEA: $p = 0.47$; BNST: $p = 0.21$). Data are mean ± SEM and dots represent data points from individual animals (n = 9 - 11 mice per group).

Over the course of these studies, we noted that activation of some efferent pathways elicited motor behaviors. To examine this phenomenon in more detail, we quantified the lateral (Figure 7D; running) and vertical (Figure 7G; jumping) movements that were observed upon optogenetic stimulation. Activation of the efferent projection from the dPBN to the lPAG resulted in explosive running behavior that was time-locked to the light stimulus (Figure 7E). Likewise, stimulation of the projection to the VMH elicited dramatic increased in locomotion that began each time the light was turned on and ceased as soon as the light was turned off (Figure 7F). In contrast, photostimulation of efferent projections to the CEA caused no significant lateral movement

(Figure 8D), and that to the BNST showed significant lateral movement to the first stimulation only (Figure 8E). Thus, efferent projections from the dPBN were distinctive in their ability to elicit switch-like locomotor behavior in response to repeated stimulation.

Analogous results were found in the jumping assay, where significant effects were observed upon activation of efferents originating from the dPBN, but not the elPBN. Upon activation of projections to either the lPAG or the VMH, a significant proportion of mice (50%) jumped as many as 35 times over a minute of stimulation (Figures 7H and 7I). In contrast, jumping behavior upon activation of the efferent pathways to either the BNST or the CEA was not significantly different than that observed in eYFP controls (Figures 8F and 8G). Taken together, these finding suggest that the efferent pathways emanating from the dPBN are sufficient to elicit a group of behaviors — running, jumping and analgesia — that would enable escape in the context of injury or other threats (Figure 7I).

Optogenetic activation of terminal fields provides a method to study pathway-specific behaviors. However, a caveat of this technique is the possibility of back-propagation of action potentials that may result in antidromic activation of projections to other downstream targets. To confirm the specificity of circuit activation, thereby allowing us to correlate the observed behaviors to a specific lPBN projection, we analyzed the induction of Fos, a marker of neuronal activity, in response to optogenetic stimulation (Figure 9).

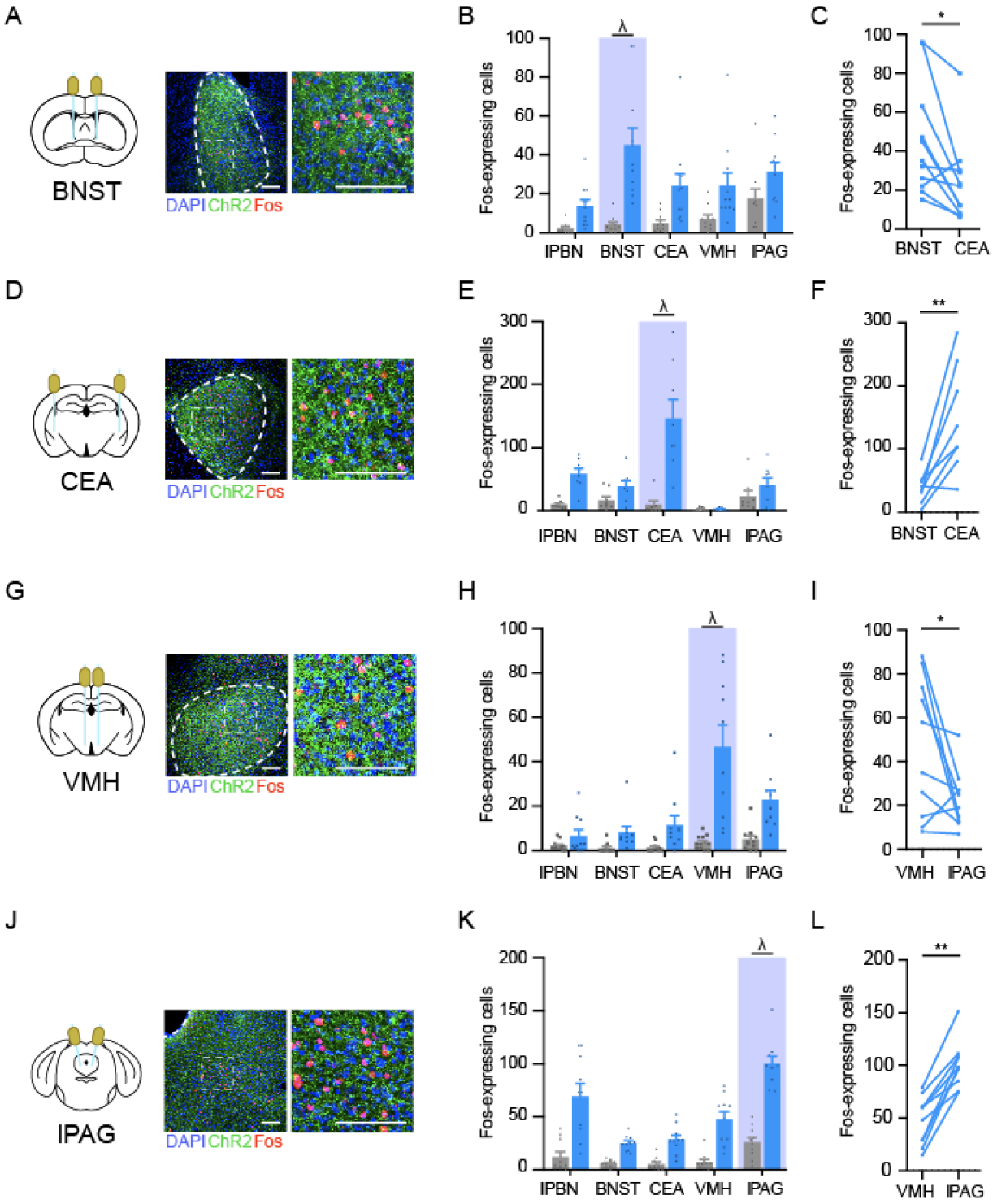

Figure 9 Pathway selective photostimulation of lPBN outputs

To assess the degree to which photstimulation of a specific lPBN efferent was selective, Fos induction was analyzed 90 min after photostimulation (20 min; 20 Hz, 5 ms pulses, 10 mW).

(A) Diagram and image of ChR2-expressing terminals and Fos-expressing cells in BNST.

(B) Fos induction in eYFP-expressing mice (control, grey) and ChR2-expressing mice (blue) upon photostimulation of lPBN efferent terminals in the BNST. Data are mean ± SEM and dots represent data points from individual animals (n = 8 - 11 mice per group).

(C) The number of Fos-expressing cells in BNST is significantly greater than that in CEA (paired Student's t-test $p = 0.01$, n = 11 mice).

(D) Diagram and image of ChR2-expressing terminals and Fos-expressing cells in CEA.

(E) Fos induction in eYFP- expressing mice (control, grey) and ChR2-expressing mice (blue) upon photostimulation of lPBN efferent terminals in the CEA. Data are mean ± SEM and dots represent data points from individual animals (n = 8 - 9 mice per group)

(F) The number of Fos-expressing cells in CEA is significantly greater than that in BNST (paired Student's t-test $p = 0.004$, n = 9 mice).

(G) Diagram and image of ChR2-expressing terminals and Fos-expressing cells in VMH.

(H) Fos induction in eYFP- expressing mice (control, grey) and ChR2-expressing mice (blue) upon photostimulation of lPBN efferent terminals in the VMH. Data are mean ± SEM and dots represent data points from individual animals (n = 10 - 11 mice per group).

(I) The number of Fos-expressing cells in VMH is significantly greater than that in lPAG (paired Student's t-test, $p = 0.04$, n = 10).

(J) Diagram and image of ChR2-expressing terminals and Fos-expressing cells in VMH.

(K) Fos induction in eYFP- expressing mice (control, grey) and ChR2-expressing mice (blue) upon photostimulation lPBN efferent terminals in the VMH. Data are mean ± SEM and dots represent data points from individual animals (n = 9 - 10 mice per group)

(L) The number of Fos-expressing cells in lPAG is significantly greater than that in VMH (paired Student's t-test $p = 0.004$, n = 9). Scale bar = 100 μm outer, 50 μm inner (A, D, G, J).

3.3.2 elPBN projections on aversive learning

Another important component of the response to noxious input is aversion that provides a salient cue to enable avoidance learning. We therefore addressed the degree to which efferent pathways from the lPBN elicit avoidance using a real-time place aversion assay (Figure 10A). As before, experiments were performed on mice in which AAVs encoding either ChR2 or eYFP had been stereotaxically injected into the lPBN and optical fibers were implanted above one of the four efferent targets — CEA, BNST, VMH or lPAG — to enable pathway-selective activation. Notably, regardless of which lPBN efferent pathways that was targeted, ChR2-expressing mice spent significantly less time on the side of the chamber in which they received photostimulation (Figures 10B, 10C, 4D, 10E and 10F).

Although this behavior was suggestive of aversion, we also considered the possibility that at least in some instances (i.e., VMH and lPAG) this apparent avoidance could simply be a consequence of optogenetically-induced locomotion. Thus, to more directly assess whether activation of efferent pathways from the lPBN was sufficient to enable associative conditioning, we used the conditioned place aversion (CPA) assay, in which optogenetic stimulation was selectively paired with one of the two chambers for 20 min on two consecutive days (Figure 10G). When activation of efferent projections to the CEA was the conditioning stimulus, ChR2-expressing mice spent significantly less time on the stimulation-paired side of the chamber (Figure 10H). Similarly, significant CPA was observed when activation of projections to the BNST was used as the conditioning stimulus (Figure 10I). In contrast, repeated photostimulation of efferent projections to either the VMH or the lPAG failed to induce CPA (Figures 11A and 11B). These findings suggest that, although activation of any of the the major outputs from the lPBN results (directly or indirectly) in real time place aversion (RTPA), only those projecting to the CEA or

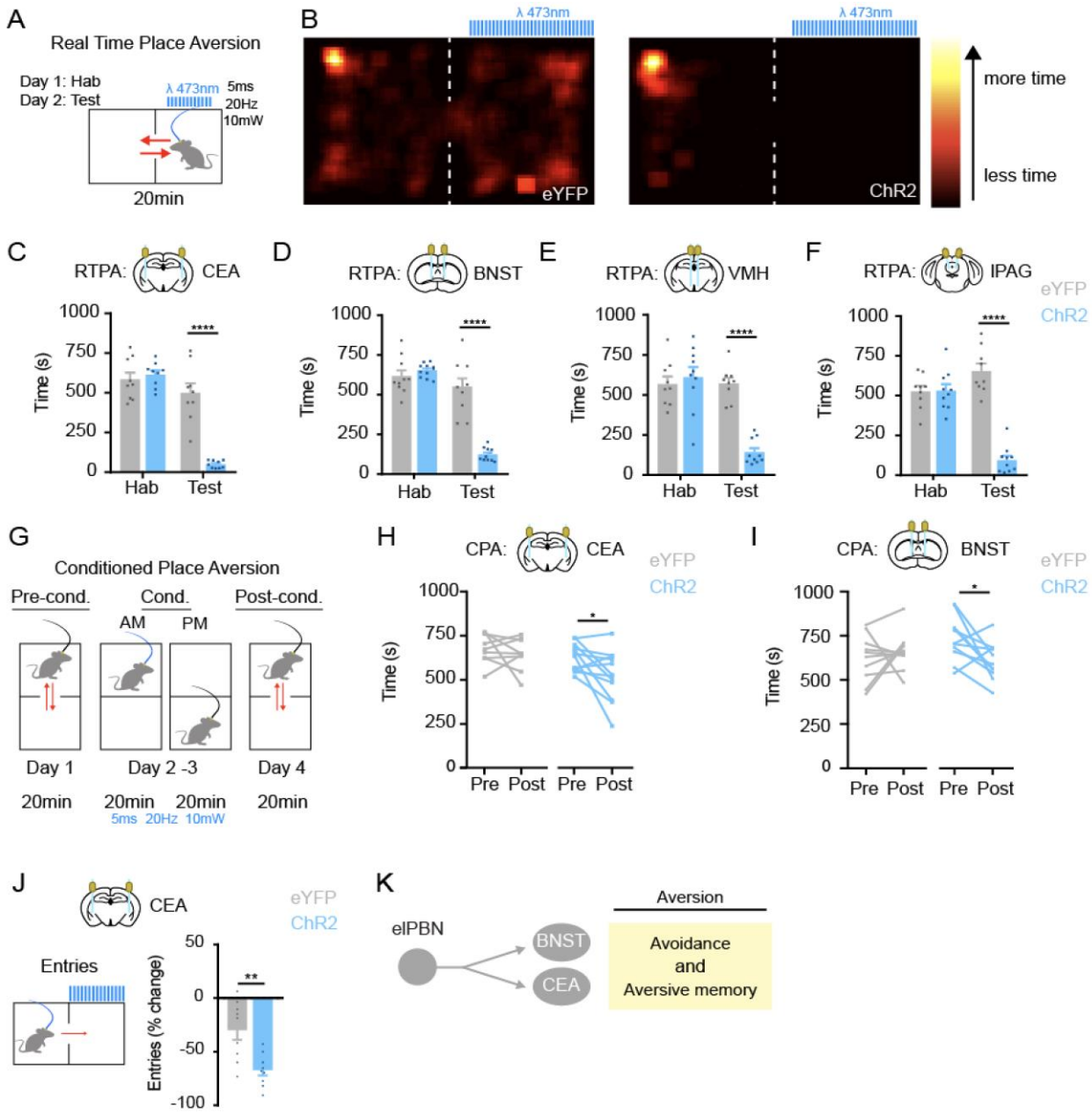

Figure 10 Efferent elPBN projections to BNST and CEA drive aversion.

(A) Experimental protocol for real time place aversion (RTPA) assay. Mice were habituated (Hab) for 20 min one day prior to testing (Test).

(B) Heat maps of time spent in RTPA chambers upon stimulation of lPBN terminals in CEA in eYFP (left) and ChR2 (right) mice.

(C-F) Time spent in photostimulation chamber during habituation phase (Hab) and testing phase (Test) in eYFP (grey) and ChR2 (blue) mice upon stimulation of lPBN efferent terminals in the CEA (C), BNST (D), VMH (E) or lPAG (F). Data are mean ± SEM and dots represent data points from individual animals (n = 9 – 11 mice per group for each experiment). **** Indicates ChR2 mice are significantly different than eYFP controls (Two-way RM ANOVA followed by Holm-Sidak post-hoc test, $p < 0.0001$).

(G) Experimental protocol for conditioned place aversion (CPA). Each session comprises 20 min in the CPA box.

(H-I). Photostimulation of elPBN efferent terminals in the CEA (H) or BNST (I) induces CPA. Data are from individual animals (n = 11 - 12 mice per group). * indicates significantly different (Paired Student's t-test: CEA: $p = 0.025$; BNST: $p = 0.028$).

(F) Entries into photostimulation chamber upon photostimulation of elPBN efferent terminals in the CEA terminals. ** indicates change in entry number between test phase and habituation phase is significantly different between eYFP and ChR2 mice (unpaired Student's t-test, $p = 0.003$).

(J) Summary diagram depicting behavioral responses observed upon stimulation of elPBN outputs to BNST and CEA.

BNST are sufficient for stable aversive learning. To further explore how quickly the mice learned to avoid the side of the chamber in which they receive optogenetic stimulation, we re-analyzed the real time place aversion data, quantifying number of entries into the light-paired chamber. Photostimulation of the efferent projection to the CEA significantly reduced the number of entries (Figure 10J), whereas activation of other efferent projections had no significant effect on entries (Figures 11C, 11D and 11E). These findings reinforce the role of projections to the CEA for avoidance learning because only this cohort of mice showed evidence of learning to avoid the light-paired chamber during the RTPA assay. Together, these data suggest that avoidance memory can be elicited by efferent pathways from the elPBN (Figure 10K), consistent with previous studies (Campos et al., 2018; Chen et al., 2018; Han et al., 2015a; Sato et al., 2015).

Similar to our previous experiment to dissect circuit function of dPBN outputs, we verified the specificity of elPBN circuit photoactivation (Figure 9).

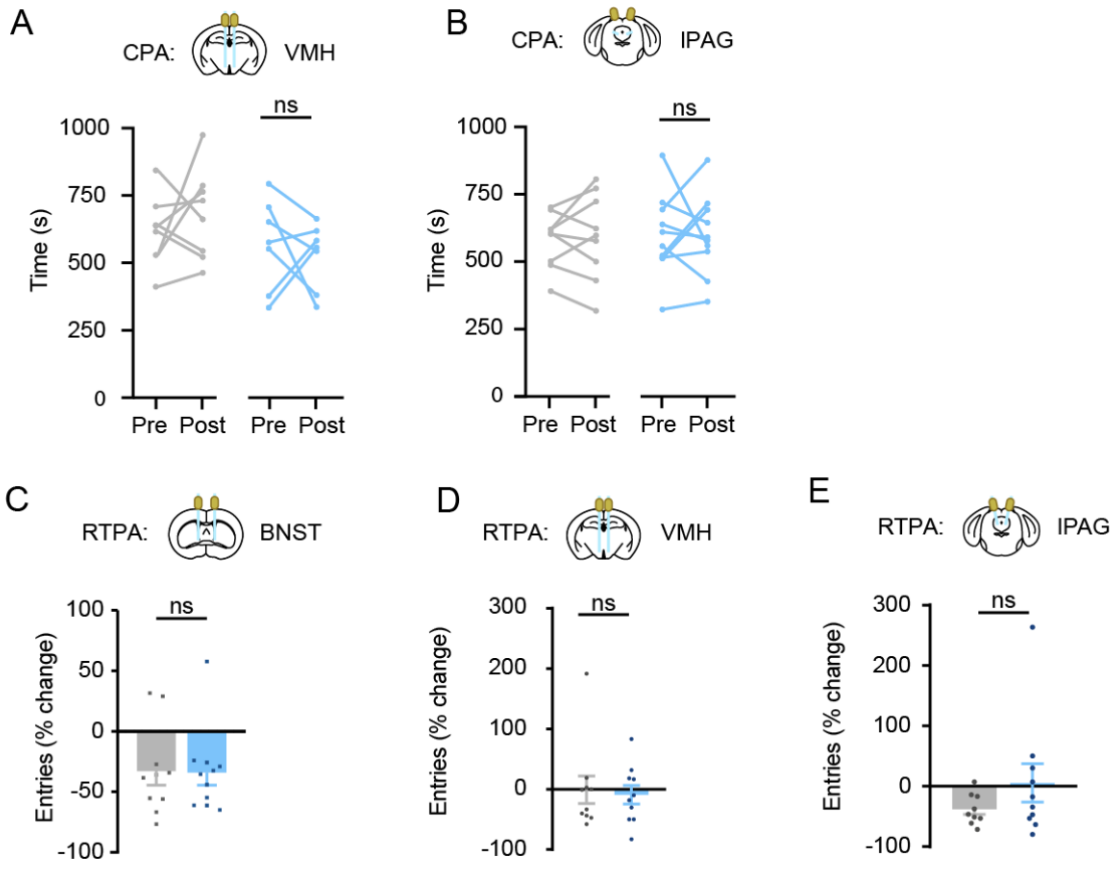

Figure 11 Optogenetic stimulation of lPBN efferents on aversive memory.

(A-B) Optogenetic activation of terminals in VMH (A) or lPAG (B) of ChR2-injected mice does not cause CPA (paired Student's t-test: VMH: p = 0.605; lPAG: p = 0.986). Data are from individual mice (n = 7 – 9 mice per condition).

(C-E) Optogenetic activation of ChR2-expressing efferents terminals in BNST (C), VMH (D), or lPAG (E) does not affect the number of entries into the photostimulation chamber during RTPA (Student's t-test, BNST: p = 0.942; VMH: p = 0.772; lPAG: p = 0.219). Data are mean ± SEM and dots represent data points from individual animals (n = 9 - 11 mice per group).

3.4 Discussion

In this chapter we devised experiments to determine the function encoded within divergent pathways emanating from the lPBN. Our optogenetic experimentation demonstrated drastically different effects on animal behavior. Projections to VMH and lPAG arise from dPBN, and the photoactivation of these projections resulted in behaviors that permit withdrawal or escape from a potentially noxious stimuli, as indicated by stimulus-locked increases in jumping, running, and/or endogenous analgesia. On the other hand, photostimulating elPBN axon terminals within BNST or CEA resulted in CPA learning. These data suggest that the cytoarchitecturally distinct domains of lPBN, although together respond to noxious stimuli, may mediate different aspects of nociceptive information to forebrain regions and consequently underlie behaviorally distinct aspects of the pain response.

An interesting finding is that, although lPBN comprises distinct subdomains, the photoactivation of any lPBN output resulted in real time place aversion. Whereas previous studies have focused on elPBN neurons, and particular those expressing CGRP, our data suggest that the lPBN serves as a hub to relay unpleasantness of either interoceptive or exteroceptive signals, at least in real time, through downstream forebrain regions. Notably, dPBN outputs failed to elicit aversive learning through CPA despite dramatic real time avoidance behavior. These indicate that the repeated photostimulation as our conditioning stimulus failed to recruit downstream mechanisms in either VMH or lPAG capable of driving learned behavior (Kunwar et al., 2015). On the other hand, repeated optogenetic activation of elPBN projections to BNST and CEA sufficiently developed an aversive memory. Although the specific mechanisms through which this occurs in BNST remain unclear (Davis et al., 2010; Lebow and Chen, 2016), this likely occurs through synaptic plasticity of CGRPR, somatostatin-expressing neurons, and other unidentified

genetic cell types in the CEA (Ciocchi et al., 2010; Han et al., 2015a; Li et al., 2013; Sato et al., 2015). Additional studies that identify the postsynaptic targets of these projections are warranted to better understand the mechanisms through which aversive learning occurs.

In contrast, little work has been done to elucidate the functional contributions of dPBN to nociception. Whereas previous studies of the physiological function of dPBN have revealed genetically-defined subsets involved in fluid satiation and thermoregulation (Nakamura and Morrison, 2008, 2010; Ryan et al., 2017), our findings demonstrate that the activity of dPBN outputs underlie robust locomotor behavior, suggesting the possibility that noxious stimuli may recruit these dPBN pathways to drive motivated behaviors to withdraw from potential injury. This is consistent with previous findings in which at least a subset of dPBN neurons preferentially respond to diverse noxious sensations, such as mechanical (in the form of a pinch) or thermal (burning heat) stimuli (Bernard et al., 1994; Bester et al., 1997; Hermanson and Blomqvist, 1996, 1997; Nakamura and Morrison, 2010). Interestingly, the optogenetic activation of dPBN terminals in VMH resulted in similar but disparate locomotor actions compared to that in lPAG despite prominent collateralizations to these two targets. This finding raises the possibility that, as is the case with elPBN collaterals to BNST and CEA, the evolutionary need to survive a life-threatening stimulus has developed redundant pathways to ensure an organism's survival. Alternatively, each collateral may relay nuanced aspects of the neural encoding of a threat such that the subtle differences in behaviors manifest from the coordinated activity of different downstream targets. Consistent with this idea, both VMH and lPAG have been shown to mediate different aspect of defensive behaviors such as running, jumping, and freezing (Kunwar et al., 2015; Tovote et al., 2016; Wang et al., 2015). Specific to terminal stimulation within lPAG, optogenetic activation resulted in increased endogenous analgesia likely through opioid-dependent mechanisms via the

rostroventral medulla and spinal cord (Basbaum and Fields, 1984; McGaraughty et al., 2004; Roeder et al., 2016).

A noteworthy observation is that the optogenetic activation of dPBN pathways elicited escape-like behaviors independent of a noxious stimulus, indicating that these behaviors reflect innate motor responses rather than the enhancement of a nocifensive response, as seen in other lPBN projections to brainstem (Barik et al., 2018). This suggests that a wide modality of stimuli capable of recruiting dPBN circuits may drive escape-like responses via the dPBN projections characterized in our experiments. This is not inconsistent with previous studies demonstrating that lPBN also serves significant roles in promoting arousal and inhibiting consummatory behaviors (Kaur et al., 2013; Kaur et al., 2017; Ryan et al., 2017), as an animal's ability to exhibit locomotor actions requires an increased state of arousal and reduction in feeding behavior. However, as a result of technical considerations we were unable to determine the role of divergent lPBN pathways on autonomic regulation of respiration and cardiovascular function in awake, behaving animals, a topic on which we speculate in our Conclusion.

Although our experiments provide evidence that dPBN and elPBN efferents primarily elicited distinct behavioral repertoires, we acknowledge that such a model undoubtedly oversimplifies the complex and interconnected circuitry underlying these behaviors. Despite optogenetic activation of axon terminals at a given downstream target, multiple brain regions from our manipulation are likely to have been indirectly affected. For example, both BNST and CEA exhibit reciprocal connections with each other as well as the lPBN and other brain regions (Barik et al., 2018; Rodriguez et al., 2017; Tokita et al., 2009). Consistent with this interconnectivity, we found that photostimulation of a single efferent pathway activates multiple brain regions, as evidenced by Fos induction. It is therefore not surprising that some behaviors were not completely

specific to the photoactivation of a particular lPBN projection. Most notably, stimulation of efferents to the BNST elicited small but significant escape-like responses, as measured by increases in running and endogenous analgesia, as well as CPA learning. Nevertheless, the broad findings of our experiments in this Chapter are consistent with a modular output from the lPBN that would enable the coordination of nocifensive responses in a context-dependent manner.

4.0 Role of dynorphin lateral parabrachial neurons in the pain experience

4.1 Introduction

The lPBN has been implicated in numerous autonomic regulatory roles such as arousal, respiration, cardiovascular responses, and feeding (Benarroch, 2016, 2018; Davern, 2014). However, the identity of lPBN neurons underlying these physiological functions has yet to be determined. The genetic identity of lPBN populations regulating thermosensation has been characterized in minor detail. dPBN neurons expressing dynorphin (*Pdyn*^{Cre}) respond more strongly to warmth, whereas cooling activates a subset of FoxP2-positive elPBN neurons (Geerling et al., 2016). Regardless, the convergence of both interoceptive and exteroceptive signals into lPBN likely engages lPBN circuits that integrate these signals to coordinate appropriate behavioral and autonomic responses.

To our knowledge, we are the first to perform experiments that investigated how the activation of *Pdyn*^{Cre} neurons affects nocifensive behavior. First, we designed experiments to identify anatomical connections between *Pdyn*^{Cre} neurons and spinoparabrachial neurons. We then performed optogenetic experiments to determine whether activation of these neurons were sufficient to elicit the nocifensive behaviors characterized in the previous Chapter. Finally, we selectively ablated these neurons in adult mice to determine the necessity of these neurons in nocifensive behaviors.

4.2 Methods

4.2.1 Animals

Mice were given free access to food and water and housed under standard laboratory conditions. The use of animals was approved by the Institutional Animal Care and Use Committee of the University of Pittsburgh. *Pdyn-IRES-Cre* (Krashes et al., 2014), *Sst-cre* ((Taniguchi et al., 2011) stock: 013044), *Calb2-cre* ((Taniguchi et al., 2011) stock: 010774), *Crh-cre* (Taniguchi et al., 2011) stock: 012704), and *Nts-cre* ((Leinninger et al., 2011) stock: 017525) were obtained from Jackson Laboratories.Wild-type C57BL/6 mice were obtained from Charles River (Cat # 027). For all experiments 8 – 16 week-old male and female mice were used. In all cases, no differences between male and female mice were observed and so the data were pooled.

4.2.2 Viruses

The following viruses were used for experimentation: AAV2-hsyn-eYFP (Addgene: 50465), AAV2-EF1a-DIO-eYFP (Addgene: 27056), AAV2-EF1a-DIO-hChR2(H134R)-eYFP (Addgene: 20298), AAV9-CAGGS-FLEX-ChR2-tdtomato.WRPE.SV40 (Addgene: 18917), AAV2-EF1a-flex-taCasp3-TEVp (Addgene: 45580), AAV8.2-hEF1a-DIO-synaptophysin-eYFP (MGH: AAV-RN2), AAV8.2-hEF1a-DIO-PSD95-eYFP (MGH: AAV-RN7), and AAV8.2-hEF1a-synaptophysin-mCherry (MGH: AAV-RN8). Viruses were purchased from University of North Carolina Vector Core, University of Pennsylvania Vector Core, and Massachusetts Gene Technology Core.

4.2.3 Stereotaxic injections and optical fiber implantation

Stereotaxic injections and optical fiber implantations were performed as described in the previous chapter. Mice were bilaterally injected with 0.5 μl virus. The injection needle was left in place for an additional 5- 10 min and then slowly withdrawn. Injections and optical fiber implantations were performed bilaterally in the lPBN at AP -5.11 mm, ML ± 1.25 mm, DV: -3.25. For implantation of optical fibers (Thor Labs: 1.25 mm ceramic ferrule 230 μm diameter), implants were slowly lowered 0.300-0.500 mm above the site of injection and secured to the skull with a thin layer of Vetbond (3M) and dental cement. The incision was closed using Vetbond and animals were given a subcutaneous injection of buprenorphine (0.3 mg/kg) and allowed to recover over a heat pad. Mice were given 4 weeks to recover prior to experimentation.

4.2.4 Intraspinal injections

Mice were anesthetized with 100 mg/kg ketamine and 10 mg/kg xylazine. An incision was made at the spinal cord level corresponding to L4-6 spinal level. The intrathecal space was exposed, and two injections of approximately 0.5 μl of virus was infused 300 μm below the surface of the spinal cord at 100 nL/min via glass pipette through the intrathecal space corresponding to L4-6 of the spinal cord. The glass pipette was left in place for an additional 5 minutes before withdrawal. The incision was closed with 5-0 vicryl suture. Buprenorphine was delivered post-surgery at 0.3 mg/kg subcutaneously, and mice were allowed to recover over a heat pad.

4.2.5 Immunohistochemistry

Immunohistochemistry was performed as previously described in Chapters 2 and 3. Primary antisera (rabbit anti-Homer1 at 1:1K) were incubated for 3 days at 4°C.

4.2.6 RNAscope in situ hybridization

Multiplex fluorescent in situ hybridization was performed according to the manufacturer's instructions (Advanced Cell Diagnostics #320850). Briefly, 18 μm-thick fresh-frozen sections containing the parabrachial nucleus were fixed in 4% paraformaldehyde, dehydrated, treated with protease for 15 minutes, and hybridized with gene-specific probes to mouse *Pdyn* (#318771), *Calca* (417961), *Tac1* (410351), *Gad2* (415071), *Fos* (316921), *Slc32a1* (#319191), and *Slc17a6* (#319171). DAPI (#320858) was used to visualize nuclei. 3-plex positive (#320881) and negative (#320871) control probes were tested. Two to three full-tissue z-stacked sections were quantified for a given mouse, and 2 – 4 mice were used per experiment.

4.2.7 Image acquisition and analysis

Full-tissue thickness sections were imaged using either an Olympus BX53 fluorescent microscope with UPlanSApo 4X, 10X, or 20X objectives or a Nikon A1R confocal microscope with 20X or 60X objectives. All images were quantified and analyzed using ImageJ. To quantify images in RNAscope in situ hybridization experiments, confocal images of tissue samples (1 – 2 sections per mouse over 2 – 4 mice) were imaged and only cells whose nuclei were clearly visible by DAPI staining and exhibited fluorescent signal were counted.

4.2.8 Behavior

Behavior was performed as previously described in Chapter 3.

Diffuse noxious inhibitory control (DNIC) testing

To induce DNIC, 0.1% 10 μl capsaicin solution was administered into the hindpaw, and mice were subsequently tested for tail flick latency 20 minutes post-injection at 55°C as described during the tail immersion test.

4.2.9 Statistical analysis

Statistical analysis was performed as previously described in Chapter 3.

4.3 Results

Having examined the outputs from the lPBN that could mediate the behavioral responses to noxious stimuli, we next characterized the nociceptive inputs to this nucleus. Towards this end, we used the *Tacr1*^{CreER} allele (Huang et al., 2016) to visualize neurokinin 1 receptor-expressing spinoparabrachial neurons (NK1R+ SPbN), which are known to transmit noxious signals from the spinal cord to the brain (Cameron et al., 2015; Todd, 2010). To visualize the innervation of the lPBN by these neurons, an AAV encoding a Cre dependent fluorescent reporter was injected into the L4-L6 spinal cord region of *Tacr1*^{CreER} tamoxifen-inducible Cre mice (Figure 12A). We found that *Tacr1*^{CreER} neurons showed dense innervation of the lPBN that was regionally constrained, with the vast majority of these terminals targeting the dPBN and very few targeting the elPBN

(Figure 12B and 12C), consistent with previous studies (Harrison et al., 2004). To ensure that this observation was not specific to *Tacr1*^{CreER} neurons, we repeated this experiment using a constitutive AAV to label all spinoparabrachial neurons. Again, we saw the same distribution of input from the spinal cord, which was predominant in the dPBN, but not the elPBN (Figures 12D and 12E).

The paucity of direct nociceptive input to the elPBN was somewhat curious to us in light of previous studies that showed direct innervation of elPBN neurons by spinoparabrachial neurons (Cechetto et al., 1985; Feil and Herbert, 1995; Ma and Peschanski, 1988). Indeed, we found that both the dPBN and elPBN subregions showed significant Fos induction in response to noxious stimulation induced via capsaicin treatment of the hindpaw (Figures 12F and 12G), consistent with previous results (Bernard et al., 1994; Hermanson and Blomqvist, 1996). However, the presynaptic terminals of *Tacr1*^{CreER} spinoparabrachial neurons were only observed in close apposition to Fos+ neurons within the dPBN (Figure 12H).

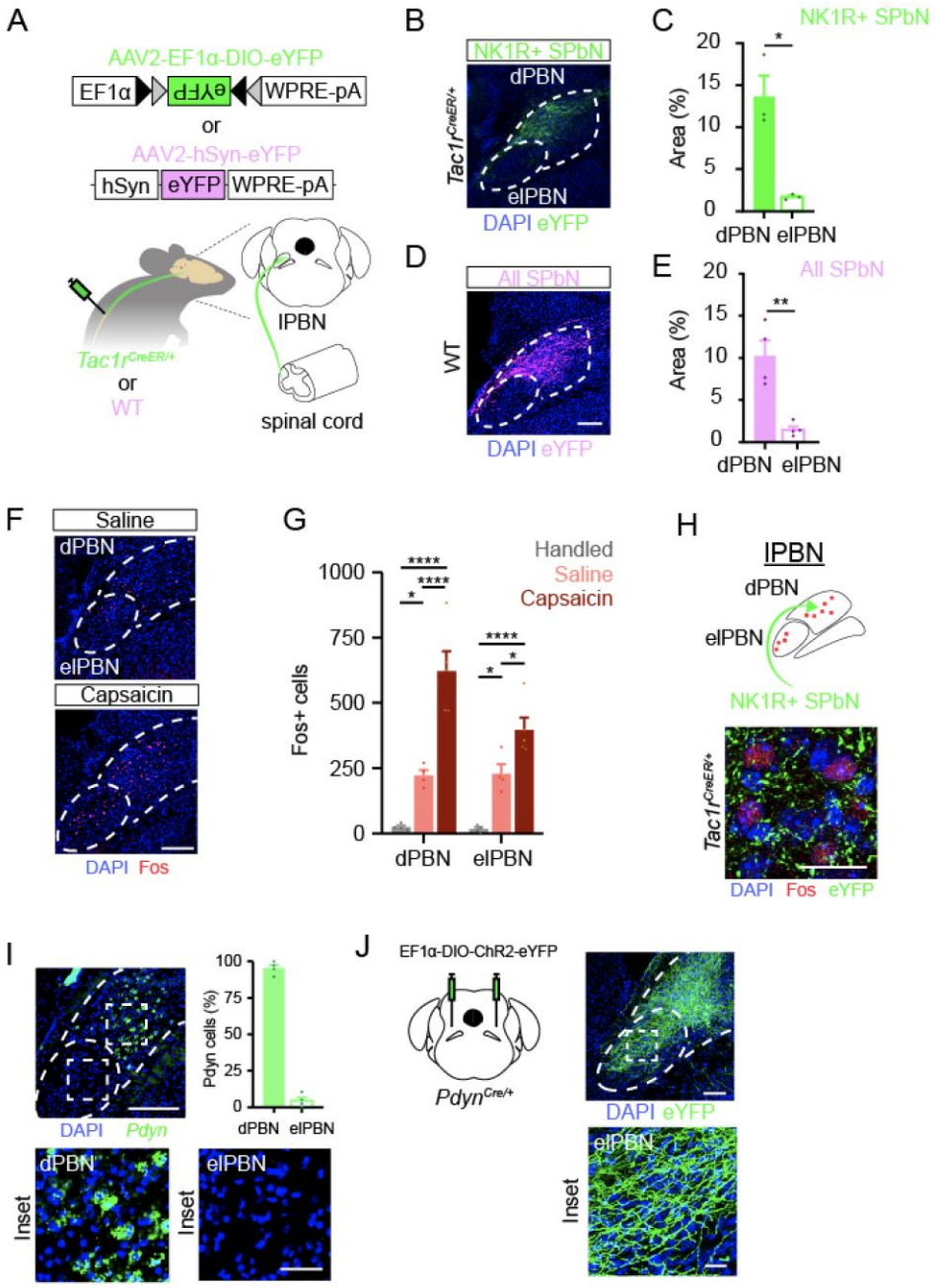

Figure 12 Spinoparabrachial input is concentrated in dPBN, but noxious stimulation drives Fos expression in both dPBN and elPBN.

(A) Experimental strategy to visualize spinal inputs into lPBN. An AAV encoding Cre- dependent eYFP (green) or constitutive eYFP (pseudocolored pink) was injected into the spinal cord (L4-L6) in *Tacr1*^{CreER} or WT mice.

(B-C) Representative image (B) and quantification (C) of the innervation density of efferent terminals in the lPBN from NK1R+ spinoparabrachial neurons (SPbN). Data are mean ± SEM and dots represent data points from individual animals (n = 3 mice). * indicates area of SPbN projections to dPBN (as percent of region) is significantly greater than that to elPBN (Paired Student's t-test; p = 0.036). Scale bar = 100 μm.
(D-E) Representative image (D) and quantification (E) of the innervation density of efferent terminals in the lPBN from all spinoparabrachial neurons. Data are mean ± SEM and dots represent data points from individual animals (n = 4 mice). * indicates area of spinoparabrachial projections to dPBN (as percent of region) is significantly greater than that to elPBN (Paired Student's t-test; p = 0.0094). Scale bar = 100 μm.
(F-G) Representative image (F) and quantification (G) of Fos induction in the dPBN and elPBN in response to intraplantar saline (10 μl) or capsaicin (10 μl, 0.03%). Data are mean ± SEM and dots represent data points from individual animals (n = 4 - 5 mice per group). Asterisks indicate significantly different (Two-way RM ANOVA followed by Tukey's post-hoc; * $p < 0.05$; **** $p < 0.001$.) Scale bar = 100 μm.
(H) NK1R+ spinoparabrachial terminals (visualized through viral expression of eYFP) are found in close apposition to Fos+ cells in the dPBN following intraplantar capsaicin. Image is representative of data from 4 mice. Scale bar = 25 μm.
(I) Representative image and quantification of $Pdyn^{Cre}$ expressing neurons in the dPBN and elPBN as visualized by FISH (n = 4 mice). Scale bar = 100 μm; inset: 25 μm.
(J) $Pdyn^{Cre}$ neurons in dPBN project to elPBN. AAV encoding Cre-dependent ChR2 was injected into lPBN of $Pdyn^{Cre}$ mice to visualize projection. Images are representative of data from at least 4 mice. Scale bar = 100 μm; inset: 25 μm.

The apparent discrepancy between the localized nature of the nociceptive input in the dPBN and the widespread nature of the Fos induction by intraplantar capsaicin raised the question of how noxious information reaches the elPBN. With the goal of identifying a neuronal population that might convey nociceptive information between lPBN subregions, we investigated cell types that are known to be expressed in the dPBN using a combination of Cre alleles and stereotaxic

injection of Cre dependent AAV reporters to visualize these cells and their projections. In total, six alleles were screened: *Sst*^{Cre}; *Tacr1*^{CreER}, *Nts*^{Cre}, *Calb2*^{Cre}, *Crh*^{Cre} and *Pdyn*^{Cre} alleles. Although all of these genetic tools uncovered populations of neurons with subregion-specific expression in the lPBN (Figure 13), only dynorphin-expressing neurons exhibited unique anatomical characteristics that positioned them to convey noxious information from the dPBN to the elPBN. In particular, using dual fluorescent in situ hybridization (FISH), we found *Pdyn* neurons were located almost exclusively in the dorsal region of the lPBN (Figure 12I), consistent with previous studies (Geerling et al., 2016). Next, we validated the *Pdyn*^{Cre} allele, confirming that Cre-dependent AAV viruses injected into the lPBN of these mice selectively targeted *Pdyn*-expressing

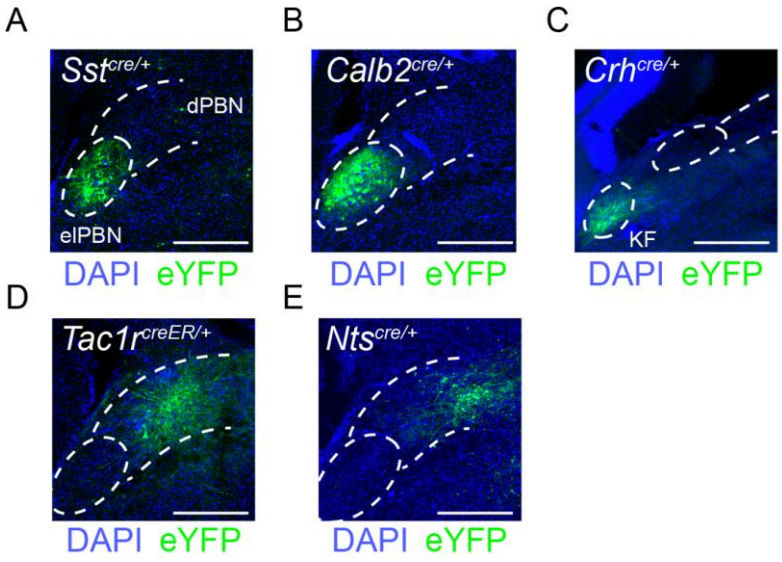

Figure 13 Screen of putative cell-type specific lPBN subpopulations

AAV encoding a fluorescently-tagged channelrhodopsin (0.5µl, bilateral) was injected into the lPBN of the following genetic mice harboring knock-in alleles for Cre-recombinase: (A) Somatostatin (*Sst-cre*, Taniguchi et al. 2011). (B) Calretinin (*Calb2-cre*, Taniguchi et al. 2011). (C) Corticotropin releasing hormone (*Crh-cre*, Taniguchi et al. 2011). (D) Neurokinin-1 receptor (*Tacr1-creER*, Huang et al. 2016). (E) Neurotensin (*Nts-cre*, Leinninger et al. 2011). Scale bar = 200 µm (A - E).

neurons (Figure 15A). Finally, using this allele to visualize dynorphin-expressing neurons, we found that dynorphin neurons in dPBN project to the elPBN (Figure 12J). Thus, dynorphin-expressing neurons have cell bodies in the dPBN and send prominent projections to the elPBN.

To further investigate the putative role of dynorphin neurons in nociceptive processing, we used a viral strategy to determine whether spinoparabrachial neurons directly innervate the *Pdyn*^{Cre} subset of dPBN neurons. *Pdyn*^{Cre} mice were stereotaxically injected with AAV encoding a Cre-dependent PSD95-eYFP into the lPBN and another encoding a constitutive synaptophysin-tdtomato into the spinal cord (Figure 14A). These efforts revealed presynaptic terminals from spinal output neurons that were in close apposition to PSD95-eYFP in *Pdyn*^{Cre} neurons, suggestive of direct synaptic contacts. Moreover, we found that intraplantar injection of capsaicin gave rise to strong Fos induction in *Pdyn*^{Cre} neurons. Specifically, 75% of Fos-expressing cells belonged to the *Pdyn*^{Cre} population and Fos was induced in 50% of these cells (Figure 14B). Together, these data provide anatomical and functional evidence that *Pdyn*^{Cre} neurons in the dPBN receive noxious input via spinoparabrachial neurons.

To characterize these *Pdyn*^{Cre} neurons in more detail, we next examined whether this population represented an excitatory or inhibitory population of neurons through dual fluorescent in situ hybridization (FISH). We found that nearly all *Pdyn* transcript colocalized with *Slc17a6 (Vglut2),* with *Pdyn* cells representing approximately one-quarter of the excitatory population within the dPBN (Figure 14C). In contrast, there was very little to no overlap of *Pdyn* and the inhibitory marker *Slc32a1 (Vgat)* (Figure 15B). Thus, from a neurochemical standpoint, dynorphin neurons in the dPBN are positioned to relay nociceptive information to the elPBN.

To further investigate whether dynorphin neurons could provide a cellular substrate for transmission of nociceptive information to elPBN efferents, we used viral and retrograde tracing

approaches to determine whether *Pdyn*^{Cre} neurons form anatomical connections with elPBN neurons that project to CEA and BNST. Towards this end, we stereotaxically injected AAV encoding a Cre-dependent synaptophysin-eYFP into dPBN together with CTB into either the CEA or BNST of *Pdyn*^{Cre} mice (Figure 14D). These experiments suggested that approximately two-thirds of CTB-labeled cells from either the BNST or the CEA receive synaptic input from *Pdyn*^{Cre} neurons as supported by the close apposition of retrogradely labeled cells to synaptophysin-eYFP and the post-synaptic density marker Homer1 (Figures 14E and 14F). These data provide anatomical support for the idea that *Pdyn*^{Cre} neurons may convey noxious information to neurons in the elPBN that have efferent projections to the CEA and/or BNST.

To further test the idea that *Pdyn*^{Cre} neurons in the dPBN convey information to the elPBN, we next examined whether activation of this population is sufficient to elicit the behavioral responses that are mediated by elPBN efferents. To manipulate these cells, we delivered an AAV encoding Cre-dependent ChR2 or eYFP into the lPBN of *Pdyn*^{Cre} mice. Consistent with our hypothesis, we found that photostimulation of *Pdyn*^{Cre} neurons in the lPBN mice gave rise to aversive behaviors, but not escape behaviors. In particular, optogenetic stimulation resulted in real time place aversion coupled with a significant reduction in number of entries into the stimulation chamber (Figures 14G and 14H). In contrast, the activation of *Pdyn*^{Cre} neurons had no effect on escape behaviors including running, jumping or tail flick latency (Figures 15C, 15D and 15E). The optogenetic activation of *Pdyn*^{Cre} neurons in lPBN provide behavioral data to support the idea that these neurons convey noxious information to elPBN neurons that project to downstream forebrain areas. To confirm our behavioral observations, we stereotaxically delivered virus encoding a genetically engineered caspase 3, a protease that induces programmed cell death

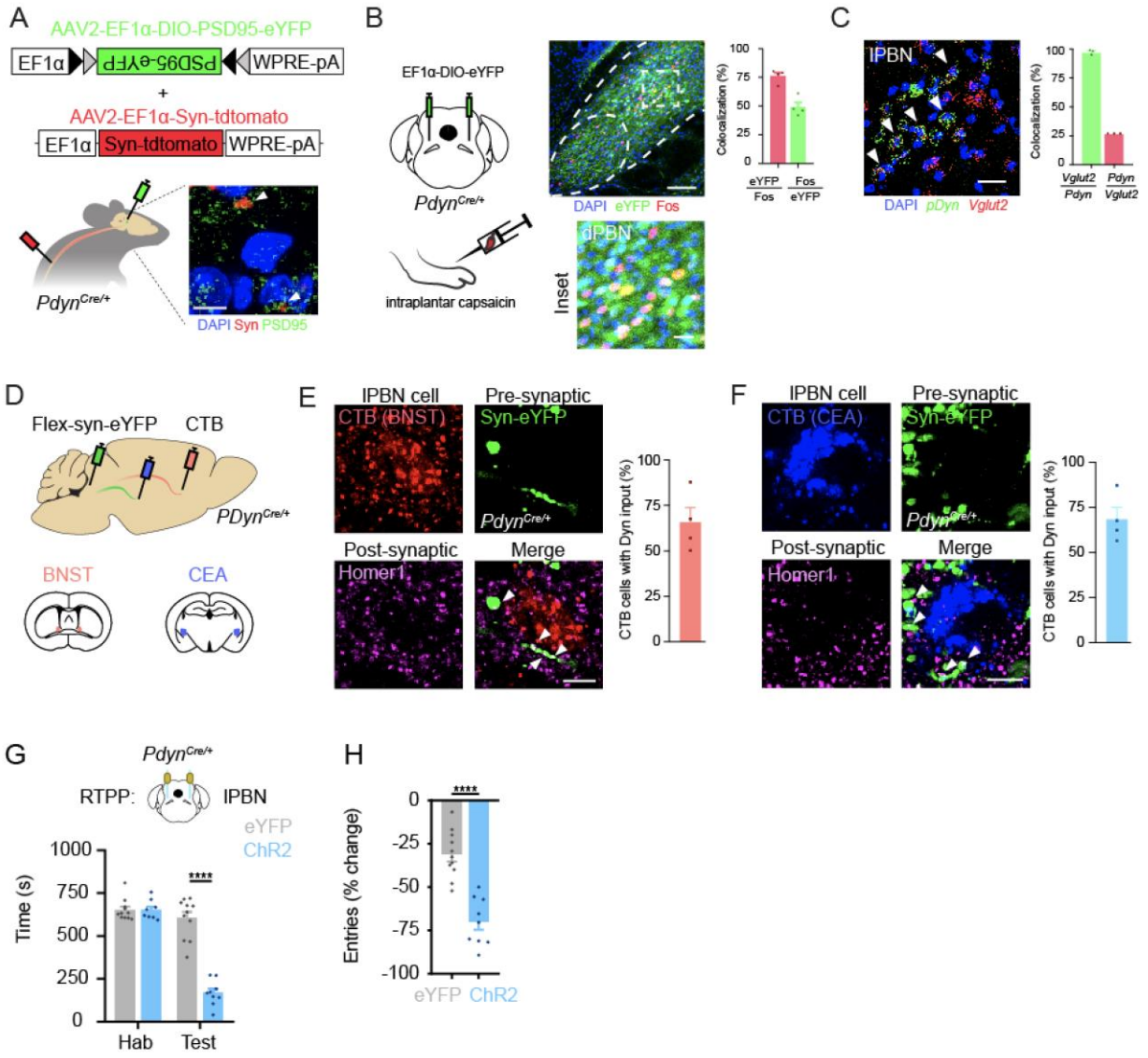

Figure 14 Dynorphin-expressing neurons may convey nociceptive input from dPBN to elPBN

(A) Spinoparabrachial synaptic inputs are found in close apposition to postsynaptic terminals of dynorphin neurons in dPBN. *Pdyn*^{Cre} mice were injected with AAVs encoding a Cre-dependent PSD95-eYFP in the lPBN and constitutive synaptophysin-tdtomato in the spinal cord (L4-L6). Image is representative of data from 2 mice.

(B) *Pdyn*^{Cre} cells express Fos following in response to noxious stimulation. An AAV encoding Cre-dependent eYFP was stereotactically injected into the lPBN to visualize dynorphin+ cells. Mice received intraplantar injections of capsaicin (10 µl, 0.03%). Representative image and quantification of the colocalization of *Fos*+ neurons and *Pdyn*^{Cre} neurons, as visualized by expression of eYFP. Data are mean ± SEM and dots represent data points from individual animals (n = 4 mice). Scale bar = 25 µm; inset: 5 µm.

(C) Dynorphin cells are primarily excitatory. Representative image and quantification of colocalization between *Pdyn*^{Cre} and *Slc17a6* mRNA in dPBN, as observed by dual FISH. Data are mean ± SEM and dots represent data points from individual animals (n = 3 mice). Arrows denote neurons with colocalized signal. Scale bar = 25 μm.

(D) Experimental strategy to visualize *Pdyn*^{Cre} synaptic inputs onto elPBN efferents that project to BNST or CEA. CTB was injected into either the BNST or the CEA and Cre-dependent synaptophysin-eYFP was delivered into the lPBN of *Pdyn*^{Cre} mice.

(E-F). Synaptic terminals from *Pdyn*^{Cre} neurons (green) are in close apposition to Homer1 puncta (purple) surrounding CTB-labeled neurons that have been backlabeled from the BNST (E; red) or CEA (F; blue). Data are mean ± SEM and dots represent data points from individual animals (n = 4 mice per experiment).

(G) Photostimulation of ChR2-expressing *Pdyn*^{Cre} cells in the dPBN elicits real time place aversion. Data are mean ± SEM and dots represent data points from individual animals (n = 9 – 11 mice per group). **** indicates significantly different (Two-way RM ANOVA followed by Holm-Sidak post-hoc test, $p < 0.0001$).

(H) Photostimulation of ChR2-expressing *Pdyn*^{Cre} cells in the dPBN significantly diminished entry number into the stimulation chamber. Data are mean ± SEM and dots represent data points from individual animals (n = 9 – 11 mice per group). **** indicates significantly different (unpaired Student's t-test $p < 0.0001$).

(Yang et al., 2013). Through this approach, we ablated the adult population of *Pdyn*^{Cre} neurons in lPBN and subsequently tested whether the loss of these neurons prevented mice from developing an aversive memory to a painful stimulus. Caspase-injected mice exhibited dramatically fewer *Pdyn*^{Cre} neurons compared to eYFP-injected mice (Figure 16A and 16B). To determine whether ablating this specific lPBN subpopulation would block the development of an aversive memory, we tested mice in a CPA assay in which mice were conditioned to intraplantar injection of formalin. Before conditioning, both control and caspase-injected mice spent similar amounts of time in the conditioned chamber. However, following two consecutive days of formalin conditioning, only control mice exhibited a significance reduction in the time spent in the

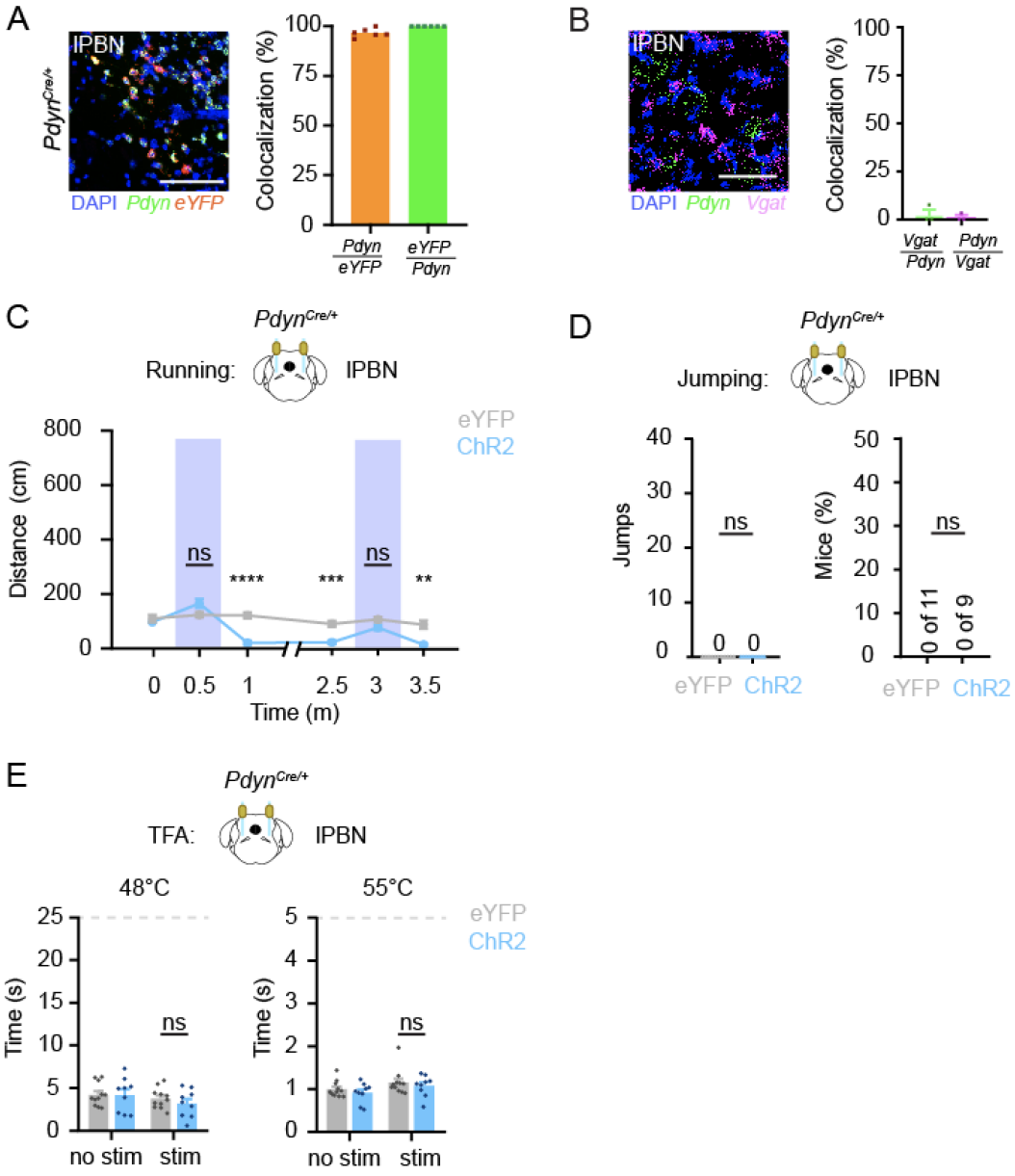

Figure 15 Analysis of Pdyn neurons in the lPBN and the effects of optogenetic activation.

(A) Representative image (left) and quantification (right) of lPBN in *Pdyn*^{Cre} mice injected with an AAV encoding Cre-dependent eYFP into the lPBN and subsequently analyzed by dual FISH using probes targeting *Pdyn* and eYFP. Data are mean and dots represent data points from individual animals (n = 2 mice).

(B) Representative image (left) and quantification (right) of the lPBN using dual FISH with probes targeting *Pdyn* and *Vgat*. Data are mean and dots represent data points from individual animals (n = 3 mice).

(C) Optogenetic stimulation of ChR2-expressing *Pdyn*^{Cre} neurons in lPBN does not induce lateral locomotion (two-way RM ANOVA followed by Holm-Sidak post-hoc test, F (5, 90) = 17.21).

(D) *Pdyn*^{Cre} ChR2-injected mice do not jump when photostimulated.

(E) Optogenetic stimulation of ChR2-expressing *Pdyn*^{Cre} neurons in lPBN does not increase tail flick latency at 48°C (two-way RM ANOVA, F (1, 18) = 0.6300) or 55°C (two-way RM ANOVA, F (1, 18) = 0.004203) compared to control mice. Data represent mean ± SEM. Scale bar = 50 μm (A - B)

conditioned chamber (Figure 16C). These data suggest that the loss of *Pdyn*^{Cre} neurons prevents CPA learning.

Next, we tested whether the loss of *Pdyn*^{Cre} neurons specifically precluded the ability to develop an aversive memory and not other behavioral outputs related to escape behaviors. To address this, we injected a capsaicin solution into the hindpaw of control and caspase-injected mice to determine whether *Pdyn*^{Cre} neurons mediate diffuse noxious inhibitory control (DNIC), a form of descending modulation that is mediated in part through lPAG projections to brainstem (Le Bars, 2002; Ossipov et al., 2010). Both control and caspase-injected mice exhibited no differences in their tail flick latencies at either baseline or following capsaicin injection (Figure 16D). Importantly, both groups exhibited an increase in their tail flick latencies following capsaicin injection, indicating the recruitment of DNIC in response to hindpaw capsaicin administration (51.3 ± 12.6% vs. 70.1 ± 12.6%, control vs. caspase-treated mice, respectively). Thus, these mice exhibited an intact DNIC response despite the ablation of *Pdyn*^{Cre} neurons within lPBN.

The observation that caspase-treated *Pdyn*^{Cre} mice exhibited impaired CPA learning but not a DNIC response to a noxious stimulus suggests that *Pdyn*^{Cre} neurons may indeed be conveying noxious input from dPBN to neurons within elPBN, consistent with our anatomical data (Figure 14E and 14F). To further test this, we determined whether delivering intraplantar capsaicin in

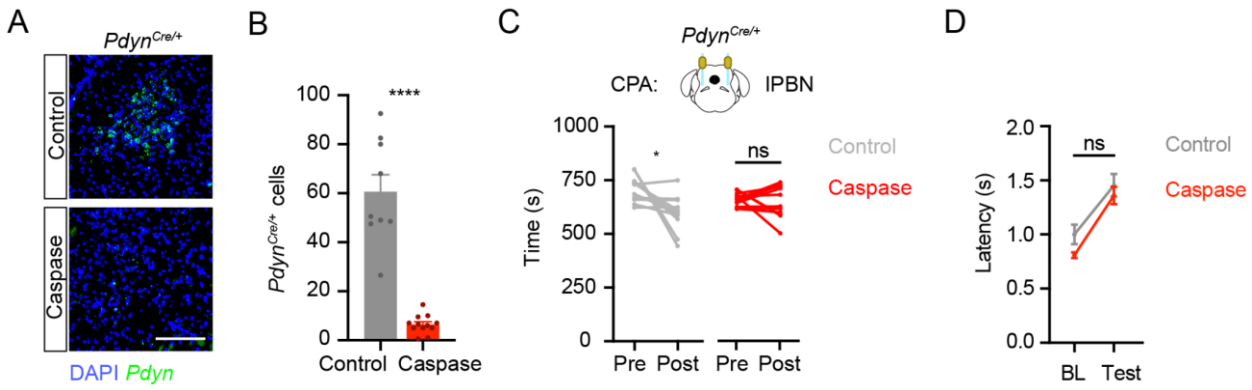

Figure 16 Ablating *Pdyn*+ lPBN neurons abrogates CPA but not DNIC.

(A) Visualization of *Pdyn*+ lPBN neurons in control and caspase-injected mice. (B) Caspase-injected mice exhibited significantly fewer $Pdyn^{Cre}$ neurons compared to control mice. Data are mean ± SEM and dots represent data points from individual animals (unpaired Student's t test, $p < 0.0001$, n = 9 – 12 mice per group). (C) Ablating $Pdyn^{Cre}$ neurons prevents CPA compared to control mice (paired Student's t test, Control: $p = 0.016$, n = 11 – 12 mice per group). (D) The withdrawal latency during capsaicin-induced DNIC to a tail flick test was not significantly different compared to that in control mice. (two-way RM ANOVA, $F(1, 16) = 0.551$, n = 8 – 10 mice per group).

control and caspase-treated $Pdyn^{Cre}$ mice would recruit neurons within elPBN through the induction of Fos. Recent studies have demonstrated the significance of CGRP- and Tac1-expressing elPBN neurons on pain-related behaviors (Barik et al., 2018; Campos et al., 2018). We therefore focused on Fos expression within these two elPBN subsets. In control mice, intraplantar capsaicin administration induced *Fos* in 16.3 ± 1.8% of *Calca*-positive neurons (Figure 17A and 17B). However, this proportion was significantly reduced in mice in which $Pdyn^{Cre}$ were ablated (10.3 ± 1.9%, $p = 0.04$, n = 5 – 7 mice per group). We observed no difference in the proportion of *Tac1* elPBN neurons expressing Fos in control and $Pdyn^{Cre}$ - ablated mice (Figure 17C and 17D). These data highlight that $Pdyn^{Cre}$ neurons serve a crucial link for the recruitment of elPBN pathways to CEA and BNST (Figure 18).

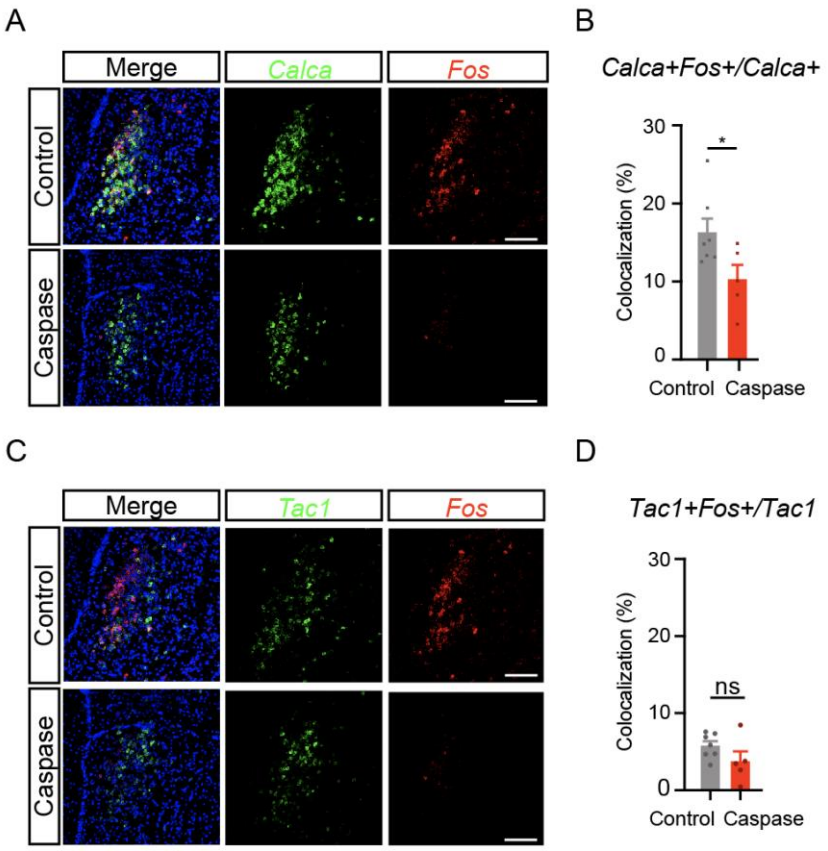

Figure 17 Effect of ablating dynorphin-expressing neurons on Fos expression in elPBN subpopulations.

(A) Representative images of Fos expression in *Calca* elPBN subpopulations between control vs. caspase-injected mice.

(B) Ablation of *Pdyn*^{Cre} neurons in dPBN reduces the number of Fos expressing-*Calca* neurons in elPBN following intraplantar injection of capsaicin. (unpaired Student's t-test, p = 0.044, n = 5 – 7 mice).

(C) Representative images of Fos expression in *Tac1* elPBN subpopulations between control vs. caspase-injected mice.

(D) Ablation of *Pdyn*^{Cre} neurons in dPBN does not reduce the number of Fos-expressing *Tac1* neurons in elPBN following intraplantar injection of capsaicin. (unpaired Student's t-test, p = 0.154, n = 5 – 7 mice).

4.4 Discussion

In this final Chapter, we present data supporting the idea that dynorphin-expressing neurons within dPBN relay noxious input arising from the periphery onto elPBN-projecting neurons, thus coordinating the generation of a nocifensive response at the level of the lPBN. Noxious stimuli induce Fos expression in both dPBN and elPBN. However, only dPBN Fos+ neurons are in close apposition to NK1R+ spinoparabrachial neurons. We demonstrate that the majority of Fos expression occurs within the *Pdyn*^{Cre} subset, and that these neurons extend processes directly onto BNST- and CEA- projecting neurons within elPBN. Despite their cell bodies being located within dPBN, optogenetic activation of dynorphin-positive neurons elicits an aversive memory with no effect on escape-like behaviors such as increased running, jumping, or recruitment of endogenous analgesia. Complementary results through the ablation of this genetically-defined population show that loss of these neurons impairs CPA learning. Furthermore, elPBN CGRP- and Tac1-expressing neurons of mice lacking dPBN dynorphin neurons exhibit diminutions in Fos expression in response to noxious stimulation as revealed by FISH analysis, supporting the role of dynorphin neurons in communicating across lPBN territories.

Spinoparabrachial neurons expressing the NK1R have been reported to terminate in the lPBN (Cameron et al., 2015; Cechetto et al., 1985; Harrison et al., 2004; Hylden et al., 1989; McMahon and Wall, 1985; Panneton and Burton, 1985). However, the neural population receiving these nociceptive inputs remain unclear. It is likely that the neurons receiving this direct input compose a heterogeneous group that underlie different autonomic and behavioral responses. The *Pdyn*^{Cre} and *Tacr1*^{CreER} populations that we visualized in our tracing studies consist of spatially separate populations that reside within the terminal fields of NK1R+ spinoparabrachial neurons. Furthermore, the dendritic and axonal extensions as well as projection patterns to downstream

brain regions appear vastly different between *Pdyn*^{Cre} and *Tacr1*^{CreER} neurons, arguing that these genetically defined populations represent discrete dPBN subpopulations. Further characterizations of the degree of overlap are warranted to confirm this. In addition, we suggest that the *Pdyn*^{Cre} population receive direct input from NK1R-positive spinoparabrachial neurons. However, it is unlikely to be the only subpopulation that receives this monosynaptic input. *Tacr1*^{CreER} neurons are within the terminal fields of these spinoparabrachial neurons, but whether these populations receive direct input from the spinal cord remains debatable. Thus, electrophysiology recordings are needed to confirm functional synapses between spinoparabrachial neurons expressing NK1R and their downstream targets, such as the *Pdyn*^{Cre} and/or *Tacr1*^{CreER} populations. A recent study demonstrated that a subset of spinoparabrachial neurons form monosynaptic connections with dPBN but not elPBN neurons (Huang et al., 2018). Thus, it is possible that these neurons make up a part of the *Pdyn*^{Cre} or *Tacr1*^{CreER} subsets.

Moreover, the morphology of the *Pdyn*^{Cre} and *Tacr1*^{CreER} populations appear to span cytoarchitectural boundaries, suggesting the possibility that these neurons may engage in trans-domain communication to convey noxious information among adjacent subnuclei, for example to neurons within the elPBN such as those expressing CGRP (Bourgeais et al., 2001; Hayward and Felder, 1999; Herbert and Bellintani-Guardia, 1995). Consistent with this anatomy, our data reveal that only the *Pdyn*^{Cre} neurons have cell bodies in the dPBN and send extensive projections to the elPBN. This does not preclude the possibility that elPBN neurons extend dendritic arbors dorsally into dPBN subdivisions (Bourgeais et al., 2003; Chamberlin et al., 1999). However, the dendritic domains of most elPBN neurons were found to remain cytoarchitecturally confined to the elPBN, and the relationship between those that exhibit dendritic arbors within dPBN and their response to noxious stimuli remain unclear. In addition, we find that *Pdyn*^{Cre} neurons are activated by noxious

input and drive aversion, but not escape behaviors. However, we note that this is unlikely to be the only function of *Pdyn*^{Cre} cells in the lPBN because these neurons have been shown to play important roles in temperature homeostasis (Geerling et al., 2016; Nakamura and Morrison, 2008, 2010). These findings raise the possibility that *Pdyn*^{Cre} neurons in the lPBN are not a single, homogeneous population. Indeed, we observed prominent projections to downstream targets including the dorsomedial hypothalamus (DMH) and lPAG. As we previously found that dPBN neurons collateralize to VMH and lPAG, we believe that the *Pdyn*^{Cre} population does not compose those that collateralize to these two targets. Furthermore, optogenetic stimulation of dPBN *Pdyn*^{Cre} terminals in lPAG or DMH failed to elicit running, jumping, or descending modulation (data not shown), suggesting that the observed behaviors following optogenetic stimulation of *Pdyn*^{Cre} lPBN neurons arose through the circuit manipulation of local lPBN activity, namely those between dPBN and elPBN neurons. In future studies, it will be important to characterize this heterogeneity in more detail to identify bona fide cell types and characterize how each defined population responds to diverse stimuli. For example, determining the sufficiency and requirement of *Pdyn*^{Cre} lPBN neurons and their projections to DMH or lPAG in a variety of thermal challenges, such as a thermal place preference assay, would help delineate this population in greater detail.

A noteworthy finding through our optogenetic activation of *Pdyn*^{Cre} neurons is the reduction in locomotor activity following photostimulation. A previous study showed that activating CGRP-expressing neurons in elPBN resulted in reversibly induced freezing with increases in basal immobility; stimulating downstream CEA neurons expressing the CGRP receptor (CGRPR) resulted in gradually increasing freezing behavior over several minutes (Han_Palmiter_2015). Thus, one possible explanation for the freezing behavior observed following *Pdyn*^{Cre} stimulation is the recruitment of the CGRP lPBN projections to CGRPR CEA.

Consistent with this interpretation, ablating *Pdyn*^{Cre} neurons reduces Fos expression in CGRP lPBN neurons following exposure to a noxious stimulus. However, we would have expected to observe freezing behavior following terminal activation of elPBN projections to CEA. The CEA comprises heterogeneous populations underlying divergent behavioral repertoires (Kim et al., 2017). Our terminal stimulation may therefore have targeted several of these populations which resulted in no overt freezing behavior. Future experiments would help elucidate the different postsynaptic targets of *Pdyn*^{Cre} neurons, the heterogeneity of cell types within lPBN, and their interactions that underlie the nociceptive response.

5.0 Conclusion

This study investigated the neural pathways of lPBN neurons emanating from spatially discrete regions that target different downstream regions and encode different components of a nocifensive response. We used genetic approaches to visualize and characterize these pathways. Furthermore, we manipulated the activity of these divergent projections using optogenetic and chemogenetic approaches. Our visualization of lPBN populations revealed a unique subset of lPBN neurons that spanned cytoarchitectural boundaries and mediated sensory input from spinal cord to forebrain-projecting elPBN neurons to elicit aversive learning. Our experiments provide a framework for future studies to better understand more broadly how different lPBN populations contribute to physiological responses to potentially threatening stimuli.

Our first step in this collection of experiments demonstrated the significance of lPBN activity to exhibit a nocifensive response to mechanical hypersensitivity. Next, we characterized the efferent pathways from two distinct lPBN populations: those arising from dPBN collateralize to VMH and lPAG, whereas elPBN collateralize to BNST and CEA. This unique feature of lPBN anatomy led us to functionally characterize these projections. Using optogenetic approaches, we found that VMH- and lPAG-projecting neurons elicited motor sequence reflective of escape-like behaviors. Furthermore, we found that lPAG terminal stimulation induces endogenous analgesia, likely through descending pathways onto brainstem nuclei and spinal cord. On the other hand, the activation of collaterals to BNST and CEA resulted in the formation of aversive memories. We wondered how noxious stimulation recruits these different anatomically distinct subdivisions and found that a subset of dPBN neurons expressing dynorphin may communicate noxious input between different lPBN subregions. Optogenetic activation of $Pdyn^{Cre}$ promoted aversive learning

but not escape-like behaviors as observed from terminal stimulations in VMH or lPAG. Moreover, genetically ablating *Pdyn*^{Cre} neurons blocked this effect, demonstrating their critical role in the formation of an aversive memory. In summary, our data support the conclusion that collateralizing pathways from the lPBN underlie behaviorally distinct aspects of a pain response (Figure 18).

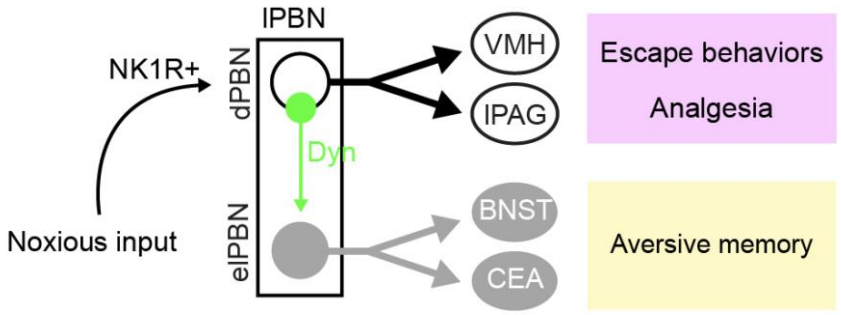

Figure 18 Model of divergent lPBN circuits

Model: Noxious input is conveyed primarily to the dPBN. Efferents from the dPBN collateralize to VMH and lPAG and mediate behavioral responses that enable escape. Dynorphin neurons in the dPBN convey noxious information to elPBN. Efferents from the elPBN collateralize onto the CEA and BNST and mediate aversion and avoidance memory.

5.1 Limitations of genetic strategies to characterize and manipulate neural activity

Despite our approach to characterize the anatomical and functional outputs of lPBN in richer detail, we realized several shortcomings that need to be factored in when we interpret our data. As with all genetic approaches to manipulate neuronal activity, we understand that our optogenetic activation of lPBN populations and their outputs do not reflect physiological activity of these pathways. Rather, our approach revealed possible behavioral actions these neurons can

initiate, as the neural coding of interoceptive or exteroceptive signals rarely if ever recruit homogeneous neuronal populations that fire synchronously during normal physiological states. Furthermore, our genetic strategy to ablate a subset of lPBN neurons expressing dynorphin may have resulted in plastic changes and neuronal rewiring. Thus, the behavioral responses observed may not necessarily reflect the requirement of the ablated neurons. Nevertheless, these modern genetic tools provide great advantages to traditional approaches to activate neural populations, such as electrical stimulation, or pharmacological/chemical ablation. For example, optogenetics and ablation via a genetically-encoded caspase allow for targeted specificity to a particular subset of neurons within a heterogeneous population, thereby avoiding off-target effects and passing fibers or neighboring neurons.

An important detail in our optogenetic approach is that all projections were photoactivated using the same paradigm – 20 Hz stimulation at a maximal laser power of 10 mW. Using the same protocol may help simplify the interpretation of our behavioral data. However, it brings into question whether the downstream targets were activated using "ideal" stimulation paradigms. For example, VMH neurons downstream of lPBN may respond differently than those downstream in CEA (Han et al., 2015a; Wang et al., 2015). Nevertheless, the interrogation of specific projections from lPBN to different downstream regions will provide insight into the functional roles of these outputs during a nocifensive response. In future studies, I propose to use in vivo calcium imaging to determine how different downstream targets respond to varying intensities of noxious stimulation. This would allow us to correlate nocifensive behavior with differing grades of calcium responses. Subsequently, we can manipulate specific lPBN pathways and determine how such perturbations affect both behavior and calcium responses. Together, these experiments would shed light on how different intensities of lPBN activity, via physiological responses to noxious stimuli,

relate to graded behavioral responses (Browne et al., 2017; Espejo and Mir, 1993; Fan et al., 1995; Le Bars, 2002).

5.2 The lPBN as a coordinator of physiological and behavioral responses to threat

How do different forms of noxious stimuli recruit lPBN pathways?

Our data support the idea that divergent lPBN pathways underlie behaviorally distinct repertoires that promote either escape-like behavior (dPBN pathway) or aversive memory (elPBN). Furthermore, we found that the dynorphin-expressing population may convey noxious signals from the environment to engage the different lPBN subnuclei, namely the CGRP-expressing population in the elPBN. An outstanding question relates to the mechanisms through which these circuits are engaged. One possibility is that the lPBN respond to all modalities of sensory stimuli, noxious and non-noxious, that either pose a potential threat or causes tissue damage, and the intensity of potential damage is correlated with the degree of lPBN activity (Campos et al., 2018). Lower intensity stimuli may engage specific subpopulations of lPBN neurons, and their degree of activity consequently recruits downstream populations commensurate to the level of lPBN activation. Higher intensity stimulation may result in the full behavioral expression of a particular circuit – that is, dynamic locomotor actions in addition to the formation of an aversive memory. These scenarios describe how lPBN networks may be engaged during acute exposure to specific stimuli.

The response during chronic pain may be more nuanced. A recent study found that chronic constriction injury of the infraorbital nerve, a model of neuropathic pain, resulted in hyperexcitability of lPBN neurons as measured by increased after-discharges and rebound firing

to mechanical and thermal stimulation (Uddin et al., 2018). Whether this resulted from neuroplastic changes at the presynaptic terminals, intrinsic properties of lPBN neurons, or from brain-wide changes was not investigated. Thus, the hyperexcitability of the lPBN during chronic pain may result in the manifestation of a broad range of pathological states that are typically comorbid with chronic pain (Nicholson and Verma, 2004; Scioli-Salter et al., 2015).

What is the functional relevance of collateralizing lPBN efferents?

In our study we identified collateralizing pathways from lPBN. Although we only studied those that exhibited robust axon terminals in downstream targets, we acknowledge that additional collaterals likely exist, either from those we identified in this study or separate subpopulations collateralizing to other brain regions (Liang et al., 2016a; Tokita et al., 2010). Specifically, we found collateralizations to CEA and BNST. Given the reciprocal connectivity with similar brain regions and with each other (Lebow and Chen, 2016), what would be the significance of inputs into these two areas from the same lPBN population? One possibility is that redundancy in these pathways would ensure that ascending input encoding threatening stimuli reach brain areas that mediate fear learning. However, these two regions have been implicated to facilitate different forms of conditioned learning: the BNST serving a more important role for learning to a diffuse, unspecified threat, compared to the CEA, which is thought to underlie conditioning to specific cues (Gungor and Pare, 2016; Walker and Davis, 1997; Walker et al., 2009). Whether this is the case and is reflected in efferents from lPBN to CEA and BNST remain to be definitively confirmed.

5.3 Future Directions

5.3.1 Genetically-defined subpopulations of lPBN and the regulation of autonomic functions

The entire PBN complex comprises at least 12 subnuclei that potentially underlie different aspects of coordinating autonomic regulation with behavioral responses. However, the contributions of distinct subregions or genetic subsets of lPBN neurons on physiology and behavior remain unclear. Experiments critical toward elucidating the contributions of lPBN activity with autonomic regulation and behavioral responses would involve improving our understanding of functionally distinct lPBN subpopulations. A previous study identified different levels of mRNA expression of various neuropeptides that were preferentially expressed within certain subregions (Maeda et al., 2009). We and others have identified different Cre-driver mouse lines that permit targeting of specific genetically defined lPBN subpopulations (Campos et al., 2018). Through our viral approach to screen different putative subpopulations, we identified several anatomically distinct populations. *Sst*^{Cre} and *Calb2*^{Cre} subsets localize almost exclusively in the elPBN, and we found that these neurons project to the same forebrain structures as those expressing CGRP, albeit at different intensity levels (data not shown). *Tacr1*^{CreER} and *Nts*^{Cre} neurons were found exclusively within dPBN, and both of these subsets appear to localize in different regions and exhibit unique morphology. Although prior studies have implicated *Crh*^{Cre} neurons in lPBN (Kainu et al., 1993), our viral tracing approaches revealed primarily neurons within the adjacent Kölliker-Fuse, a major contributor of the brainstem respiratory network (Bonis et al., 2010; Bonis et al., 2013; Chamberlin and Saper, 1994), and therefore will not be discussed

here. Below I outline the anatomical and neurochemical properties of these different lPBN subpopulations and speculate on their functional significance in physiology and behavior.

Sst^{Cre} in autonomic regulation

To our knowledge, the *Sst*^{Cre} population in the lPBN has not been characterized in great detail. It is likely that this population colocalizes to some degree with the CGRP-expressing population as both populations exhibit robust terminal labeling in the CEA. However, we found significantly fewer *Sst*^{Cre} - expressing axon terminals in the BNST, a forebrain region that also receives CGRP-positive lPBN input, and a small number of fibers in the DMH. The CGRP-expressing population has also been found to be glutamatergic, and most neurons within elPBN express *Vglut2*. These findings suggest that *Sst*^{Cre} neurons in lPBN are also excitatory. Although the post-synaptic targets of *Sst*^{Cre} lPBN neurons remain to be identified, they likely express the somatostatin receptor 2 (Sst2) (Dournaud et al., 1996; Schindler et al., 1997). Interestingly, somatostatin receptor signaling exerts an inhibitory effect. This raises the peculiar possibility that *Sst*^{Cre} neurons may be express both the neurotransmitter glutamate in addition to an inhibitory neuropeptide.

The phenomenon that neurons express opposing neuropeptides and neurotransmitters has been observed throughout the central nervous system (Tan and Bullock, 2008; van den Pol, 2012). The mechanisms through which glutamate and somatostatin release affects circuit activity and behavior remain uncertain, though a number of possibilities exist. For example, co-release of somatostatin and glutamate may occur locally or at a number of downstream regions, but the receptor for somatostatin may not be expressed, resulting in activation of the post-synaptic cells. Another possibility may relate to the intensity of *Sst*^{Cre} -positive neural activation. At low intensities of stimulation, *Sst*^{Cre} neurons may release the fast-acting neurotransmitter glutamate,

whereas high intensity activation may be required for neuropeptide release. This may be a mechanism through which *Sst*^{Cre}-expressing neurons in lPBN modulate neural activity, a strategy observed in other neural systems (Li and van den Pol, 2006). Lastly, somatostatin may act either pre-synaptically for feedback regulation or trans-synaptically to exert a regulatory role via local inhibition.

Within the hindbrain and brainstem somatostatin has been found to exert an inhibitory effect on sympathetic outflow. Somatostatin infusion into the rostral ventrolateral medulla (RVM) reduces blood pressure and heart rate. It also lowers the respiratory rate via prolongation of inspiration and reduction in expiration (Bou Farah et al., 2016; Stengel and Tache, 2017). Whether *Sst*^{Cre} -expressing lPBN neurons project to RVM, thereby providing the source of somatostatin, would be important to understanding how somatostatin signaling in RVM regulates these autonomic functions. Furthermore, to what degree these neurons interact with CGRP-positive elPBN neurons both locally and their post-synaptic targets in CEA would be important to understanding how the different lPBN circuits elicit responses to dangerous stimuli.

Calb2^{Cre} in pain affect

lPBN neurons expressing *Calb2* have also been found to exhibit projection patterns similar to CGRP-expressing and somatostatin-expressing neurons, with the latter two likely being a subset. *Calb2* encodes a calcium binding protein, but its functional significance within lPBN circuitry remains unclear. As *Calb2* is expressed in a glutamatergic population, one possibility is that it acts as an intracellular Ca^{2+} buffer to protect against excitotoxicity (Arai et al., 1991). As a neurochemically labeled population, *Calb2*^{Cre} neurons likely also express PACAP and may promote anxiogenic and pro-nociceptive states (Neugebauer, 2015). Future studies that manipulate

the activity of these neurons would help contribute toward our understanding of their role in autonomic regulation.

Tacr1^{CreER} and cardiovascular control during nociception

We found that neurons expressing the neurokinin-1 receptor (NK1R) exhibit wide branching morphology. Although these neurons do not extend into elPBN, their extensions appear to span almost all dPBN subnuclei. The nucleus solitary tract mediates sensory input from arterial baroreceptors and chemoreceptors into the same terminal fields as NK1R-expressing dPBN neurons (Davern, 2014; Norgren, 1978; Shapiro and Miselis, 1985). This would suggest that NK1R-expressing neurons in dPBN may integrate inputs related to autonomic functions with behavioral responses (Palmiter, 2018). Consistent with this idea, a number of studies have implicated their function in mediating cardiovascular responses to noxious stimulation. Intraplantar formalin administration induced reflex tachycardia, elevated heart rate, increased mean arterial pressure, and elicited nocifensive licking in rats (Boscan et al., 2005; Culman et al., 1997). In contrast, repeated noxious mechanical stimulation did not induce Fos expression in NK1R-expressing lPBN neurons, suggesting that prolonged noxious input is required for activation in this population (Pinto et al., 2003). Infusion of either GABA agonist or NK1R antagonist into lPBN attenuated the cardiovascular effects of formalin injection. However, only intracerebroventricular injections of NK1R antagonist reduced the nocifensive response. Together, these data would argue that NK1R-positive lPBN neurons may be more important in coordinating the cardiovascular responses not only to noxious stimuli, but more broadly to situations that may induce stress such as intraplantar formalin. The anti-nociceptive effects observed with intracerebroventricular injections of NK1R antagonists therefore may be mediated through other

brain regions expressing NK1R (Baulmann et al., 2000; Khasabov and Simone, 2013; Khasabov et al., 2017).

Nts^{Cre} and antinociception

Neurotensin is an excitatory neurotransmitter that acts primarily through G protein-coupled receptors (Neurotensin receptor 1 and neurotensin receptor 2). We found *Nts*^{Cre} neurons to be localized in dPBN, primarily within the ventral aspect within rostral dPBN, consistent with previous findings (Block and Hoffman, 1987). However, not much is known about its regulation of lPBN activity, whereas its role as a neuromodulator through its receptors NTS1 and NTS2 in the central nervous system has been described in different neural systems (Boules et al., 2013; Geisler et al., 2006). One group demonstrated that neurotensin injections into lPBN enhanced spontaneous activity and vagally-evoked activity (Saleh and Cechetto, 1993). Furthermore, sustained vagal stimulation depleted neurotensin within lPBN, suggesting *Nts*^{Cre} neurons respond to autonomic changes and release neurotensin to regulate visceral input locally at presynaptic terminals or downstream targets (Saleh, 1997). In our preliminary characterization of *Nts*^{Cre} neurons, we found dense projections to lPAG, particularly the ventrolateral aspect. It is possible that neurotensin release from *Nts*^{Cre} – positive lPBN terminals in the lPAG may underlie neurotensin's anti-nociceptive effects. Microinjections of neurotensin in lPAG resulted in glutamate release that acts through both glutamatergic and GABAergic mediators to recruit endogenous analgesia via the RVM (Feng et al., 2015; Kleczkowska and Lipkowski, 2013).

The advancements of mouse genetics and genetic tools to probe circuit function in vivo has enabled detailed analysis of how distinct populations of neurons, especially those within a heterogeneous mix, contribute to behavioral responses to external stimuli. How the populations of neurons detailed above participate in the regulation of autonomic responses, response to

nociception, and interactions with more other populations such as the *CGRP*^{Cre} subset would be of great interest to improve our understanding of lPBN circuitry.

5.3.2 Dynorphin and kappa opioid receptor in the lPBN

We found that optogenetic activation of *Pdyn*^{Cre} neurons in the lPBN resulted in aversive learning but not increased locomotor repertoires indicative of escape-like behavior. Furthermore, ablating *Pdyn*^{Cre} neurons blocked conditioned learning to formalin. The neural mechanism through which this occurs remains unclear. It is interesting that nearly all dynorphin-expressing neurons also co-express the vesicular glutamate transporter 2 (*Vglut2*). Dynorphin release acts on its cognate receptor kappa opioid receptor (KOR), an inhibitory G protein-coupled receptor. Thus, it may be counterintuitive that an inhibitory neuropeptide is co-expressed in glutamatergic neurons. Similar to *Sst*^{Cre} neurons, which are likely glutamatergic but also express the inhibitory neuropeptide somatostatin, the co-expression of opposing neurotransmitters may permit several neuromodulatory roles that are dependent on stimulus intensity (van den Pol, 2012). That is, the release of dynorphin may only occur following high intensity stimulation or at a specific frequency. Regardless, an important factor in determining whether dynorphin signaling occurs within local circuits of the lPBN is the presence of KOR. Our lab has generated a Cre-driver mouse line in which Cre recombinase has been knocked into the gene for KOR, *Oprk1* (Cai et al., 2016). In preliminary studies, we stereotaxically delivered Cre-dependent virus encoding a fluorescent reporter (eYFP) into the lPBN of *Oprk1*^{Cre} mice and visualized fluorescently-labeled cells throughout the entirety of the lPBN. This was confirmed with FISH to validate that the eYFP-positive cells co-localized with the *Oprk1* probe. With these tools, we can investigate the mechanism through which activation of *Pdyn*^{Cre} neurons recruits local lPBN neurons expressing

KOR. A step toward addressing this question would be understanding whether *Pdyn*^{Cre} neurons also express KOR, thereby permitting feedback regulation. Another possibility is that dynorphin release acts trans-synaptically through neighboring KOR-expressing neurons via local diffusion. Additional experiments are warranted to determine how manipulating these dynorphin- or KOR-expressing populations affect autonomic regulation and behavioral responses to distinct stimuli, such as those that present a potential threat.

5.3.3 Measuring lPBN-mediated arousal to noxious stimuli

The role of lPBN activity on mediating arousal has gained growing attention. Several groups have begun investigating the functional role of lPBN on reanimation from anesthesia with the motive that lPBN signaling may serve critical roles in the arousal system. Chemogenetic activation of glutamatergic lPBN neurons decreased emergence time from anesthesia, and this was reversed with with chemogenetic inhibition (Luo et al., 2018; Muindi et al., 2016; Wang et al., 2019). In line with these results, Fos expression was increased in brain regions implicated in sleep-wakefulness, and these were also downstream of lPBN projections. Furthermore, a recent study investigated how different lPBN projections to the preoptic area (POA) or lateral hypothalamus (LH) differ in their ability to generate arousal (Qiu et al., 2016). These studies clearly demonstrate the involvement of lPBN signaling on the sleep-arousal system. However, the evolutionary significance of lPBN activity on the arousal system is underappreciated. In all of our behavioral assays, we observed that optogenetic activation of lPBN pathways resulted in significant avoidance behavior during the real time place aversion assay. Such behavioral responses would invariably require an increased arousal state. The aversive aspect during photoactivation of these pathways suggest that increased arousal would enable an animal to respond appropriately to either noxious

or potentially dangerous stimuli. Thus, it is likely that these animals behaved in such a way because these pathways would also be recruited by exposure to noxious stimuli, thereby promoting behavioral and autonomic changes to ensure an animal's escape from and memory of potentially life-threatening stimuli (Kaur et al., 2013; Kaur and Saper, 2019; Kaur et al., 2017; Palmiter, 2018; Saper, 2016). Although our study did not measure changes in cortical activity, as measured by electroencephalogram (EEG), we hypothesize that the activation of lPBN outputs to the downstream regions in our study would promote brain-wide changes to favor a wakeful state as a result of exposure to potentially harmful stimuli. One possible way to test this would involve the use of Cre-mediated targeting of neural populations expressing Fos in response to noxious stimulation (Rodriguez et al., 2017; Sakurai et al., 2016).

Appendix Introduction

The Appendix comprises a compilation of other major projects and experiments that I have worked on throughout my graduate studies in Dr. Sarah Ross's lab. Appendix A features experiments to reveal the contributions of kappa opioid receptor signaling on primary afferents in neurogenic inflammation. Experiments were performed in the Ross lab. Appendix B highlights behavioral experiments that aim to determine whether Nogo receptor signaling mediates the in vivo effects of Aβ pathology on learning. These experiments were performed with Dr. Zachary Wills. Appendix C and D are clinical projects done with the Department of Neurosurgery. The first characterizes the effectiveness of fixed-pressure shunts for hydrocephalus in an adult cohort. The second is a case report on a pediatric patient with the rare diagnosis of Schimmelpenning syndrome. Additional projections that I have contributed can be found in the following PubMed link: https://www.ncbi.nlm.nih.gov/myncbi/1rKQBuyLmspky/bibliography/public/

Appendix A Kappa opioid receptor signaling inhibits neurogenic inflammation

Primary afferents are known to be inhibited by kappa opioid receptor (KOR) signaling. How KOR signaling contributes to neurogenic inflammation remains unclear. Based on the finding that KOR is expressed in mouse and human peptidergic afferents, we sought to address whether KOR activation could inhibit neurogenic inflammation. To address this question, we measured plasma extravasation in mice that had received an intraplantar injection of capsaicin in the presence or absence of a KOR agonist (Figure 19A). For these experiments, we compared the effects of nalfurafine, a centrally penetrating KOR agonist (Endoh et al., 2001; Nagase et al., 1998), to those of either ICI204,488 or FE200665 (Vanderah, 2010), two peripherally restricted KOR agonists that have extremely limited ability to cross the blood-brain barrier (Shaw et al., 1989; Vanderah, 2010). In control mice, treatment with the TRPV1 agonist capsaicin resulted in a significant increase in Evans blue in the ipsilateral paw relative to the contralateral paw. In contrast, treatment with any of the three KOR agonists significantly reduced capsaicin-induced plasma extravasation (Figures 19B and 19C). These observations are consistent with previous data (Green and Levine, 1992). Similar results were observed when neurogenic inflammation was induced with an inflammatory mixture of bradykinin and prostaglandin E2 (Figure 20). Importantly, we found that nalfurafine failed to attenuate Evans blue extravasation in $KOR^{-/-}$ mice, confirming that the inhibition of neurogenic inflammation by nalfurafine is specific to KOR (Figure 19D). Finally, as an independent measure of neurogenic inflammation, we also assessed the effects of KOR agonists on the increase in paw temperature observed following capsaicin-injection into the hindpaw. Intraplantar injection of capsaicin in vehicle-treated mice resulted in an increase in paw temperature that was significantly attenuated in mice treated with either nalfurafine or ICI204,488

(Figures 19E and 19F). Together, these results suggest that activation of KOR in the periphery is sufficient to inhibit neurogenic inflammation.

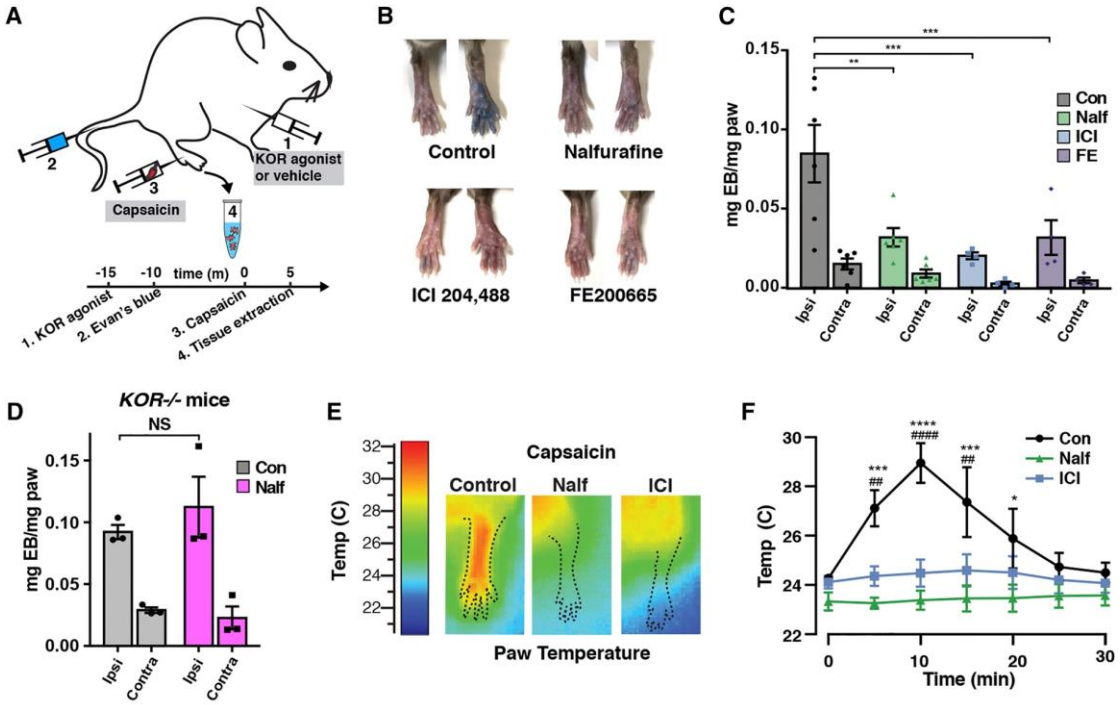

Figure 19 Peripherally Selective KOR Agonists Inhibit Neurogenic Inflammation and Sensitization of Nociceptive Afferents.

(A) Schematic illustrating experimental design to measure the effect of KOR agonists on plasma extravasation induced by capsaicin. (B and C) Representative images (B) and quantification (C) of Evans blue extravasation upon injection of capsaicin (0.1%) into the ipsilateral paw of mice pretreated with vehicle (Control), nalfurafine (20 mg/kg), ICI204,448 (10 mg/kg), or FE200665 (12 mg/kg), as indicated. Data are presented as mean ± SEM, and symbols represent data points from individual animals (two-way ANOVA followed by Tukey's post hoc test; *$p < 0.05$; n = 4–6 mice/condition). (D) Capsaicin-induced Evans blue extravasation in $KOR^{-/-}$ mice treated with vehicle (Con) or nalfurafine (Nalf, 20 mg/kg). Data are represented as mean + SEM, and symbols represent data points from individual animals (two-way ANOVA; NS $p > 0.05$; n = 3 mice/condition) (E and F) Representative images (E) and quantification (F) of infrared thermography to assess paw temperature. Injection of capsaicin (0.1%) caused a transient increase in the temperature of the ipsilateral paw of mice pretreated with vehicle (Control), which was significantly greater than that observe in mice pretreated with nalfurafine (20 mg/kg) or ICI204,448 (10 mg/kg), as indicated. Data represent mean ± SEM (two-way ANOVA followed by Holm-Sidak multiple comparison test; * or # indicates $p < 0.05$ between nalfurafine and vehicle or ICI and vehicle groups, respectively; n = 4–5 mice/condition).

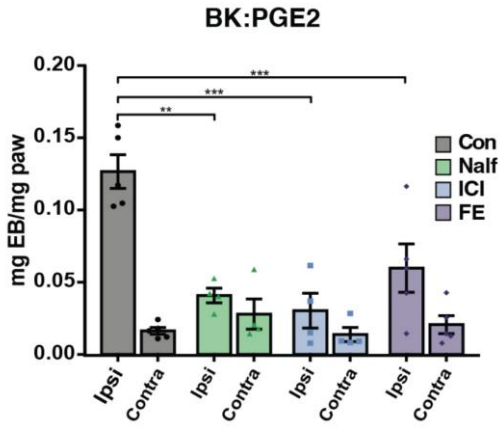

Figure 20 KOR agonists inhibit neurogenic inflammation induced by bradykinin and prostaglandin E2.

Evans blue extravasation upon injection of bradykinin:prostaglandin E2 (10 μM:10 μM, 10μL) into the ipsilateral paw of mice pretreated with vehicle (Con), nalfurafine (Nalf, 20 μg/kg), ICI204,448 (ICI, 10 mg/kg), or FE200665 (FE, 12 mg/kg), as indicated. Data are mean ± SEM and symbols represent data points from individual animals (two-way ANOVA followed by Tukey's post hoc test; ** $p < 0.01$; *** $p < 0.001$, $n = 4 – 5$ mice/condition).

Appendix B ADDLs Block Learning via NgR-Mediated Inhibition of Spine Assembly and T-Type Channels

An important measure of Aβ pathology is its impact on learning. To determine the role of NgRs in Aβ-mediated inhibition of learning, we introduced ADDLs (~10 pmols) via a single intracerebroventricular (ICV) injection into the mouse brain (Figures 21A and 22A) and examined its impact on novel object recognition (NOR) learning. Consistent with previous work (Figueiredo et al., 2013), ADDLs block NOR learning 7 days after ICV injection in comparison to control (DMSO)-injected animals (Figure 21B and Figure 22B). In contrast, NgR family knockouts (NgRNNN) are unaffected by ADDLs, showing normal NOR behavior (right panel). Note that none of the ICV-injected animals show deficits in movement (open field analysis; Figure 22C). These findings suggest NgRs mediate Aβ's inhibition of learning.

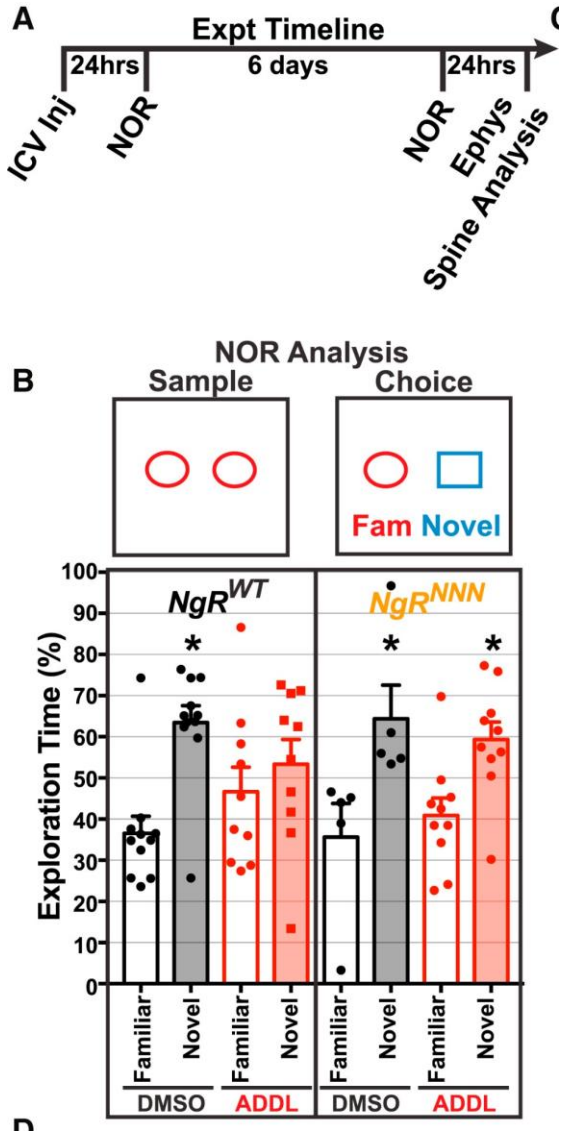

Figure 21 ADDLs Block NOR Learning by NgR Family-Mediated Inhibition of Spine Assembly and T-Type Currents

(A) Timeline of ICV injections, NOR behavioral analysis, acute slice recordings, and dendritic spine analysis. (B) ADDL-mediated deficits in novel object learning rescued by NgR family loss. Top: illustration of NOR sample and choice test with familiar (Fam) and novel (Nov) objections assessing 2-hr retention memory. Bottom: quantification of exploration time with indicated objects following ICV injections with DMSO (0.8 μL of 2% DMSO) or ADDLs (0.8 μL of 50 μM Aβ monomer equivalent). n = animals indicated by circles. Bars represent means; error bars SEM. ∗$p < 0.05$ versus fixed 50% (chance), Student's t test.

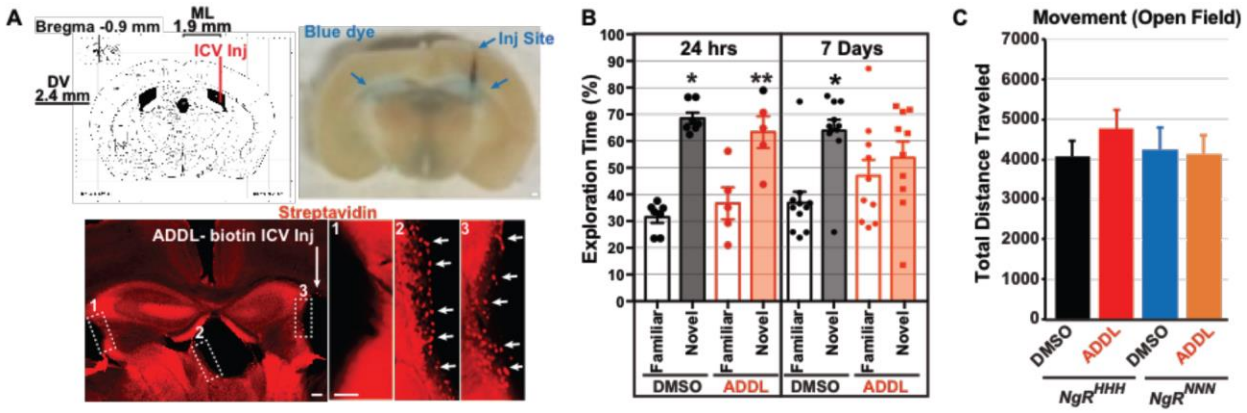

Figure 22 Extended Analysis of ICV Injections of ADDLs

(A) (Left) Mouse atlas indicating stereotactic location of ICV injections. (Right) Mouse brain section 2 hours following test injection with blue dye illustrating injection site and spread of dye to right and left ventricles (blue arrows). (Below) Immunostained mouse brain section 24 hours following biotin-LC-ADDL ICV injection. Hatched boxes (numbered) are expanded on the right highlighting (white arrows) the biotin-LC-ADDL labeling of the central (2) and right ventricles (3). Note the absence of staining in left ventricle (1). Scale bar = 100μm. (B) Novel object recognition analysis at indicated times (24 hours or 7 days) following ICV injection of control animals (8-week-old C57B6 males). Quantification of the mean exploration time with indicated objects (familiar or novel) and indicated conditions (2% DMSO or ADDLs ICV). Error bars equal SEM. (n) indicated by circles (each representing an animal) in graph. * $p<0.01$ **$p<0.05$ vs 50% (chance) Student's t test. (C) Quantification of the mean total distance travelled in open field analysis for indicated animals (NgR genotypes) and conditions (2% DMSO or ADDLs ICV). Error bars equal SEM. n = 8 - 13 mice per group.

Appendix C Exclusive use of fixed pressure valves for cerebrospinal fluid diversion in a modern adult cohort.

C.1 Introduction

The introduction of ventriculoperitoneal shunt insertion transformed the treatment of hydrocephalus and continues to be the most frequently used method of hydrocephalus management in both pediatric and adult patient populations (Patwardhan and Nanda, 2005; Weisenberg et al., 2016). Gradually, fixed pressure valve systems have lost ground against newer programmable valve systems as the favored device of choice for shunt insertion. Such enhancements have been purported to provide reductions in risks for shunt malfunction and improved dynamic management of intracranial pressure (Hanlo et al., 2003; Mpakopoulou et al., 2012; Stein and Guo, 2008). Despite this, the rates of complication and shunt revision persist and contribute to the cost of treatment (Merkler et al., 2017; Patwardhan and Nanda, 2005; Simon et al., 2008; Stein and Guo, 2008; Stone et al., 2013). Thus, no clear consensus exists for the use of programmable over that of nonprogrammable shunts (Hatlen et al., 2012; Ringel et al., 2005; Stone et al., 2013; Xu et al., 2013).

Much of the published literature comparing the costs and clinical outcomes of programmable versus nonprogrammable shunt insertions focuses on shunt use in the pediatric hydrocephalus population (Lam et al., 2014; Pollack et al., 1999; Simon et al., 2008). Furthermore, few longitudinal studies have evaluated the management of hydrocephalus in adult patients with fixed shunts in a modern cohort (Khan et al., 2015; Korinek et al., 2011; Reddy et al., 2012, 2014; Reddy et al., 2011). Here, we investigated in detail the characteristics and outcomes of an adult

patient population who universally received fixed valve shunt insertion as the initial treatment of hydrocephalus by a single physician.

C.2 Materials and Methods

Data collection

We retrospectively examined clinical records within our institution from January 2000 through March 2017 of all adult patients who underwent fixed shunt placement by a single physician, Daniel Wecht (DW) for treatment of hydrocephalus at the University of Pittsburgh Medical Center. All patients received peritoneal-based catheters during their initial shunt placement. Patients that had received shunts previously by other providers were not included. Indications for shunt placement were categorized as follows: hemorrhage, normal pressure hydrocephalus (NPH), pseudotumor cerebri, tumor, and infection. The small number of patients whose etiology of hydrocephalus did not fit the above categories were grouped as others and comprise the following: traumatic brain injury, ischemic stroke, and hydrocephalus of unknown etiology.

Definitions

Patients who received shunt insertion for hydrocephalus were identified using current procedural code (CPT) 62223 as well as an electronic medical record query for the term (shunt) among patients who had been seen by the senior author. The category “hemorrhage” comprised any non-traumatic intracranial hemorrhage including subarachnoid, intraventricular, and intraparenchymal hemorrhages. Shunt revisions were defined as reoperation on a previously

implanted shunt for any indication. Mechanical failure of the shunt was determined during reoperations for shunt revisions by selectively cannulating the valve and the tubing distal to the valve and assessing for the presence of drainage and normal flow using a barometer filled to 35 mm H20. The proximal catheter was observed after removal of the shunt valve to determine proximal obstruction. The shunt was removed and assessed for any obstruction or inability to drain properly proximally, distally, or at the valve. Any shunt that fulfilled either criteria was considered a malfunction due to mechanical failure. Overdrainage and underdrainage were determined by radiographic findings combined with clinical symptoms, such as positional headache, and the absence of any mechanical problem with the proximal shunt, distal shunt, or the valve itself during intraoperative inspection.

Patients with pseudotumor or NPH diagnoses were selected based on clinical improvement of relevant symptoms after high volume lumbar puncture or three-day lumbar drain trial. In the case of pseudotumor cerebri, the presence documented, progressive vision loss was also an indication. Patient with hemorrhage and other forms of acute hydrocephalus typically underwent prior placement of an external ventricular drain, with a gradual attempt at weaning the drain via incremental increases in the pressure level followed by a 24–48 hour clamp trial, being attempted. Patients unable to be weaned from external cerebrospinal fluid drainage had shunts placed.

Analysis

Statistical analysis was performed with GraphPad Prism 7.0 and IBM SPSS version 25. Chi-squared and Fisher's exact test was performed on categorical data. Mann-Whitney tests were used for continuous variables between two groups. Kaplan-Meier curves were performed on survival data and comparisons were made using the log-rank (Mantel-Cox) test. Comparisons

among three or more groups were made using Kruskal-Wallis test followed by Dunn's post-hoc test. The level of significance was $p < 0.05$.

C.3 Results

We collected data from 169 patients who had undergone insertion of fixed shunts between 2000 and 2017 for the treatment of hydrocephalus. We excluded 43 patients who had been previously shunted, resulting in 126 patients shunted by a single physician. One hundred twenty-three of 126 (97.6%) of patients received parietal ventriculoperitoneal (VP) shunting. Occipital and frontal shunting were performed in 2 (1.6%) and 1 (0.8%) of initial operations, respectively. One hundred twenty-three of 126 (97.6%) operations used Pudenz valves. One operation involved insertion of a Delta valve and the remaining two patients received Heyer-Schulte valves. The majority of valve pressures were set at medium (118 of 125, 94.4%). Seven of 125 were set at low (5.6%). These patients were subsequently categorized into etiologies for hydrocephalus: hemorrhagic, NPH, tumor, pseudotumor cerebri, infection, and others (see below). Of the patients with low valve pressure settings, 4 of 7 (57.1%) fell into the hemorrhagic group, 2 of 7 (28.6%) had tumors, and 1 of 7 (14.3%) had an infection.

The distribution of patients across hydrocephalus etiologies is as follows: hemorrhagic (54 of 126, 42.9%), NPH (48 of 126, 38.1%), tumor (8 of 126, 6.3%), pseudotumor cerebri (7 of 126, 5.6%), infection (1 of 126, 0.8%), and others (8 of 126, 6.3%) (Table 1). Forty-eight (38%) patients were male whereas 78 (62%) were female. Further details of the distribution of male and female patients across etiologies of hydrocephalus can be found in Table 2. When categorized by etiology, we found the following mean ages of male and female patients respectively: 58.4 ± 6.1 vs. 56.8 ±

4.7 years (hemorrhagic), 74.9 ± 3.8 vs. 71.3 ± 3.3 years (NPH), 59.8 ± 15.3 vs. 71.7 ± 23.2 years (tumor), and 52.7 ± 15 vs. 58.4 ± 8 years (other). Only females exhibited pseudotumor cerebri at a mean age of 31 ± 5.1 years. A single female patient with infectious etiology was 75 years old.

Table 2 Distribution of patients receiving fixed valve shunts and shunt revisions.

Etiology	Patient number (%)	Shunt revisions (%)	Follow up time
Hemorrhage	54 (42.9)	14 (42.4)	22.5 ± 5.2
NPH	48 (38.1)	13 (39.4)	28.1 ± 7.1
Infection	1 (0.8)	0 (0)	1.7
Other	8 (6.3)	4 (12.1)	43.6 ± 17.4
Pseudotumor cerebri	7 (5.6)	2 (6.1)	7.1 ± 4.7
Tumor	8 (6.3)	0 (0)	65.9 ± 64.5
Total	**126 (100)**	**33 (100)**	**28.1 ± 6.1**

Curved bracketed values indicate proportion of total. Follow up time is indicated in months as mean ± standard error.

No differences in proportion of shunt failures were found between males and females (Fisher's exact test, p = 0.5467). However, when stratified by etiology the proportion of shunt revisions was greater in female than in male patients with NPH (p = 0.0158, Table 2). Mean follow up time for all patients was 28.1 ± 6.1 months (Table 1). By etiology, the follow up times are listed: 22.5 ± 5.2 months (hemorrhagic), 28.1 ± 7.1 months (NPH), 7.1 ± 4.7 months (pseudotumorerebri), 65.9 ± 64.5 months (tumor), and 43.6 ± 17.4 months (other). A single patient with infectious etiology followed up in 1.7 months.

Table 3 Distribution of shunt revisions across genders and etiology of hydrocephalus.

	Revisions	None	Total	Revisions	None	Total	value
Hemorrhage	5	19	24	9	21	30	0.328
NPH	8	8	16	5	27	32	0.0158
Infection	0	0	0	0	1	1	NA
Other	2	1	3	2	3	5	NA
Pseudotumor cerebri	0	0	0	2	5	7	NA
Tumor	0	5	5	0	3	3	NA
Total	**15**	**33**	**48**	**18**	**60**	**78**	

NA indicates not applicable.

Shunt revision

Thirty three of 126 patients (26.2%) required at least one shunt revision (Table 3), with mechanical shunt malfunction (13 of 33, 39.4% of failures) being the most common reason for failure. Six of 13 malfunctions resulted from mechanical failure at the valve, 2 of 13 occurred proximally, and 5 of 13 occurred distally. Shunt infection was the second most common reason for shunt revisions (7 of 33, 21.2% of failures, 5.6% of all patients). Of note, antibiotic impregnated catheters are not routinely used at our institution in adults. Shunts migration occurred in 6 of 33 (18.2% of failures) of patients. Misplaced shunts accounted for three of 33 (9.1% of failures) of shunt revisions. Both overdrainage and underdrainage each resulted in 2 (6.1% of failures) shunt revisions, and all 4 patients whose shunts failed for this reason had NPH. Importantly, all shunts were functional in patients experiencing overdrainage and underdrainage.

Table 4 Distribution of number of shunt revisions.

Number of revisions	Number of patients (%)	
1	19	(57.6)
2	10	(30.3)
3	1	(3)
4	2	(6.1)
5	1	(3)
Total	**33**	**100**

When stratified by etiology of hydrocephalus compared to number of patients requiring at least one revision, a large percentage of patients (14 of 33, 42.4% of failures) whose shunts required revision developed hydrocephalus initially as a result of hemorrhage. A similar proportion was found in patients who required treatment for NPH (13 of 33, 39.4% of failures). Two patients (6.1% of failures) with pseudotumor cerebri required treatment shunt failure, while no shunts failed in patients treated for hydrocephalus due to tumor or infection. Four patients (12.1%) whose etiology of hydrocephalus did not fall in the above categories required shunt revision (Table 1).

When considering shunt revisions as a fraction of the total number of shunt placements by etiology, shunt revisions occurred in similar proportions among those with hemorrhage (14 of 54, 25.9%), NPH (13 of 48, 27.1%), and pseudotumor cerebri (2 of 7, 28.6%). Two of 4 (50%) patients categorized as “others” required shunt revision. Zero patients in either “infection” or “tumor” groups required revision ($p = 0.165$). Furthermore, the rate of revisions between the hemorrhage and NPH groups that received fixed shunts were not different ($p = 0.873$, Fig. 1).

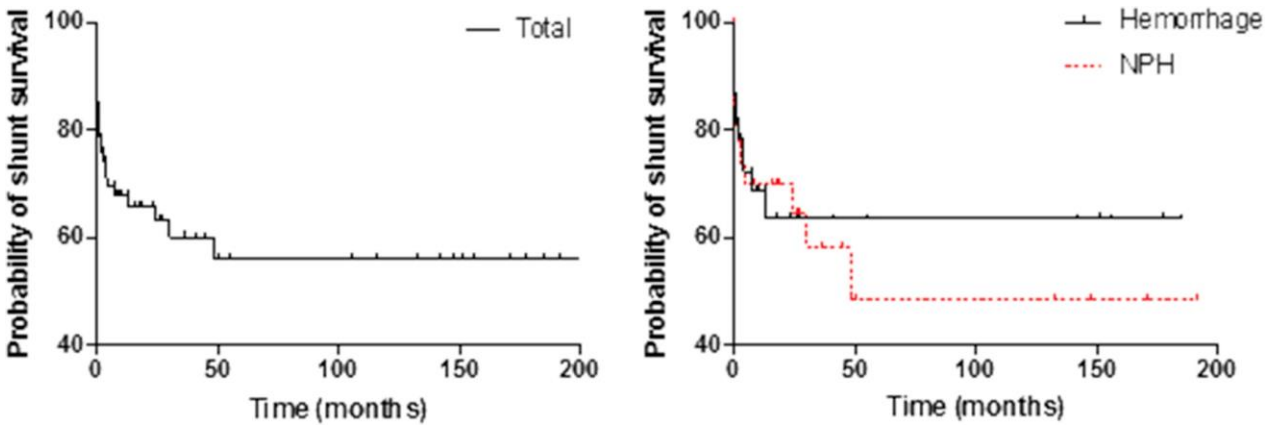

Figure 23 Survival curve of shunts.

(Left) All patients (Right) Hemorraghic and NPH groups. Log-rank test was performed.

Nineteen of 33 patients (57.6%) required a single revision. Ten of 33 patients (30.3%) required two shunt revisions during follow up. Four of 33 patients (12.1%) required three or more revisions. Together, shunt revisions occurred at an average rate of 1.7 ± 0.2 per patient among those requiring at least one revision.

Presenting symptoms

Of 126 patients who received insertion of fixed VP shunt, we were able to characterize the preoperative symptomology of 109 patients: 41 from hemorrhagic, 46 from NPH, 1 from infection, 8 from other, 7 from pseudotumor cerebri, and 8 from tumor. Across all etiologies, 69 of 109 patients (63.3%) exhibited decreased cognitive deterioration, 61 (56%) presented with gait disturbances, 34 (31.2%) presented with urinary incontinence, and 31 (28.4%) presented with headaches. A smaller number of patients presented with the following symptoms: decreased wakefulness (17 of 109, 15.6%); nausea and/or vomiting (11 of 109, 10.1%); vertigo (5 of 109, 4.6%), blurry vision (8 of 109, (7.3%), or papilledema (6 of 109, 5.5%). No patients presented pre-operatively with double vision. By etiology, the most common symptoms presented within the

hemorrhagic group were headaches (23 of 41, 56%) and cognitive decline (22 of 41, 53.7%). The most common symptoms within the pseudotumor cerebri group were headaches (4 of 7, 57.1%), blurry vision (7 of 7, 100%), and papilledema (6 of 7, 85.7%). The majority of patients within the tumor group presented with cognitive decline (6 of 8, 75%) and gait instability (3 of 8, 37.5%) (Table 4).

Table 5 Summary of presenting symptoms by etiology.

Presenting symptoms	Hemorrhage (n = 41)	NPH (n = 46)	Infection (n = 1)	Other (n = 8)	Pseudotumor cerebri (n = 7)
Headache	23 (56.1)	2 (4.3)	0	1 (12.5)	4 (57.1)
Double Vision	0	0	0	0	0
Blurry Vision	1 (2.4)	0	0	0	7 (100)
Papilledema	0	0	0	0	6 (85.7)
Cognitive Decline	22 (56.7)	35 (76.1)	1 (100)	4 (50.0)	1 (14.3)
Decreased Wakefulness	13 (31.7)	2 (4.35)	0	2 (25.0)	0
Gait Instability	7 (17.0)	44 (95.7)	1 (100)	6 (75.0)	0
Urinary incontinence	3 (7.3)	29 (63.0)	0	1 (12.5)	0
Nausea/vomiting	11 (26.8)	0	0	0	0
Vertigo	2 (4.9)	1 (2.2)	0	1 (12.5)	0

Values indicate number of patients with symptoms. Parentheses indicate the percent of patients within categories.

Post-operative symptom effect

We found that 47 of 126 (37.3%) patients passed away at the time the data was collected. No deaths were associated with the peri- or post-operative surgical complications. Of those patients the mean survival length from the time of shunt insertion until mortality date was 50.3 ± 6.5 months.

We next characterized the resolution of symptomology patient by patient following shunt insertion and found 74 patients who met criteria to compare their pre-operative and post-operative symptomology: 23 from hemorrhage, 33 from NPH, 1 from infection, 5 from other, 6 from pseudotumor cerebri, and 6 from tumor. Fixed shunt insertion was found to resolve headaches in 13 of 17 patients (76.5%), blurry vision in 5 of 6 patients (83.3%), papilledema in 5 of 6 patients (83.3%), cognitive decline in 39 of 43 patients (90.7%), decreased wakefulness in 8 of 9 patients (88.9%), gait instability in 35 of 43 patients (81.4%), urinary incontinence in 19 of 22 patients 86.4%), nausea/vomiting in 3 of 4 patients (75%), and vertigo in 2 of 3 patients (66.7%). Further details regarding the resolution of symptoms by etiology are found in Table 5.

Table 6 Summary of resolved symptoms following shunt insertion by patient.

Resolved symptoms	Hemorrhage (n = 23)	NPH (n = 33)	Infection (n = 1)	Other (n = 5)	Pseudotumor cerebri (n = 6)
Headache	11 of 12 (91.7)	0 of 1	0	0	2 of 3 (66.7)
Double Vision	0	0	0	0	0
Blurry Vision	0	0	0	0	5 of 6 (83.3)
Papilledema	0	0	0	0	5 of 6 (83.3)
Cognitive Decline	7 of 9 (77.8)	23 of 24 (95.8)	1 of 1 (100)	3 of 3 (100)	1 of 1 (100)
Decreased Wakefulness	6 of 7 (85.7)	2 of 2 (100)	0	0	0
Gait Instability	3 of 3 (100)	25 of 31 (80.6)	1 of 1 (100)	4 of 5 (80.0)	0
Urinary incontinence	1 of 1 (100)	16 of 19 (84.2)	0	1 of 1 (100)	0
Nausea/vomiting	3 of 4 (75)	0	0	0	0
Vertigo	1 of 1 (100)	1 of 1 (100)	0	0	0

Parentheses indicate the percent of resolved symptoms within each category.

C.4 Discussion

Although hydrocephalus arises from diverse etiologies, VP shunt insertion continues to be the most frequently used treatment in both the pediatric and adult patient populations (Merkler et al., 2017; Stein and Guo, 2008; Wu et al., 2007). Despite significant technological advancements and constructions of ventriculoperitoneal shunts, the rates of complication following shunt insertion remain considerable and contribute to the excessive cost of treatment (Hanlo et al., 2003; Hoshide et al., 2017; Kestle et al., 2005; Lifshutz and Johnson, 2001). Here, we detailed the use of fixed shunts in 126 patients from 2000 – 2017 from a single physician. A major concern for the use of fixed shunts is the complication of overdrainage or underdrainage of cerebrospinal fluid (CSF) (Xu et al., 2013). We found that 26.2% of patients with a fixed shunt required at least one revision, and the most common cause of shunt revision was due to malfunction, making up 39.4% of failures. This is consistent with previous studies (Borgbjerg et al., 1995; Di Rocco et al., 1994; Kaestner et al., 2017; Wu et al., 2007).

Etiology of hydrocephalus has also been found to be correlated with frequency of shunt revisions. In our study, patients in either hemorrhage or NPH categories accounted for the majority of shunt revisions (42.4% and 39.4%, respectively). However, the proportion of shunt failures were similar in either groups (25.9% and 27.1%, respectively). This may be explained by the differences in number of patients in each of our categories. Nevertheless, the low proportion of failures in those shunted for NPH is comparable to those found in previous studies (Kaestner et al., 2017; McGirt et al., 2005). Overdrainage and underdrainage reflected only 6.1% of failures, respectively (2 of 33). Interestingly, all four patients suffering from symptoms due to overdrainage or underdrainage had an initial diagnosis of NPH. Those with symptoms of underdrainage were

revised to a low pressure fixed valve with no further complications, whereas the two patients with overdrainage issues subsequently received a Strata valve set to 2.5 and Delta valve set to 2.5.

Shunt insertion was found to resolve a large proportion of presenting symptoms. Nearly all patients with hemorrhagic hydrocephalus experienced headache resolution as well as improvements in cognitive decline and decreased wakefulness. Patients with NPH primarily presented with cognitive decline, gait instability and urinary incontinence that were also resolved. Hydrocephalus due to pseudotumor cerebri caused primarily headaches, blurry vision, and papilledema. Shunt insertion resolved these symptoms in the majority of patients.

A major concern for the use of programmable shunts is its significant cost compared to that of fixed shunts. At our institution, the total shunt supply implant cost and direct supply expenses for programmable shunts were more expensive than using fixed valves (Agarwal et al., 2018). The lack of consensus over the cost-benefit of using a more expensive programmable valve has generally been mixed.

C.5 Limitations

Several limitations of our study may have biased our results. Our study retrospectively reviews the data of patients receiving fixed shunts. We therefore cannot randomize prospectively matched groups, subjecting our analysis to potential confounding bias. Furthermore, data was collected from a single institution that predisposes our study to selection bias based upon the demographics at this institution.

C.6 Conclusion

Our study characterizes the clinical outcomes of a modern cohort of adult patients receiving fixed shunts by a single physician at our institution for the treatment of hydrocephalus due to diverse etiologies. We further compare the clinical outcomes for patients receiving fixed shunts to those that of programmable shunts. From the patient population evaluated in this study, hydrocephalus occurred most frequently as a result of NPH or hemorrhage, and the revision rates were similar between these two groups. Shunt malfunction was found to be the primary reason for failure. The proportion of failed shunts remains considerable and comparable to those in decades past. Given the experience of the physician performing these shunt insertions, our study highlights the need for improvements in the design of fixed shunt valve designs to reduce failures resulting from malfunction.

Appendix D Is Schimmelpenning syndrome associated with intracranial tumors? A case report.

D.1 Introduction

Schimmelpenning syndrome, or linear sebaceous nevus syndrome (OMIM 163200) is a rare, well-defined constellation of clinical phenotypes associated with the presence of nevus sebaceous. It classically presents with well-defined yellow-orange plaques located on the scalp or neck and cerebral, ocular, and skeletal defects (Happle, 2010). Through various DNA sequencing techniques, a number of groups have consistently and independently identified the same mutation in the *HRAS* or *KRAS* genes as the primary mechanism responsible for the majority of the clinical manifestations. Mutations in pro-oncogenic signaling pathways increase the likelihood of nevus sebaceous to develop malignant potential, and up to 24% of these patients develop secondary cutaneous neoplasms (Moody et al., 2012). However, extracutaneous neoplasms associated with the central nervous system have rarely been reported in Schimmelpenning syndrome patients (Baker et al., 1987). We report a rarely described case of a child with a diagnosis of Schimmelpenning syndrome and a central nervous system tumor in this case a pilocytic astrocytoma (PA).

D.2 Radiographical findings

A 15-year-old male patient diagnosed with Schimmelpenning syndrome as a neonate presented to the Children's Hospital of Pittsburgh after a generalized tonic-clonic seizure. An electroencephalogram detected focal epileptiform discharges in the left hemisphere. A head computed tomography scan revealed multiple calcified abnormalities, largely within the left temporal lobe (Fig. 24). A magnetic resonance imaging (MRI) scan of the brain identified a heterogeneously enhancing expansile lesion with cystic components measuring 3.3 × 1.8 × 2.3 cm centered in the left temporal stem. Two additional expansile lesions were identified, one adjacent to the left foramen of Monro and the other adjacent to the choroid plexus in the atrium of the left lateral ventricle, measuring 1.6 × 1 × 0.8 cm and 2.5 × 1.3 × 1.3 cm, respectively (Fig. 25). No midline shift was seen. An MRI of the spine was negative. Of note, the patient had a non-contrast brain MRI during infancy for unrelated reasons which did not demonstrate an obvious lesion.

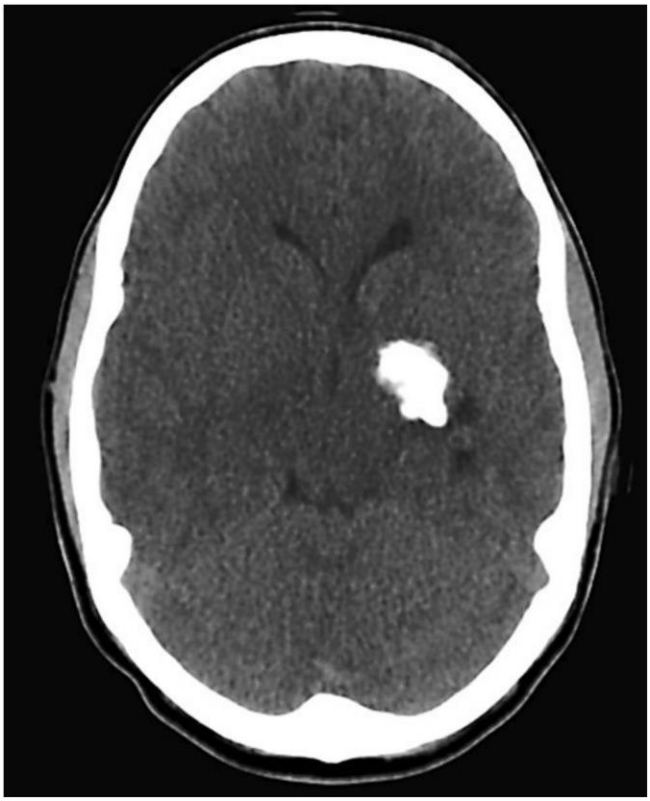

Figure 24 Preoperative transverse computed tomography image indicating a calcified lesion abutting the temporal horn

Operative Course

Following a frontotemporal craniotomy and dural opening, a temporal corticectomy was made and the ventricle was entered. The tissue of the medial ventricular wall was soft, grayish, and abnormal. When the tumor had been largely debulked by both visual inspection and neuronavigation, resection was terminated. Total resection was not attempted given the presence of the metastatic lesions and adjacent critical structures. Molecular analysis revealed no abnormalities in the proto-oncogenes BRAF, HRAS, or KRAS. Histopathological analysis confirmed the sampled tissue to be a WHO grade 1 PA. The case was reviewed in a neuropathological consensus conference with complete agreement on the diagnosis. The patient recovered with no neurological deficits and was discharged on postoperative day 5. The patient

has been closely followed with serial MRIs, and at the time of this report, 6 months after surgery, no evidence of tumor progression has been noted. Chemotherapy will be administered only for progression.

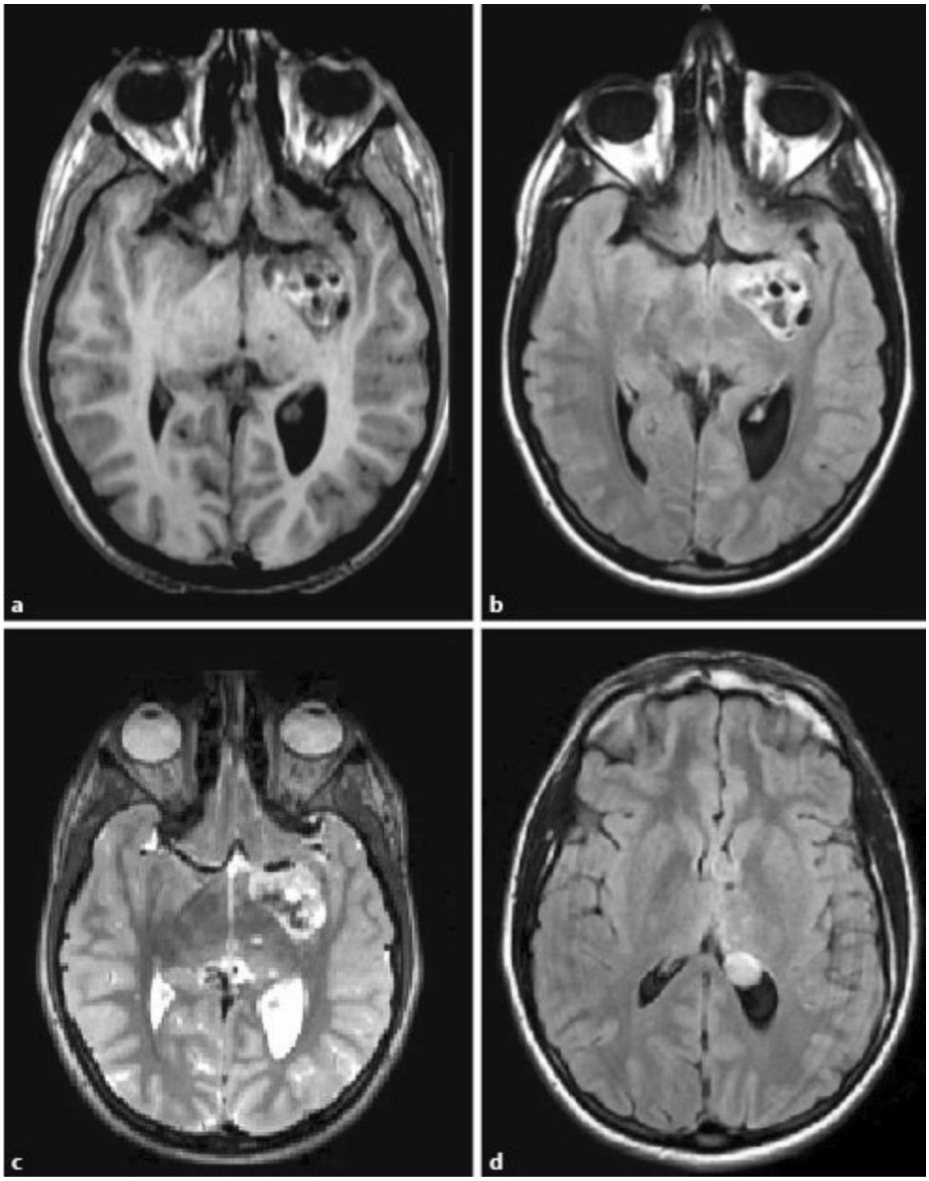

Figure 25 Radiographic images of intracranial mass.

Preoperative T1 images with contrast (a), FLAIR (b), and T2 (c) MRI sequences demonstrating a heterogeneously enhancing, cystic mass of the temporal stem abutting the hippocampus and temporal horn of the lateral ventricle with no significant edema

and minimal mass effect on adjacent structures. (d) FLAIR sequence depicting left foramen of Monro and left atrial satellite lesions.

Table 7 Summary of intracranial lesions associated with Schimmelpenning syndrome and associated disorders

Disorder	Tumor	Reference
Unclear (Schimmel-penning-like)	Astrocytoma	Watanabe et al. [41], 2016
Nevus unius lateralis	Astrocytoma of anterior hypothalamus	Meyerson [13], 1967
Epidermal nevus syndrome	Gliomatosis cerebri	Choi and Kudo [26], 1981
Nevus unius lateralis	Mixed glioma	Andriola [14], 1976
Organoid nevus syndrome	Meningo-encephalo-angioneurinomatosis	Clancy et al. [17], 1985
Epidermal nevus syndrome	Medulloblastoma	Okumura et al. [35], 2012
Unclear (phakomatosis pigmentovascularis-like)	Optic pathway glioma	Seifert et al. [16], 2012
Linear sebaceous nevus syndrome	Optic glioma	Sato et al. [15], 1994
Linear sebaceous nevus syndrome	Leptomeningeal hemangioma	Mollica et al. [32], 1974
Linear sebaceous nevus syndrome	(1) Choroid plexus papilloma; (2) anterior horn ependyma; (3) frontal lobe calcification	Levin et al. [29], 1984
Schimmelpenning	Parenchymal cyst	Kamate et al. [28], 2009
Linear sebaceous nevus syndrome	Choroidal hemangioma	Yan et al. [42], 2007
Linear sebaceous nevus syndrome	Cerebellar venous angioma	Seawright et al. [38], 1996
Organoid nevus syndrome	Scleral choristoma	Shields et al. [40], 2014
Epidermal nevus syndrome	Complex choristoma; osteoma; arachnoid cysts	Sharma et al. [39], 2012
Linear sebaceous nevus syndrome	Complex choristoma	Lin and Yan [30], 2010
Linear sebaceous nevus syndrome	Complex choristoma; hemimegalencephaly	Park et al. [36], 2009
Linear sebaceous nevus syndrome	Complex conjunctival choristoma	Brodsky et al. [23], 1997
Epidermal nevus syndrome	Choroidal osteoma; complex choristoma	Mullaney and Weatherhead [34], 1996
Epidermal nevus syndrome	Hypothalamic hamartoma	Rizzo and Pavone [37], 2015
Nevus sebaceous	Hamartoma	Moskowitz and Honig [33], 1982
Linear sebaceous nevus syndrome	Hamartoma of the right lateral ventricle	Barth et al. [21], 1977
ECCL	CNS lipoma	Chandravanshi [25], 2014
Epidermal nevus syndrome	Left orbital and left cerebellopontine angle cistern lipomas	Canyigit and Oguz [24] 2006
Epidermal nevus syndrome	Intraspinal lipoma	Booth and Rollins [22], 2002
ECCL	CNS lipoma	Mall et al. [31], 2000
ECCL	CNS lipoma	Grimalt et al. [27], 1993

D.3 Discussion

This report concerns a patient with a clinical diagnosis of Schimmelpenning syndrome who presented with a seizure secondary to a low-grade astrocytoma. Compelling data indicates that nearly all tissue samples from lesions of Schimmelpenning syndrome patients, but not from normal adjacent tissue of the same individual due to the mosaic nature of the condition, exhibit mutations in either HRAS or KRAS. Most predominantly, the hotspot mutation in HRAS c.37G>C causes a p.G13R substitution that constitutively activates the Ras/Raf/ MAPK signaling pathway (Groesser et al., 2012), supporting the conclusion that Schimmelpenning syndrome arises from genetic mosaicism resulting in an autosomal dominant RASopathy (Happle, 2013). Schimmelpenning syndrome patients most commonly present with skeletal, neurological, and ocular extracutaneous features. Neurological abnormalities have been previously reported to occur in the majority of cases, although one study found neurological deficits in only 14 of 196 cases (7%) (Baker et al., 1987; van de Warrenburg et al., 1998). Major neurological features include mental retardation, seizures, and structural cerebral deformities such as hemimegalencephaly. The full clinical phenotype of these neurological features may gradually develop over time. In our patient, no records indicated neurological involvement at birth. Furthermore, neurological examination revealed no remarkable abnormalities other than the presenting new onset generalized seizures caused by the PA. Ophthalmologic abnormalities have also been commonly reported in individuals with Schimmelpenning syndrome (Diven et al., 1987). These ocular features frequently manifest as lipodermoids, choristomas, and colobomas. We observed in our patient a unilateral corneal dermoid cyst resulting in severe anisometropic amblyopia.

Neurological symptoms occur fairly commonly in patients with Schimmelpenning syndrome. However, as noted above, the full clinical presentation of neurological symptoms may

only develop as affected patients age because physiological abnormalities resulting from anatomical deformities, such as maldeveloped cranial nerves and neurovascular defects, develop over time. Furthermore, the growth of cerebral neoplasms may contribute to the constellation of neurological symptoms, including increased intracranial pressure, head circumference enlargement, and seizures. Additional studies investigating intracranial tumor involvement and the manifestation of neurological symptoms are warranted. Nevertheless, the rare incidence of extracutaneous neoplasms involving the central nervous system and gradual development of neurological symptoms would argue for careful monitoring for the sudden onset of any neurological symptoms (Happle, 2010). Genetic testing should be performed on affected tissues evaluating for mutations in genes affecting the Ras/Raf/MAPK signaling pathways.

Sporadic PAs have been found to arise primarily through chromosomal 7q34 duplication generating a novel fusion protein comprising the KIAA1549 locus and BRAF kinase domain (Bar et al., 2008; Jacob et al., 2009). Despite their generally indo lent nature, PAs have been associated with neurofibromatosis type 1 (NF1), with approximately 15% of NF1 patients developing PA (Listernick et al., 2007). The NF1 gene encodes the GTPase-activating protein neurofibromin, which acts as a negative regulator of RAS. Mutations in neurofibromin result in the autosomal dominant phenotype of NF1, driven by increased activity of RAS and the downstream MAPK and mechanistic target of rapamycin (mTOR) signaling pathways (Helfferich et al., 2016). Interestingly, optic pathway gliomas in NF1 patients have been found to progress more slowly compared to sporadic tumors (Helfferich et al., 2016; Koeller and Rushing, 2004).

In contrast, the occurrence of extracutaneous neoplasms affecting the central nervous system, most of which appear benign, have rarely been observed in Schimmelpenning syndrome patients. In one report a patient presenting with nevus unius lateralis was found to have a grade 1

astrocytoma in the right anteromedial temporal lobe, possibly originating from the hypothalamus (Meyerson, 1967). A second case reported a mixed glioma originating from the left parietal region (Alfonso et al., 1987). Optic gliomas have been observed in a handful of Schimmelpenning syndrome patients. Similar to those found in NF1 patients, optic gliomas were detected in children and were of an indolent nature (Sato et al., 1994; Seifert et al., 2012). Whereas preclinical studies using genetic mice to alter the expression of neurofibromin have found preferential development of optic gliomas compared to other NF1-associated tumors (Listernick et al., 2007), no such studies have been performed to determine the relationship between Schimmelpenning syndrome and the development of any intracranial tumors. However, the close relationship between these two conditions, the occurrence of PAs, and the Ras signaling pathway suggest involvement of a common pathway in their pathogenesis.

Cerebral hamartomas have also been found in Schimmelpenning syndrome patients, although this occurs infrequently as well (Clancy et al., 1985). Benign congenital tumors such as choristomas and hemangiomas have been reported in Schimmelpenning syndrome patients. Choristomas have typically been reported affecting the epibulbar region and demonstrate several histological features (Alfonso et al., 1987). Complex choristomas typically contain ectodermal and mesodermal tissues such as cartilage and bone (Pe'er and Ilsar, 1995). Lipomas have been reported in patients with encephalocraniocutaneous lipomatosis (ECCL), which symptomatically appears similar to those with Schimmelpenning syndrome. These include cerebral malformations and cutaneous and ocular anomalies, including choristomas. However, a benign lipoma of the scalp underlying regions of alopecia, known as nevus psiloliparus, occurs uniquely with ECCL. The presence of benign lipomas elsewhere in the central nervous system also occurs frequently in ECCL patients (Moog et al., 2007). The location of these benign neoplasms affecting the nervous

system strongly suggests that these tumors arise from RASopathy within either the ectoderm or neuroectoderm during development. Although small benign masses within the central nervous system may pose a limited risk, the possibility of potential growth should be of concern as their enlargement may cause a mass effect resulting in the compression of neighboring structures and consequent development of neurological abnormalities. A summary of Schimmelpenning syndrome and related disorders with intracranial masses is documented in Table 1 (Barth et al., 1977; Booth and Rollins, 2002; Brodsky et al., 1997; Canyigit and Oguz, 2006; Chandravanshi, 2014; Choi and Kudo, 1981; Grimalt et al., 1993; Kamate et al., 2009; Levin et al., 1984; Lin and Yan, 2010; Mall et al., 2000; Meyerson, 1967; Mollica et al., 1974; Moskowitz and Honig, 1982; Okumura et al., 2012; Park et al., 2009; Rizzo and Pavone, 2015; Sato et al., 1994; Seawright et al., 1996; Seifert et al., 2012; Sharma et al., 2012; Shields et al., 2014; Watanabe et al., 2016; Yan et al., 2007).

In a recently reported case, an infant presented with multisystem involvement similar to that of Schimmelpenning syndrome and an anaplastic astrocytoma resulting from a BRAF V600E mutation, but no mutations HRAS or KRAS (Watanabe et al., 2016). These rare cases suggest the possibility that Schimmelpenning syndrome may arise through different mosaic RASopathies, and the presenting PA in our patient may be associated with Schimmelpenning syndrome independent of a HRAS or KRAS mutation. A recent case report identified a 4-month-old patient diagnosed with Schimmelpenning syndrome resulting from a postzygotic NRAS mutation, although no PA was reported (Kuroda et al., 2015). Despite the rare incidence of Schimmelpenning syndrome patients developing astrocytomas, it is possible that these individuals have a predisposition to develop pro-oncogenic extracutaneous mutations. The strong association between HRAS and KRAS mutations in Schimmelpenning syndrome patients and lack of PA suggests a potential

common signaling pathway in RASopathy, as defects in other genes regulating the RAS signaling pathway also results in an increased incidence of intracranial neoplastic involvement (Canyigit and Oguz, 2006; Helfferich et al., 2016; Listernick et al., 2007; Watanabe et al., 2016). Therefore, future studies will be needed to determine the convergence or involvement of different RASopathies that ultimately give rise to the intracranial tumors mentioned in Table 1. Whether the PAs in Schimmelpenning syndrome patients exhibit a more benign development compared to those with sporadic PA, as the optic gliomas do, remains to be determined.

Bibliography

Agarwal, N., Kashkoush, A., McDowell, M.M., Lariviere, W.R., Ismail, N., and Friedlander, R.M. (2018). Comparative durability and costs analysis of ventricular shunts. J Neurosurg, 1-8.

Alfonso, I., Howard, C., Lopez, P.F., Palomino, J.A., and Gonzalez, C.E. (1987). Linear nevus sebaceous syndrome. A review. J Clin Neuroophthalmol *7*, 170-177.

Alhadeff, A.L., Su, Z., Hernandez, E., Klima, M.L., Phillips, S.Z., Holland, R.A., Guo, C., Hantman, A.W., De Jonghe, B.C., and Betley, J.N. (2018). A Neural Circuit for the Suppression of Pain by a Competing Need State. Cell *173*, 140-152 e115.

Arai, R., Winsky, L., Arai, M., and Jacobowitz, D.M. (1991). Immunohistochemical localization of calretinin in the rat hindbrain. J Comp Neurol *310*, 21-44.

Babaev, O., Piletti Chatain, C., and Krueger-Burg, D. (2018). Inhibition in the amygdala anxiety circuitry. Exp Mol Med *50*, 18.

Baker, R.S., Ross, P.A., and Baumann, R.J. (1987). Neurologic complications of the epidermal nevus syndrome. Arch Neurol *44*, 227-232.

Bar, E.E., Lin, A., Tihan, T., Burger, P.C., and Eberhart, C.G. (2008). Frequent gains at chromosome 7q34 involving BRAF in pilocytic astrocytoma. J Neuropathol Exp Neurol *67*, 878-887.

Barik, A., Thompson, J.H., Seltzer, M., Ghitani, N., and Chesler, A.T. (2018). A Brainstem-Spinal Circuit Controlling Nocifensive Behavior. Neuron *100*, 1491-1503 e1493.

Barth, P.G., Valk, J., Kalsbeek, G.L., and Blom, A. (1977). Organoid nevus syndrome (linear nevus sebaceus of Jadassohn): clinical and radiological study of a case. Neuropadiatrie *8*, 418-428.

Basbaum, A.I., and Fields, H.L. (1978). Endogenous pain control mechanisms: review and hypothesis. Ann Neurol *4*, 451-462.

Basbaum, A.I., and Fields, H.L. (1984). Endogenous pain control systems: brainstem spinal pathways and endorphin circuitry. Annu Rev Neurosci *7*, 309-338.

Baulmann, J., Spitznagel, H., Herdegen, T., Unger, T., and Culman, J. (2000). Tachykinin receptor inhibition and c-Fos expression in the rat brain following formalin-induced pain. Neuroscience *95*, 813-820.

Ben-Shaul, Y. (2017). OptiMouse: a comprehensive open source program for reliable detection and analysis of mouse body and nose positions. BMC Biol *15*, 41.

Benarroch, E.E. (2016). Parabrachial nuclear complex: Multiple functions and potential clinical implications. Neurology *86*, 676-683.

Benarroch, E.E. (2018). Brainstem integration of arousal, sleep, cardiovascular, and respiratory control. Neurology *91*, 958-966.

Bernard, J.F., and Besson, J.M. (1990). The spino(trigemino)pontoamygdaloid pathway: electrophysiological evidence for an involvement in pain processes. J Neurophysiol *63*, 473-490.

Bernard, J.F., Bester, H., and Besson, J.M. (1996). Involvement of the spino-parabrachio -amygdaloid and -hypothalamic pathways in the autonomic and affective emotional aspects of pain. Prog Brain Res *107*, 243-255.

Bernard, J.F., Huang, G.F., and Besson, J.M. (1994). The parabrachial area: electrophysiological evidence for an involvement in visceral nociceptive processes. J Neurophysiol *71*, 1646-1660.

Bester, H., Matsumoto, N., Besson, J.M., and Bernard, J.F. (1997). Further evidence for the involvement of the spinoparabrachial pathway in nociceptive processes: a c-Fos study in the rat. J Comp Neurol *383*, 439-458.

Block, C.H., and Hoffman, G.E. (1987). Neuropeptide and monoamine components of the parabrachial pontine complex. Peptides *8*, 267-283.

Bonis, J.M., Neumueller, S.E., Krause, K.L., Kiner, T., Smith, A., Marshall, B.D., Qian, B., Pan, L.G., and Forster, H.V. (2010). A role for the Kolliker-Fuse nucleus in cholinergic modulation of breathing at night during wakefulness and NREM sleep. J Appl Physiol (1985) *109*, 159-170.

Bonis, J.M., Neumueller, S.E., Krause, K.L., Pan, L.G., Hodges, M.R., and Forster, H.V. (2013). Contributions of the Kolliker-Fuse nucleus to coordination of breathing and swallowing. Respir Physiol Neurobiol *189*, 10-21.

Booth, T.N., and Rollins, N.K. (2002). MR imaging of the spine in epidermal nevus syndrome. AJNR Am J Neuroradiol *23*, 1607-1610.

Borgbjerg, B.M., Gjerris, F., Albeck, M.J., Hauerberg, J., and Borgesen, S.E. (1995). Frequency and causes of shunt revisions in different cerebrospinal fluid shunt types. Acta Neurochir (Wien) *136*, 189-194.

Boscan, P., Dutschmann, M., Herbert, H., and Paton, J.F. (2005). Neurokininergic mechanism within the lateral crescent nucleus of the parabrachial complex participates in the heart-rate response to nociception. The Journal of neuroscience : the official journal of the Society for Neuroscience *25*, 1412-1420.

Bou Farah, L., Bowman, B.R., Bokiniec, P., Karim, S., Le, S., Goodchild, A.K., and McMullan, S. (2016). Somatostatin in the rat rostral ventrolateral medulla: Origins and mechanism of action. J Comp Neurol *524*, 323-342.

Boules, M., Li, Z., Smith, K., Fredrickson, P., and Richelson, E. (2013). Diverse roles of neurotensin agonists in the central nervous system. Front Endocrinol (Lausanne) *4*, 36.

Bourgeais, L., Gauriau, C., Monconduit, L., Villanueva, L., and Bernard, J.F. (2003). Dendritic domains of nociceptive-responsive parabrachial neurons match terminal fields of lamina I neurons in the rat. J Comp Neurol *464*, 238-256.

Bourgeais, L., Monconduit, L., Villanueva, L., and Bernard, J.F. (2001). Parabrachial internal lateral neurons convey nociceptive messages from the deep laminas of the dorsal horn to the intralaminar thalamus. J Neurosci *21*, 2159-2165.

Brodsky, M.C., Kincannon, J.M., Nelson-Adesokan, P., and Brown, H.H. (1997). Oculocerebral dysgenesis in the linear nevus sebaceous syndrome. Ophthalmology *104*, 497-503.

Browne, L.E., Latremoliere, A., Lehnert, B.P., Grantham, A., Ward, C., Alexandre, C., Costigan, M., Michoud, F., Roberson, D.P., Ginty, D.D., *et al.* (2017). Time-Resolved Fast Mammalian Behavior Reveals the Complexity of Protective Pain Responses. Cell Rep *20*, 89-98.

Buritova, J., Besson, J.M., and Bernard, J.F. (1998). Involvement of the spinoparabrachial pathway in inflammatory nociceptive processes: a c-Fos protein study in the awake rat. J Comp Neurol *397*, 10-28.

Cai, X., Huang, H., Kuzirian, M.S., Snyder, L.M., Matsushita, M., Lee, M.C., Ferguson, C., Homanics, G.E., Barth, A.L., and Ross, S.E. (2016). Generation of a KOR-Cre knockin mouse strain to study cells involved in kappa opioid signaling. Genesis *54*, 29-37.

Cameron, D., Polgar, E., Gutierrez-Mecinas, M., Gomez-Lima, M., Watanabe, M., and Todd, A.J. (2015). The organisation of spinoparabrachial neurons in the mouse. Pain *156*, 2061-2071.

Campos, C.A., Bowen, A.J., Roman, C.W., and Palmiter, R.D. (2018). Encoding of danger by parabrachial CGRP neurons. Nature *555*, 617-622.

Campos, C.A., Bowen, A.J., Schwartz, M.W., and Palmiter, R.D. (2016). Parabrachial CGRP Neurons Control Meal Termination. Cell Metab *23*, 811-820.

Canyigit, M., and Oguz, K.K. (2006). Epidermal nevus syndrome with internal carotid artery occlusion and intracranial and orbital lipomas. AJNR Am J Neuroradiol *27*, 1559-1561.

Carleton, A., Accolla, R., and Simon, S.A. (2010). Coding in the mammalian gustatory system. Trends Neurosci *33*, 326-334.

Carter, M.E., Han, S., and Palmiter, R.D. (2015). Parabrachial calcitonin gene-related peptide neurons mediate conditioned taste aversion. The Journal of neuroscience : the official journal of the Society for Neuroscience *35*, 4582-4586.

Carter, M.E., Soden, M.E., Zweifel, L.S., and Palmiter, R.D. (2013). Genetic identification of a neural circuit that suppresses appetite. Nature *503*, 111-114.

Cechetto, D.F., and Calaresu, F.R. (1985). Central pathways relaying cardiovascular afferent information to amygdala. Am J Physiol *248*, R38-45.

Cechetto, D.F., Standaert, D.G., and Saper, C.B. (1985). Spinal and trigeminal dorsal horn projections to the parabrachial nucleus in the rat. J Comp Neurol *240*, 153-160.

Chamberlin, N.L., Mansour, A., Watson, S.J., and Saper, C.B. (1999). Localization of mu-opioid receptors on amygdaloid projection neurons in the parabrachial nucleus of the rat. Brain Res *827*, 198-204.

Chamberlin, N.L., and Saper, C.B. (1992). Topographic organization of cardiovascular responses to electrical and glutamate microstimulation of the parabrachial nucleus in the rat. J Comp Neurol *326*, 245-262.

Chamberlin, N.L., and Saper, C.B. (1994). Topographic organization of respiratory responses to glutamate microstimulation of the parabrachial nucleus in the rat. The Journal of neuroscience : the official journal of the Society for Neuroscience *14*, 6500-6510.

Chandravanshi, S.L. (2014). Encephalocraniocutaneous lipomatosis: a case report and review of the literature. Indian J Ophthalmol *62*, 622-627.

Chaplan, S.R., Bach, F.W., Pogrel, J.W., Chung, J.M., and Yaksh, T.L. (1994). Quantitative assessment of tactile allodynia in the rat paw. J Neurosci Methods *53*, 55-63.

Chen, J.Y., Campos, C.A., Jarvie, B.C., and Palmiter, R.D. (2018). Parabrachial CGRP Neurons Establish and Sustain Aversive Taste Memories. Neuron *100*, 891-899 e895.

Choi, B.H., and Kudo, M. (1981). Abnormal neuronal migration and gliomatosis cerebri in epidermal nevus syndrome. Acta Neuropathol *53*, 319-325.

Ciocchi, S., Herry, C., Grenier, F., Wolff, S.B., Letzkus, J.J., Vlachos, I., Ehrlich, I., Sprengel, R., Deisseroth, K., Stadler, M.B., *et al.* (2010). Encoding of conditioned fear in central amygdala inhibitory circuits. Nature *468*, 277-282.

Clancy, R.R., Kurtz, M.B., Baker, D., Sladky, J.T., Honig, P.J., and Younkin, D.P. (1985). Neurologic manifestations of the organoid nevus syndrome. Arch Neurol *42*, 236-240.

Coizet, V., Dommett, E.J., Klop, E.M., Redgrave, P., and Overton, P.G. (2010). The parabrachial nucleus is a critical link in the transmission of short latency nociceptive information to midbrain dopaminergic neurons. Neuroscience *168*, 263-272.

Culman, J., Klee, S., Ohlendorf, C., and Unger, T. (1997). Effect of tachykinin receptor inhibition in the brain on cardiovascular and behavioral responses to stress. The Journal of pharmacology and experimental therapeutics *280*, 238-246.

Davern, P.J. (2014). A role for the lateral parabrachial nucleus in cardiovascular function and fluid homeostasis. Front Physiol *5*, 436.

Davis, M., Walker, D.L., Miles, L., and Grillon, C. (2010). Phasic vs sustained fear in rats and humans: role of the extended amygdala in fear vs anxiety. Neuropsychopharmacology *35*, 105-135.

Di Rocco, C., Marchese, E., and Velardi, F. (1994). A survey of the first complication of newly implanted CSF shunt devices for the treatment of nontumoral hydrocephalus. Cooperative survey of the 1991-1992 Education Committee of the ISPN. Childs Nerv Syst *10*, 321-327.

Diven, D.G., Solomon, A.R., McNeely, M.C., and Font, R.L. (1987). Nevus sebaceus associated with major ophthalmologic abnormalities. Archives of dermatology *123*, 383-386.

Dournaud, P., Gu, Y.Z., Schonbrunn, A., Mazella, J., Tannenbaum, G.S., and Beaudet, A. (1996). Localization of the somatostatin receptor SST2A in rat brain using a specific anti-peptide antibody. J Neurosci *16*, 4468-4478.

Endoh, T., Tajima, A., Izumimoto, N., Suzuki, T., Saitoh, A., Suzuki, T., Narita, M., Kamei, J., Tseng, L.F., Mizoguchi, H., *et al.* (2001). TRK-820, a selective kappa-opioid agonist, produces potent antinociception in cynomolgus monkeys. Jpn J Pharmacol *85*, 282-290.

Espejo, E.F., and Mir, D. (1993). Structure of the rat's behaviour in the hot plate test. Behav Brain Res *56*, 171-176.

Fadok, J.P., Krabbe, S., Markovic, M., Courtin, J., Xu, C., Massi, L., Botta, P., Bylund, K., Muller, C., Kovacevic, A., *et al.* (2017). A competitive inhibitory circuit for selection of active and passive fear responses. Nature *542*, 96-100.

Fan, R.J., Shyu, B.C., and Hsiao, S. (1995). Analysis of nocifensive behavior induced in rats by CO2 laser pulse stimulation. Physiol Behav *57*, 1131-1137.

Feil, K., and Herbert, H. (1995). Topographic organization of spinal and trigeminal somatosensory pathways to the rat parabrachial and Kolliker-Fuse nuclei. J Comp Neurol *353*, 506-528.

Feng, Y.P., Wang, J., Dong, Y.L., Wang, Y.Y., and Li, Y.Q. (2015). The roles of neurotensin and its analogues in pain. Curr Pharm Des *21*, 840-848.

Flak, J.N., Arble, D., Pan, W., Patterson, C., Lanigan, T., Goforth, P.B., Sacksner, J., Joosten, M., Morgan, D.A., Allison, M.B., *et al.* (2017). A leptin-regulated circuit controls glucose mobilization during noxious stimuli. J Clin Invest *127*, 3103-3113.

Flak, J.N., Patterson, C.M., Garfield, A.S., D'Agostino, G., Goforth, P.B., Sutton, A.K., Malec, P.A., Wong, J.T., Germani, M., Jones, J.C., *et al.* (2014). Leptin-inhibited PBN neurons enhance responses to hypoglycemia in negative energy balance. Nature neuroscience *17*, 1744-1750.

Fu, O., Iwai, Y., Kondoh, K., Misaka, T., Minokoshi, Y., and Nakajima, K.I. (2019). SatB2-Expressing Neurons in the Parabrachial Nucleus Encode Sweet Taste. Cell Rep *27*, 1650-1656 e1654.

Fulwiler, C.E., and Saper, C.B. (1984). Subnuclear organization of the efferent connections of the parabrachial nucleus in the rat. Brain Res *319*, 229-259.

Garfield, A.S., Li, C., Madara, J.C., Shah, B.P., Webber, E., Steger, J.S., Campbell, J.N., Gavrilova, O., Lee, C.E., Olson, D.P., *et al.* (2015). A neural basis for melanocortin-4 receptor-regulated appetite. Nature neuroscience *18*, 863-871.

Garfield, A.S., Shah, B.P., Madara, J.C., Burke, L.K., Patterson, C.M., Flak, J., Neve, R.L., Evans, M.L., Lowell, B.B., Myers, M.G., Jr., *et al.* (2014). A parabrachial-hypothalamic cholecystokinin neurocircuit controls counterregulatory responses to hypoglycemia. Cell Metab *20*, 1030-1037.

Gauriau, C., and Bernard, J.F. (2002a). Pain pathways and parabrachial circuits in the rat. Exp Physiol *87*, 251-258.

Gauriau, C., and Bernard, J.F. (2002b). Pain pathways and parabrachial circuits in the rat. Exp Physiol *87*, 251-258.

Geerling, J.C., Kim, M., Mahoney, C.E., Abbott, S.B., Agostinelli, L.J., Garfield, A.S., Krashes, M.J., Lowell, B.B., and Scammell, T.E. (2016). Genetic identity of thermosensory relay neurons in the lateral parabrachial nucleus. Am J Physiol Regul Integr Comp Physiol *310*, R41-54.

Geerling, J.C., and Loewy, A.D. (2007). Sodium depletion activates the aldosterone-sensitive neurons in the NTS independently of thirst. Am J Physiol Regul Integr Comp Physiol *292*, R1338-1348.

Geerling, J.C., and Loewy, A.D. (2008). Central regulation of sodium appetite. Exp Physiol *93*, 177-209.

Geerling, J.C., Yokota, S., Rukhadze, I., Roe, D., and Chamberlin, N.L. (2017). Kolliker-Fuse GABAergic and glutamatergic neurons project to distinct targets. Journal of Comparative Neurology *525*, 1844-1860.

Geisler, S., Berod, A., Zahm, D.S., and Rostene, W. (2006). Brain neurotensin, psychostimulants, and stress--emphasis on neuroanatomical substrates. Peptides *27*, 2364-2384.

Green, P.G., and Levine, J.D. (1992). Delta- and kappa-opioid agonists inhibit plasma extravasation induced by bradykinin in the knee joint of the rat. Neuroscience *49*, 129-133.

Grimalt, R., Ermacora, E., Mistura, L., Russo, G., Tadini, G.L., Triulzi, F., Cavicchini, S., Rondanini, G.F., and Caputo, R. (1993). Encephalocraniocutaneous lipomatosis: case report and review of the literature. Pediatr Dermatol *10*, 164-168.

Groesser, L., Herschberger, E., Ruetten, A., Ruivenkamp, C., Lopriore, E., Zutt, M., Langmann, T., Singer, S., Klingseisen, L., Schneider-Brachert, W., *et al.* (2012). Postzygotic HRAS and KRAS mutations cause nevus sebaceous and Schimmelpenning syndrome. Nat Genet *44*, 783-787.

Gungor, N.Z., and Pare, D. (2016). Functional Heterogeneity in the Bed Nucleus of the Stria Terminalis. J Neurosci *36*, 8038-8049.

Guo, Z.L., Moazzami, A.R., and Longhurst, J.C. (2005). Stimulation of cardiac sympathetic afferents activates glutamatergic neurons in the parabrachial nucleus: relation to neurons containing nNOS. Brain Res *1053*, 97-107.

Guthmann, A., Fritschy, J.M., Ottersen, O.P., Torp, R., and Herbert, H. (1998). GABA, GABA transporters, GABA(A) receptor subunits, and GAD mRNAs in the rat parabrachial and Kolliker-Fuse nuclei. J Comp Neurol *400*, 229-243.

Han, S., Soleiman, M.T., Soden, M.E., Zweifel, L.S., and Palmiter, R.D. (2015a). Elucidating an Affective Pain Circuit that Creates a Threat Memory. Cell *162*, 363-374.

Han, S., Soleiman, M.T., Soden, M.E., Zweifel, L.S., and Palmiter, R.D. (2015b). Elucidating an Affective Pain Circuit that Creates a Threat Memory. Cell *162*, 363-374.

Hanlo, P.W., Cinalli, G., Vandertop, W.P., Faber, J.A., Bogeskov, L., Borgesen, S.E., Boschert, J., Chumas, P., Eder, H., Pople, I.K., *et al.* (2003). Treatment of hydrocephalus determined by the European Orbis Sigma Valve II survey: a multicenter prospective 5-year shunt survival study in children and adults in whom a flow-regulating shunt was used. J Neurosurg *99*, 52-57.

Happle, R. (2010). The group of epidermal nevus syndromes Part I. Well defined phenotypes. J Am Acad Dermatol *63*, 1-22; quiz 23-24.

Happle, R. (2013). Nevus sebaceus is a mosaic RASopathy. J Invest Dermatol *133*, 597-600.

Harrison, T.A., Hoover, D.B., and King, M.S. (2004). Distinct regional distributions of NK1 and NK3 neurokinin receptor immunoreactivity in rat brainstem gustatory centers. Brain Res Bull *63*, 7-17.

Hatlen, T.J., Shurtleff, D.B., Loeser, J.D., Ojemann, J.G., Avellino, A.M., and Ellenbogen, R.G. (2012). Nonprogrammable and programmable cerebrospinal fluid shunt valves: a 5-year study. J Neurosurg Pediatr *9*, 462-467.

Hayward, L.F., and Felder, R.B. (1999). Electrophysiological properties of rat lateral parabrachial neurons in vitro. Am J Physiol *276*, R696-706.

Helfferich, J., Nijmeijer, R., Brouwer, O.F., Boon, M., Fock, A., Hoving, E.W., Meijer, L., den Dunnen, W.F., and de Bont, E.S. (2016). Neurofibromatosis type 1 associated low grade gliomas: A comparison with sporadic low grade gliomas. Crit Rev Oncol Hematol *104*, 30-41.

Herbert, H., and Bellintani-Guardia, B. (1995). Morphology and dendritic domains of neurons in the lateral parabrachial nucleus of the rat. J Comp Neurol *354*, 377-394.

Herbert, H., Moga, M.M., and Saper, C.B. (1990). Connections of the parabrachial nucleus with the nucleus of the solitary tract and the medullary reticular formation in the rat. J Comp Neurol *293*, 540-580.

Hermanson, O., and Blomqvist, A. (1996). Subnuclear localization of FOS-like immunoreactivity in the rat parabrachial nucleus after nociceptive stimulation. J Comp Neurol *368*, 45-56.

Hermanson, O., and Blomqvist, A. (1997). Subnuclear localization of FOS-like immunoreactivity in the parabrachial nucleus after orofacial nociceptive stimulation of the awake rat. J Comp Neurol *387*, 114-123.

Hooks, B.M., Lin, J.Y., Guo, C., and Svoboda, K. (2015). Dual-channel circuit mapping reveals sensorimotor convergence in the primary motor cortex. J Neurosci *35*, 4418-4426.

Hoshide, R., Meltzer, H., Dalle-Ore, C., Gonda, D., Guillaume, D., and Chen, C.C. (2017). Impact of ventricular-peritoneal shunt valve design on clinical outcome of pediatric patients with hydrocephalus: Lessons learned from randomized controlled trials. Surg Neurol Int *8*, 49.

Huang, H., Kuzirian, M.S., Cai, X., Snyder, L.M., Cohen, J., Kaplan, D.H., and Ross, S.E. (2016). Generation of a NK1R-CreER knockin mouse strain to study cells involved in Neurokinin 1 Receptor signaling. Genesis *54*, 593-601.

Huang, T., Lin, S.H., Malewicz, N.M., Zhang, Y., Zhang, Y., Goulding, M., LaMotte, R.H., and Ma, Q. (2018). Identifying the pathways required for coping behaviours associated with sustained pain. Nature.

Hylden, J.L., Anton, F., and Nahin, R.L. (1989). Spinal lamina I projection neurons in the rat: collateral innervation of parabrachial area and thalamus. Neuroscience *28*, 27-37.

Jacob, K., Albrecht, S., Sollier, C., Faury, D., Sader, E., Montpetit, A., Serre, D., Hauser, P., Garami, M., Bognar, L., *et al.* (2009). Duplication of 7q34 is specific to juvenile pilocytic astrocytomas and a hallmark of cerebellar and optic pathway tumours. Br J Cancer *101*, 722-733.

Jansen, N.A., and Giesler, G.J., Jr. (2015). Response characteristics of pruriceptive and nociceptive trigeminoparabrachial tract neurons in the rat. J Neurophysiol *113*, 58-70.

Jarvie, B.C., and Palmiter, R.D. (2017). HSD2 neurons in the hindbrain drive sodium appetite. Nat Neurosci *20*, 167-169.

Jasmin, L., Burkey, A.R., Card, J.P., and Basbaum, A.I. (1997). Transneuronal labeling of a nociceptive pathway, the spino-(trigemino-)parabrachio-amygdaloid, in the rat. The Journal of neuroscience : the official journal of the Society for Neuroscience *17*, 3751-3765.

Jhamandas, J.H., Aippersbach, S.E., and Harris, K.H. (1991). Cardiovascular influences on rat parabrachial nucleus: an electrophysiological study. Am J Physiol *260*, R225-231.

Jongsma, H., Pettersson, L.M., Zhang, Y., Reimer, M.K., Kanje, M., Waldenstrom, A., Sundler, F., and Danielsen, N. (2001). Markedly reduced chronic nociceptive response in mice lacking the PAC1 receptor. Neuroreport *12*, 2215-2219.

Kaestner, S., Poetschke, M., Roth, C., and Deinsberger, W. (2017). Different origins of hydrocephalus lead to different shunt revision rates. Neurol Neurochir Pol *51*, 72-76.

Kainu, T., Honkaniemi, J., Gustafsson, J.A., Rechardt, L., and Pelto-Huikko, M. (1993). Co-localization of peptide-like immunoreactivities with glucocorticoid receptor- and Fos-like immunoreactivities in the rat parabrachial nucleus. Brain Res *615*, 245-251.

Kamate, M., Dumale, A., and Hattiholi, V. (2009). Parenchymal brain cysts in Schimmelpenning-Feuerstein-Mims syndrome. Neurol India *57*, 225-226.

Kaur, S., Pedersen, N.P., Yokota, S., Hur, E.E., Fuller, P.M., Lazarus, M., Chamberlin, N.L., and Saper, C.B. (2013). Glutamatergic signaling from the parabrachial nucleus plays a critical role in hypercapnic arousal. The Journal of neuroscience : the official journal of the Society for Neuroscience *33*, 7627-7640.

Kaur, S., and Saper, C.B. (2019). Neural Circuitry Underlying Waking Up to Hypercapnia. Front Neurosci *13*, 401.

Kaur, S., Wang, J.L., Ferrari, L., Thankachan, S., Kroeger, D., Venner, A., Lazarus, M., Wellman, A., Arrigoni, E., Fuller, P.M., *et al.* (2017). A Genetically Defined Circuit for Arousal from Sleep during Hypercapnia. Neuron *96*, 1153-1167 e1155.

Kestle, J.R., Walker, M.L., and Strata, I. (2005). A multicenter prospective cohort study of the Strata valve for the management of hydrocephalus in pediatric patients. J Neurosurg *102*, 141-145.

Khan, F., Rehman, A., Shamim, M.S., and Bari, M.E. (2015). Factors affecting ventriculoperitoneal shunt survival in adult patients. Surg Neurol Int *6*, 25.

Khasabov, S.G., and Simone, D.A. (2013). Loss of neurons in rostral ventromedial medulla that express neurokinin-1 receptors decreases the development of hyperalgesia. Neuroscience *250*, 151-165.

Khasabov, S.G., Wang, J.C., Simone, D.A., and Strichartz, G.R. (2017). A role for neurokinin-1 receptor neurons in the rostral ventromedial medulla in the development of chronic postthoracotomy pain. Pain *158*, 1332-1341.

Kim, J., Zhang, X., Muralidhar, S., LeBlanc, S.A., and Tonegawa, S. (2017). Basolateral to Central Amygdala Neural Circuits for Appetitive Behaviors. Neuron *93*, 1464-1479 e1465.

Kleczkowska, P., and Lipkowski, A.W. (2013). Neurotensin and neurotensin receptors: characteristic, structure-activity relationship and pain modulation--a review. European journal of pharmacology *716*, 54-60.

Kobashi, M., and Bradley, R.M. (1998). Effects of GABA on neurons of the gustatory and visceral zones of the parabrachial nucleus in rats. Brain Res *799*, 323-328.

Koeller, K.K., and Rushing, E.J. (2004). From the archives of the AFIP: pilocytic astrocytoma: radiologic-pathologic correlation. Radiographics *24*, 1693-1708.

Korinek, A.M., Fulla-Oller, L., Boch, A.L., Golmard, J.L., Hadiji, B., and Puybasset, L. (2011). Morbidity of ventricular cerebrospinal fluid shunt surgery in adults: an 8-year study. Neurosurgery *68*, 985-994; discussion 994-985.

Krashes, M.J., Shah, B.P., Madara, J.C., Olson, D.P., Strochlic, D.E., Garfield, A.S., Vong, L., Pei, H., Watabe-Uchida, M., Uchida, N., *et al.* (2014). An excitatory paraventricular nucleus to AgRP neuron circuit that drives hunger. Nature *507*, 238-242.

Kunwar, P.S., Zelikowsky, M., Remedios, R., Cai, H., Yilmaz, M., Meister, M., and Anderson, D.J. (2015). Ventromedial hypothalamic neurons control a defensive emotion state. Elife *4*.

Kuroda, Y., Ohashi, I., Enomoto, Y., Naruto, T., Baba, N., Tanaka, Y., Aida, N., Okamoto, N., Niihori, T., Aoki, Y., *et al.* (2015). A postzygotic NRAS mutation in a patient with Schimmelpenning syndrome. Am J Med Genet A *167A*, 2223-2225.

Lam, S.K., Srinivasan, V.M., Luerssen, T.G., and Pan, I.W. (2014). Cerebrospinal fluid shunt placement in the pediatric population: a model of hospitalization cost. Neurosurg Focus *37*, E5.

Le Bars, D. (2002). The whole body receptive field of dorsal horn multireceptive neurones. Brain Res Brain Res Rev *40*, 29-44.

Le Bars, D., Gozariu, M., and Cadden, S.W. (2001). Animal models of nociception. Pharmacol Rev *53*, 597-652.

Lebow, M.A., and Chen, A. (2016). Overshadowed by the amygdala: the bed nucleus of the stria terminalis emerges as key to psychiatric disorders. Mol Psychiatry *21*, 450-463.

Lee, H.J., Macbeth, A.H., Pagani, J.H., and Young, W.S., 3rd (2009). Oxytocin: the great facilitator of life. Prog Neurobiol *88*, 127-151.

Leinninger, G.M., Opland, D.M., Jo, Y.H., Faouzi, M., Christensen, L., Cappellucci, L.A., Rhodes, C.J., Gnegy, M.E., Becker, J.B., Pothos, E.N., *et al.* (2011). Leptin action via neurotensin neurons controls orexin, the mesolimbic dopamine system and energy balance. Cell Metab *14*, 313-323.

Levin, S., Robinson, R.O., Aicardi, J., and Hoare, R.D. (1984). Computed tomography appearances in the linear sebaceous naevus syndrome. Neuroradiology *26*, 469-472.

Li, H., Penzo, M.A., Taniguchi, H., Kopec, C.D., Huang, Z.J., and Li, B. (2013). Experience-dependent modification of a central amygdala fear circuit. Nat Neurosci *16*, 332-339.

Li, Y., and van den Pol, A.N. (2006). Differential target-dependent actions of coexpressed inhibitory dynorphin and excitatory hypocretin/orexin neuropeptides. J Neurosci *26*, 13037-13047.

Liang, S.H., Yin, J.B., Sun, Y., Bai, Y., Zhou, K.X., Zhao, W.J., Wang, W., Dong, Y.L., and Li, Y.Q. (2016a). Collateral projections from the lateral parabrachial nucleus to the paraventricular thalamic nucleus and the central amygdaloid nucleus in the rat. Neurosci Lett *629*, 245-250.

Liang, W., Li, L., Cui, X., Tang, Z., Wei, X., Pan, H., and Li, B. (2016b). Enhanced proliferation and differentiation effects of a CGRP- and Sr-enriched calcium phosphate cement on bone mesenchymal stem cells. J Appl Biomater Funct Mater *14*, e431-e440.

Lifshutz, J.I., and Johnson, W.D. (2001). History of hydrocephalus and its treatments. Neurosurg Focus *11*, E1.

Lin, H., and Yan, J. (2010). Linear nevus sebaceous syndrome in a patient with atypical associated abnormalities. J Pediatr Ophthalmol Strabismus *47 Online*, e1-4.

Listernick, R., Ferner, R.E., Liu, G.T., and Gutmann, D.H. (2007). Optic pathway gliomas in neurofibromatosis-1: controversies and recommendations. Ann Neurol *61*, 189-198.

Luo, T., Yu, S., Cai, S., Zhang, Y., Jiao, Y., Yu, T., and Yu, W. (2018). Parabrachial Neurons Promote Behavior and Electroencephalographic Arousal From General Anesthesia. Front Mol Neurosci *11*, 420.

Ma, W., and Peschanski, M. (1988). Spinal and trigeminal projections to the parabrachial nucleus in the rat: electron-microscopic evidence of a spino-ponto-amygdalian somatosensory pathway. Somatosens Res *5*, 247-257.

Mabuchi, T., Shintani, N., Matsumura, S., Okuda-Ashitaka, E., Hashimoto, H., Muratani, T., Minami, T., Baba, A., and Ito, S. (2004). Pituitary adenylate cyclase-activating polypeptide is required for the development of spinal sensitization and induction of neuropathic pain. J Neurosci *24*, 7283-7291.

Maeda, N., Onimura, M., Ohmoto, M., Inui, T., Yamamoto, T., Matsumoto, I., and Abe, K. (2009). Spatial differences in molecular characteristics of the pontine parabrachial nucleus. Brain Res *1296*, 24-34.

Malick, A., Jakubowski, M., Elmquist, J.K., Saper, C.B., and Burstein, R. (2001). A neurohistochemical blueprint for pain-induced loss of appetite. Proceedings of the National Academy of Sciences of the United States of America *98*, 9930-9935.

Mall, V., Heinen, F., Uhl, M., Wellens, E., and Korinthenberg, R. (2000). CNS lipoma in patients with epidermal nevus syndrome. Neuropediatrics *31*, 175-179.

McGaraughty, S., Farr, D.A., and Heinricher, M.M. (2004). Lesions of the periaqueductal gray disrupt input to the rostral ventromedial medulla following microinjections of morphine into the medial or basolateral nuclei of the amygdala. Brain Res *1009*, 223-227.

McGirt, M.J., Woodworth, G., Coon, A.L., Thomas, G., Williams, M.A., and Rigamonti, D. (2005). Diagnosis, treatment, and analysis of long-term outcomes in idiopathic normal-pressure hydrocephalus. Neurosurgery *57*, 699-705; discussion 699-705.

McMahon, S.B., and Wall, P.D. (1985). The distribution and central termination of single cutaneous and muscle unmyelinated fibres in rat spinal cord. Brain Res *359*, 39-48.

Menani, J.V., De Luca, L.A., Jr., and Johnson, A.K. (2014). Role of the lateral parabrachial nucleus in the control of sodium appetite. Am J Physiol Regul Integr Comp Physiol *306*, R201-210.

Menendez, L., Bester, H., Besson, J.M., and Bernard, J.F. (1996). Parabrachial area: electrophysiological evidence for an involvement in cold nociception. J Neurophysiol *75*, 2099-2116.

Merkler, A.E., Ch'ang, J., Parker, W.E., Murthy, S.B., and Kamel, H. (2017). The Rate of Complications after Ventriculoperitoneal Shunt Surgery. World Neurosurg *98*, 654-658.

Meyerson, L.B. (1967). Nevus unius lateralis, brain tumor, and diencephalic syndrome. Archives of dermatology *95*, 501-504.

Miller, R.L., Knuepfer, M.M., Wang, M.H., Denny, G.O., Gray, P.A., and Loewy, A.D. (2012). Fos-activation of FoxP2 and Lmx1b neurons in the parabrachial nucleus evoked by hypotension and hypertension in conscious rats. Neuroscience *218*, 110-125.

Missig, G., Mei, L., Vizzard, M.A., Braas, K.M., Waschek, J.A., Ressler, K.J., Hammack, S.E., and May, V. (2017). Parabrachial Pituitary Adenylate Cyclase-Activating Polypeptide Activation of Amygdala Endosomal Extracellular Signal-Regulated Kinase Signaling Regulates the Emotional Component of Pain. Biol Psychiatry *81*, 671-682.

Missig, G., Roman, C.W., Vizzard, M.A., Braas, K.M., Hammack, S.E., and May, V. (2014). Parabrachial nucleus (PBn) pituitary adenylate cyclase activating polypeptide (PACAP) signaling in the amygdala: implication for the sensory and behavioral effects of pain. Neuropharmacology *86*, 38-48.

Moga, M.M., Herbert, H., Hurley, K.M., Yasui, Y., Gray, T.S., and Saper, C.B. (1990). Organization of cortical, basal forebrain, and hypothalamic afferents to the parabrachial nucleus in the rat. J Comp Neurol *295*, 624-661.

Mollica, F., Pavone, L., and Nuciforo, G. (1974). Linear sebaceous nevus syndrome in a newborn. Am J Dis Child *128*, 868-871.

Moody, M.N., Landau, J.M., and Goldberg, L.H. (2012). Nevus sebaceous revisited. Pediatr Dermatol *29*, 15-23.

Moog, U., Jones, M.C., Viskochil, D.H., Verloes, A., Van Allen, M.I., and Dobyns, W.B. (2007). Brain anomalies in encephalocraniocutaneous lipomatosis. Am J Med Genet A *143A*, 2963-2972.

Moskowitz, R., and Honig, P.J. (1982). Nevus sebaceus in association with an intracranial mass. J Am Acad Dermatol *6*, 1078-1080.

Mpakopoulou, M., Brotis, A.G., Gatos, H., Paterakis, K., and Fountas, K.N. (2012). Ten years of clinical experience in the use of fixed-pressure versus programmable valves: a retrospective study of 159 patients. Acta Neurochir Suppl *113*, 25-28.

Mu, D., Deng, J., Liu, K.F., Wu, Z.Y., Shi, Y.F., Guo, W.M., Mao, Q.Q., Liu, X.J., Li, H., and Sun, Y.G. (2017). A central neural circuit for itch sensation. Science *357*, 695-699.

Muindi, F., Kenny, J.D., Taylor, N.E., Solt, K., Wilson, M.A., Brown, E.N., and Van Dort, C.J. (2016). Electrical stimulation of the parabrachial nucleus induces reanimation from isoflurane general anesthesia. Behav Brain Res *306*, 20-25.

Mulder, H., Uddman, R., Moller, K., Zhang, Y.Z., Ekblad, E., Alumets, J., and Sundler, F. (1994). Pituitary adenylate cyclase activating polypeptide expression in sensory neurons. Neuroscience *63*, 307-312.

Nagase, H., Hayakawa, J., Kawamura, K., Kawai, K., Takezawa, Y., Matsuura, H., Tajima, C., and Endo, T. (1998). Discovery of a structurally novel opioid kappa-agonist derived from 4,5-epoxymorphinan. Chem Pharm Bull (Tokyo) *46*, 366-369.

Nakamura, K., and Morrison, S.F. (2008). A thermosensory pathway that controls body temperature. Nat Neurosci *11*, 62-71.

Nakamura, K., and Morrison, S.F. (2010). A thermosensory pathway mediating heat-defense responses. Proceedings of the National Academy of Sciences of the United States of America *107*, 8848-8853.

Neugebauer, V. (2015). Amygdala pain mechanisms. Handb Exp Pharmacol *227*, 261-284.

Nicholson, B., and Verma, S. (2004). Comorbidities in chronic neuropathic pain. Pain Med *5 Suppl 1*, S9-S27.

Norgren, R. (1978). Projections from the nucleus of the solitary tract in the rat. Neuroscience *3*, 207-218.

Okumura, A., Lee, T., Ikeno, M., Shimojima, K., Kajino, K., Inoue, Y., Yoshikawa, N., Suganuma, H., Suzuki, M., Hisata, K., *et al.* (2012). A severe form of epidermal nevus syndrome associated with brainstem and cerebellar malformations and neonatal medulloblastoma. Brain Dev *34*, 881-885.

Ossipov, M.H., Dussor, G.O., and Porreca, F. (2010). Central modulation of pain. J Clin Invest *120*, 3779-3787.

Palmiter, R.D. (2018). The Parabrachial Nucleus: CGRP Neurons Function as a General Alarm. Trends Neurosci *41*, 280-293.

Panneton, W.M., and Burton, H. (1985). Projections from the paratrigeminal nucleus and the medullary and spinal dorsal horns to the peribrachial area in the cat. Neuroscience *15*, 779-797.

Park, J.M., Kim, D.S., Kim, J., Lee, M.G., and Oh, S.H. (2009). Epibulbar complex choristoma and hemimegalencephaly in linear sebaceous naevus syndrome. Clin Exp Dermatol *34*, e686-689.

Patwardhan, R.V., and Nanda, A. (2005). Implanted ventricular shunts in the United States: the billion-dollar-a-year cost of hydrocephalus treatment. Neurosurgery *56*, 139-144; discussion 144-135.

Pe'er, J., and Ilsar, M. (1995). Epibulbar complex choristoma associated with nevus sebaceus. Arch Ophthalmol *113*, 1301-1304.

Pinto, M., Lima, D., Castro-Lopes, J., and Tavares, I. (2003). Noxious-evoked c-fos expression in brainstem neurons immunoreactive for GABAB, mu-opioid and NK-1 receptors. Eur J Neurosci *17*, 1393-1402.

Polgar, E., Wright, L.L., and Todd, A.J. (2010). A quantitative study of brainstem projections from lamina I neurons in the cervical and lumbar enlargement of the rat. Brain Res *1308*, 58-67.

Pollack, I.F., Albright, A.L., and Adelson, P.D. (1999). A randomized, controlled study of a programmable shunt valve versus a conventional valve for patients with hydrocephalus. Hakim-Medos Investigator Group. Neurosurgery *45*, 1399-1408; discussion 1408-1311.

Qiu, M.H., Chen, M.C., Fuller, P.M., and Lu, J. (2016). Stimulation of the Pontine Parabrachial Nucleus Promotes Wakefulness via Extra-thalamic Forebrain Circuit Nodes. Curr Biol *26*, 2301-2312.

Reddy, G.K., Bollam, P., and Caldito, G. (2012). Ventriculoperitoneal shunt surgery and the risk of shunt infection in patients with hydrocephalus: long-term single institution experience. World Neurosurg *78*, 155-163.

Reddy, G.K., Bollam, P., and Caldito, G. (2014). Long-term outcomes of ventriculoperitoneal shunt surgery in patients with hydrocephalus. World Neurosurg *81*, 404-410.

Reddy, G.K., Bollam, P., Shi, R., Guthikonda, B., and Nanda, A. (2011). Management of adult hydrocephalus with ventriculoperitoneal shunts: long-term single-institution experience. Neurosurgery *69*, 774-780; discussion 780-771.

Ringel, F., Schramm, J., and Meyer, B. (2005). Comparison of programmable shunt valves vs standard valves for communicating hydrocephalus of adults: a retrospective analysis of 407 patients. Surg Neurol *63*, 36-41; discussion 41.

Rizzo, R., and Pavone, P. (2015). Nevus Sebaceous and Its Association With Neurologic Involvement. Semin Pediatr Neurol *22*, 302-309.

Rodriguez, E., Sakurai, K., Xu, J., Chen, Y., Toda, K., Zhao, S., Han, B.X., Ryu, D., Yin, H., Liedtke, W., *et al.* (2017). A craniofacial-specific monosynaptic circuit enables heightened affective pain. Nature neuroscience *20*, 1734-1743.

Roeder, Z., Chen, Q., Davis, S., Carlson, J.D., Tupone, D., and Heinricher, M.M. (2016). Parabrachial complex links pain transmission to descending pain modulation. Pain *157*, 2697-2708.

Roman, C.W., Derkach, V.A., and Palmiter, R.D. (2016). Genetically and functionally defined NTS to PBN brain circuits mediating anorexia. Nat Commun *7*, 11905.

Rosenfeld, M.G., Mermod, J.J., Amara, S.G., Swanson, L.W., Sawchenko, P.E., Rivier, J., Vale, W.W., and Evans, R.M. (1983). Production of a novel neuropeptide encoded by the calcitonin gene via tissue-specific RNA processing. Nature *304*, 129-135.

Ryan, P.J., Ross, S.I., Campos, C.A., Derkach, V.A., and Palmiter, R.D. (2017). Oxytocin-receptor-expressing neurons in the parabrachial nucleus regulate fluid intake. Nature neuroscience *20*, 1722-1733.

Sakurai, K., Zhao, S., Takatoh, J., Rodriguez, E., Lu, J., Leavitt, A.D., Fu, M., Han, B.X., and Wang, F. (2016). Capturing and Manipulating Activated Neuronal Ensembles with CANE Delineates a Hypothalamic Social-Fear Circuit. Neuron *92*, 739-753.

Saleh, T.M. (1997). Visceral afferent stimulation-evoked changes in the release of peptides into the parabrachial nucleus in vivo. Brain Res *778*, 56-63.

Saleh, T.M., and Cechetto, D.F. (1993). Peptides in the parabrachial nucleus modulate visceral input to the thalamus. Am J Physiol *264*, R668-675.

Saper, C.B. (2016). The House Alarm. Cell Metab *23*, 754-755.

Saper, C.B., and Loewy, A.D. (1980). Efferent connections of the parabrachial nucleus in the rat. Brain Res *197*, 291-317.

Sarhan, M., Freund-Mercier, M.J., and Veinante, P. (2005). Branching patterns of parabrachial neurons projecting to the central extended amgydala: single axonal reconstructions. J Comp Neurol *491*, 418-442.

Sato, K., Kubota, T., and Kitai, R. (1994). Linear sebaceous nevus syndrome (sebaceous nevus of Jadassohn) associated with abnormal neuronal migration and optic glioma: case report. Neurosurgery *35*, 318-320; discussion 320.

Sato, M., Ito, M., Nagase, M., Sugimura, Y.K., Takahashi, Y., Watabe, A.M., and Kato, F. (2015). The lateral parabrachial nucleus is actively involved in the acquisition of fear memory in mice. Mol Brain *8*, 22.

Schindler, M., Sellers, L.A., Humphrey, P.P., and Emson, P.C. (1997). Immunohistochemical localization of the somatostatin SST2(A) receptor in the rat brain and spinal cord. Neuroscience *76*, 225-240.

Scioli-Salter, E.R., Forman, D.E., Otis, J.D., Gregor, K., Valovski, I., and Rasmusson, A.M. (2015). The shared neuroanatomy and neurobiology of comorbid chronic pain and PTSD: therapeutic implications. The Clinical journal of pain *31*, 363-374.

Seawright, A.A., Sullivan, T.J., Pelekanos, J.T., and Masel, J. (1996). Coexistent orbital and cerebellar venous anomalies in linear sebaceous naevus syndrome. Aust N Z J Ophthalmol *24*, 373-376.

Seifert, F., Jager, T., Ring, J., and Chen, W. (2012). Concurrence of linear epidermal nevus and nevus flammeus in a man with optic pathway glioma: coincidence or phacomatosis? Int J Dermatol *51*, 592-593.

Shapiro, R.E., and Miselis, R.R. (1985). The central neural connections of the area postrema of the rat. J Comp Neurol *234*, 344-364.

Sharma, R., Singal, A., Verma, P., Rohatgi, J., and Sharma, S. (2012). Epidermal nevus syndrome associated with unusual neurological, ocular, and skeletal features. Indian J Dermatol Venereol Leprol *78*, 480-483.

Shaw, J.S., Carroll, J.A., Alcock, P., and Main, B.G. (1989). ICI 204448: a kappa-opioid agonist with limited access to the CNS. British journal of pharmacology *96*, 986-992.

Shields, C.N., Shields, C.L., Lin, C.J., Menacker, S.J., and Shields, J.A. (2014). Calcified scleral choristoma in organoid nevus syndrome simulating retinoblastoma. J Pediatr Ophthalmol Strabismus *51 Online*, e1-3.

Simon, T.D., Riva-Cambrin, J., Srivastava, R., Bratton, S.L., Dean, J.M., Kestle, J.R., and Hydrocephalus Clinical Research, N. (2008). Hospital care for children with hydrocephalus in the United States: utilization, charges, comorbidities, and deaths. J Neurosurg Pediatr *1*, 131-137.

Stein, S.C., and Guo, W. (2008). Have we made progress in preventing shunt failure? A critical analysis. J Neurosurg Pediatr *1*, 40-47.

Stengel, A., and Tache, Y.F. (2017). Activation of Brain Somatostatin Signaling Suppresses CRF Receptor-Mediated Stress Response. Front Neurosci *11*, 231.

Stone, J.J., Walker, C.T., Jacobson, M., Phillips, V., and Silberstein, H.J. (2013). Revision rate of pediatric ventriculoperitoneal shunts after 15 years. J Neurosurg Pediatr *11*, 15-19.

Tan, C.L., and Knight, Z.A. (2018). Regulation of Body Temperature by the Nervous System. Neuron *98*, 31-48.

Tan, C.O., and Bullock, D. (2008). Neuropeptide co-release with GABA may explain functional non-monotonic uncertainty responses in dopamine neurons. Neurosci Lett *430*, 218-223.

Taniguchi, H., He, M., Wu, P., Kim, S., Paik, R., Sugino, K., Kvitsiani, D., Fu, Y., Lu, J., Lin, Y., *et al.* (2011). A resource of Cre driver lines for genetic targeting of GABAergic neurons in cerebral cortex. Neuron *71*, 995-1013.

Todd, A.J. (2010). Neuronal circuitry for pain processing in the dorsal horn. Nat Rev Neurosci *11*, 823-836.

Todd, A.J., McGill, M.M., and Shehab, S.A. (2000). Neurokinin 1 receptor expression by neurons in laminae I, III and IV of the rat spinal dorsal horn that project to the brainstem. Eur J Neurosci *12*, 689-700.

Tokita, K., and Boughter, J.D., Jr. (2016). Topographic organizations of taste-responsive neurons in the parabrachial nucleus of C57BL/6J mice: An electrophysiological mapping study. Neuroscience *316*, 151-166.

Tokita, K., Inoue, T., and Boughter, J.D., Jr. (2009). Afferent connections of the parabrachial nucleus in C57BL/6J mice. Neuroscience *161*, 475-488.

Tokita, K., Inoue, T., and Boughter, J.D., Jr. (2010). Subnuclear organization of parabrachial efferents to the thalamus, amygdala and lateral hypothalamus in C57BL/6J mice: a quantitative retrograde double labeling study. Neuroscience *171*, 351-365.

Tovote, P., Esposito, M.S., Botta, P., Chaudun, F., Fadok, J.P., Markovic, M., Wolff, S.B., Ramakrishnan, C., Fenno, L., Deisseroth, K., *et al.* (2016). Midbrain circuits for defensive behaviour. Nature *534*, 206-212.

Uddin, O., Studlack, P., Akintola, T., Raver, C., Castro, A., Masri, R., and Keller, A. (2018). Amplified parabrachial nucleus activity in a rat model of trigeminal neuropathic pain. Neurobiol Pain *3*, 22-30.

van de Warrenburg, B.P., van Gulik, S., Renier, W.O., Lammens, M., and Doelman, J.C. (1998). The linear naevus sebaceus syndrome. Clin Neurol Neurosurg *100*, 126-132.

van den Pol, A.N. (2012). Neuropeptide transmission in brain circuits. Neuron *76*, 98-115.

Vanderah, T.W. (2010). Delta and kappa opioid receptors as suitable drug targets for pain. The Clinical journal of pain *26 Suppl 10*, S10-15.

Walker, D.L., and Davis, M. (1997). Double dissociation between the involvement of the bed nucleus of the stria terminalis and the central nucleus of the amygdala in startle increases produced by conditioned versus unconditioned fear. J Neurosci *17*, 9375-9383.

Walker, D.L., Miles, L.A., and Davis, M. (2009). Selective participation of the bed nucleus of the stria terminalis and CRF in sustained anxiety-like versus phasic fear-like responses. Prog Neuropsychopharmacol Biol Psychiatry *33*, 1291-1308.

Wang, L., Chen, I.Z., and Lin, D. (2015). Collateral pathways from the ventromedial hypothalamus mediate defensive behaviors. Neuron *85*, 1344-1358.

Wang, T.X., Xiong, B., Xu, W., Wei, H.H., Qu, W.M., Hong, Z.Y., and Huang, Z.L. (2019). Activation of Parabrachial Nucleus Glutamatergic Neurons Accelerates Reanimation from Sevoflurane Anesthesia in Mice. Anesthesiology *130*, 106-118.

Watanabe, Y., Shido, K., Niihori, T., Niizuma, H., Katata, Y., Iizuka, C., Oba, D., Moriya, K., Saito-Nanjo, Y., Onuma, M., *et al.* (2016). Somatic BRAF c.1799T>A p.V600E Mosaicism syndrome characterized by a linear syringocystadenoma papilliferum, anaplastic astrocytoma, and ocular abnormalities. Am J Med Genet A *170A*, 189-194.

Weisenberg, S.H., TerMaath, S.C., Seaver, C.E., and Killeffer, J.A. (2016). Ventricular catheter development: past, present, and future. J Neurosurg *125*, 1504-1512.

Wu, Y., Green, N.L., Wrensch, M.R., Zhao, S., and Gupta, N. (2007). Ventriculoperitoneal shunt complications in California: 1990 to 2000. Neurosurgery *61*, 557-562; discussion 562-553.

Xu, H., Wang, Z.X., Liu, F., Tan, G.W., Zhu, H.W., and Chen, D.H. (2013). Programmable shunt valves for the treatment of hydrocephalus: a systematic review. Eur J Paediatr Neurol *17*, 454-461.

Yamamoto, T., Shimura, T., Sakai, N., and Ozaki, N. (1994). Representation of hedonics and quality of taste stimuli in the parabrachial nucleus of the rat. Physiol Behav *56*, 1197-1202.

Yamamoto, T., Takemura, M., Inui, T., Torii, K., Maeda, N., Ohmoto, M., Matsumoto, I., and Abe, K. (2009). Functional organization of the rodent parabrachial nucleus. Ann N Y Acad Sci *1170*, 378-382.

Yan, J., Qiu, H., and Li, Y. (2007). Linear nevus sebaceous syndrome associated with choroidal hemangioma. Orbit *26*, 331-335.

Yang, C.F., Chiang, M.C., Gray, D.C., Prabhakaran, M., Alvarado, M., Juntti, S.A., Unger, E.K., Wells, J.A., and Shah, N.M. (2013). Sexually dimorphic neurons in the ventromedial hypothalamus govern mating in both sexes and aggression in males. Cell *153*, 896-909.

Yokota, S., Oka, T., Tsumori, T., Nakamura, S., and Yasui, Y. (2007). Glutamatergic neurons in the Kolliker-Fuse nucleus project to the rostral ventral respiratory group and phrenic nucleus: a combined retrograde tracing and in situ hybridization study in the rat. Neurosci Res *59*, 341-346.

Zagami, C.J., and Stifani, S. (2010). Molecular characterization of the mouse superior lateral parabrachial nucleus through expression of the transcription factor Runx1. PLoS One *5*, e13944.

Zhang, Q., Shi, T.J., Ji, R.R., Zhang, Y.Z., Sundler, F., Hannibal, J., Fahrenkrug, J., and Hokfelt, T. (1995). Expression of pituitary adenylate cyclase-activating polypeptide in dorsal root ganglia following axotomy: time course and coexistence. Brain Res *705*, 149-158.